The Thesis Committee for Suzan Muge Ergene
Certifies that this is the approved version of the following thesis:

Lithologic Heterogeneity of the Eagle Ford Formation, South Texas

APPROVED BY
SUPERVISING COMMITTEE:

Supervisor:

Kitty L. Milliken

William L. Fisher

Charlie Kerans

Lithologic Heterogeneity of the Eagle Ford Formation, South Texas

by

Suzan Muge Ergene, B.S.

Thesis

Presented to the Faculty of the Graduate School of
The University of Texas at Austin
in Partial Fulfillment
of the Requirements
for the Degree of

Masters of Science in Geological Sciences

The University of Texas at Austin
May 2014

Acknowledgements

I would like to thank most importantly, Dr. Kitty Milliken for her continued support and thoughtful guidance. I am forever indebted to her for her patience during both the research and coursework I have experienced at The University of Texas at Austin. My gratitude is also due to my committee members; Dr. William Fisher and Dr. Charlie Kerans provided guidance in committee and in numerous classes that I have taken from both of them.

This study is the part of the project “Characterization of Mudrocks by Quantitative Analysis of High Resolution SEM images” Task 3 of the Shell-UT Unconventional Research Project (SUTUR). Other members of the Task 3 Group are Nick Hayman (co-PI), Maxwell Pommer, Joel Lundsford, Aysen Ozkan (Shell) and Robert Dombrowski (Shell). We thank Patrick Smith for assistance with SEM training. Also, we would like to thank BP for access to the Lozier Canyon outcrop samples.

I would like to offer my special thanks to Turkish Petroleum Corporation for providing scholarship program and sponsoring during my graduate work in The University of Texas at Austin.

Lastly, I would like to thank all my friends and my family for their love, guidance, patience and support they provided during difficult times. This project would never been completed were it not for their support.

Abstract

Lithologic Heterogeneity of the Eagle Ford Formation, South Texas

Suzan Muge Ergene, MS GeoSci
The University of Texas at Austin, 2014

Supervisor: Kitty L. Milliken

Grain assemblages in organic-rich mudrocks of the Eagle Ford Formation of South Texas are assessed to determine the relative contributions of intra- and extrabasinal sediment sources, with the ultimate goal of producing data of relevance to prediction of diagenetic pathways. Integrated light microscopy, BSE imaging, and X-ray mapping reveal a mixed grain assemblage of calcareous allochems, biosiliceous grains (radiolaria), quartz, feldspar, lithics, and clay minerals. Dominant fossils are pelagic and benthic foraminifers and thin-walled and prismatic mollusks; echinoderms, calcispheres, and oysters are present. Early-formed authigenic minerals, including calcite, kaolinite, dolomite, albite, pyrite, quartz, and Ca-phosphate, some reworked, add to the overall lithologic heterogeneity.

Point counting of images produced using energy-dispersive X-ray mapping in the SEM provides observations at a scale appropriate to classifying the mudrocks based on the composition of the grain assemblage, although grains and other crystals of clay-size cannot be fully characterized even with the SEM. Each sample is plotted on a triangle, whose vertices correspond to terrigenous and volcanic grains (extrabasinal components), calcareous allochems, and biosiliceous grains. As a subequal mix of grains of intrabasinal and extrabasinal origins the detrital grain assemblage of the Eagle Ford, presents a formidable challenge to the task of lithologic classification of this unit, as neither conventional limestone nor sandstone classifications can be readily applied. The abundant marine skeletal debris in the Eagle Ford is accompanied by abundant calcite cementation and the dissolution and replacement of biosiliceous debris is accompanied by authigenic quartz, suggesting that mudrock grain classification has potential for yielding diagenetic predictions.

Table of Contents

List of Tables

List of Figures

List of Equations

INTRODUCTION

Purpose of The Study

Heterogeneity of mudrocks, chemical, textural, and lithological, remains inadequately described, although it is clear that variations of mudrocks are more significant than those of limestones and sandstones (Schieber and Zimmerle, 1998; Macquaker et. al., 1998; Macquaker and Howell, 1999; Aplin and Macquaker, 2011; Milliken et. al., 2012(a); Milliken et. al., 2012 (b)) depend on the our definition of heterogeneity in this study. Mixing of intrabasinal and extrabasinal grain assemblages in mudrocks contributes an important heterogeneity that goes well beyond what is observed in other types of sedimentary rocks (Milliken et. al., 2012(b)). It is believed that mudrocks record the changes in primary productivity and bottom water anoxia, which have significant impact on skeletal grain assemblage and sediment aggregates, versus changes in detrital sediment input (Macquaker and Howell, 1999), which has a contribution to the intrabasinal and extrabasinal grain assemblage respectively. In this study the textural and compositional variety of mudrocks rich in intrabasinal-grains is assessed through petrographic studies of the Upper Cretaceous Eagle Ford Formation. The fundamental objectives of the study are to (1) use outcrop and core samples of the Lower and Upper Eagle Ford to identify different grain types and group them as extrabasinal grains versus intrabasinal grains, (2) assess textural and compositional variety, (3) identify diagenetic components and decipher the contrasting diagenetic histories that relate to variations in the detrital grain assemblage, and (4) test a means of mudrock classification to predict diagenetic behavior and response to the changing physical and chemical subsurface conditions.

Petrography and sedimentology of mudrocks have not been studied in sufficient detail, in part because methodologies (notably field-emission scanning electron microscopy) suitable for examination of mudrock grains have only become widely available in the past decade. In this study, a variety of petrographic methods allow us to assess compositional variations at magnifications appropriate to making grain-scale observations. By analogy to sandstones and limestones, the subsurface porosity evolution and mechanical behavior of the mudrocks are most likely controlled by the primary grain assemblage (e.g., (Land et. al., 1997)), but this hypothesis needs further exploration (Milliken et. el., 2012 (b)). Post-depositional processes including compaction, grain dissolution, and cementation need to be evaluated in the context of mudrocks. Porosity loss caused by diagenesis clearly is related to the grain size and lithological properties of mudrocks (Dewhurst, 1998), but the manner in which diagenetic changes affect lithology is poorly known. For instance, dissolution and replacement causes the decrease in detrital K-feldspar amount with depth in mudrocks (Land et. al., 1997; Hower et. al., 1976), which is similar to behavior of detrital feldspar in sandstones (Land et. al., 1997, Milliken, 1992, and Blatt, 1985). The study of Hower (1976) suggesting that burial diagenesis occurs in a closed system was disputed in the study of Land et. al. (1997) in which it was concluded that open chemical processes are responsible for the burial diagenesis of argillaceous sediments. The fate of material released by this grain dissolution remains unknown. The main point which can be interpreted in either way (open versus closed systems), is that primary composition controls burial diagenesis in fine-grained argillaceous sediments in a manner completely analogous to the controls on diagenesis in sandstones.

In this study grain types and lithological properties of the Eagle Ford are assessed for the prediction of porosity loss and mechanical behavior. A sample suite across depth and thermal maturity is used to evaluate how grain assemblages respond to post-depositional processes in the subsurface.

PREVIOUS WORK

Geologic Setting and Paleogeography

In the Gulf Coast region, a single amalgamated carbonate platform, the Comanche Shelf developed during Cretaceous period at the top of Jurassic ramp sediments without pronounced shelf margin (Phelps et. al., 2014) (Figure 1). Alternations of prograding carbonate platforms and transgressive organic-rich mudrocks on the Comanche Shelf developed in two primary episodes (Montgomery et. al., 2002; Phelps et. al., 2014). It was proposed that each episode is characterized by two shelfal depositional profiles which are the regressive, flat-topped reef-rimmed platforms (organism and biotic process driven) and transgressive to high-stand storm-dominated ramp profiles (physical process driven) (Figure 1) (Harbor, 2011).

Deposition of transgressive mudstones including Pearsall (organic-rich), Del Rio (oyster-rich to planolites-rich (Phelps et. al., 2014)), and Eagle Ford (organic-rich) coincides with the back-stepping of the Comanche Platform in South Texas. Among them, the thickest transgressive organic-rich mudrock deposit was Eagle Ford on the Comanche Shelf. The Washita supersequence, which includes carbonates and shales of the Stuart City, Kiamichi, Georgetown, Del Rio and Buda formations (Phelps et. al., 2014), is capped by the Mid-Cretaceous Unconformity (MCU) above the Buda Formation (Figure 1), which is recognized in the regional seismic data of Gulf of Mexico defined by Buffer et al, 1980, Faust, 1990, and Dawson, 1997. The Mid-Cretaceous Unconformity, which is a major disconformity in the Mesozoic rock record, can be explained by uplift coupled with eustatic regression that produced shelf-edge exposure prior to Eagle Ford deposition (Galloway, 2008; Harbor, 2011). Because the Eagle Ford directly overlies Buda Limestone in South Texas (Figure 5), the Mid-Cretaceous unconformity, whose spatial distribution is not known in South Texas, can be considered as the boundary between Buda Limestone and Eagle Ford (Phelps et. al., 2014). Biostratigraphic data, geochemical analysis, and subaerial exposure surface where the former shelf margin was supposed to be observed are considered as evidences for the unconformity (Phelps et. al., 2014).

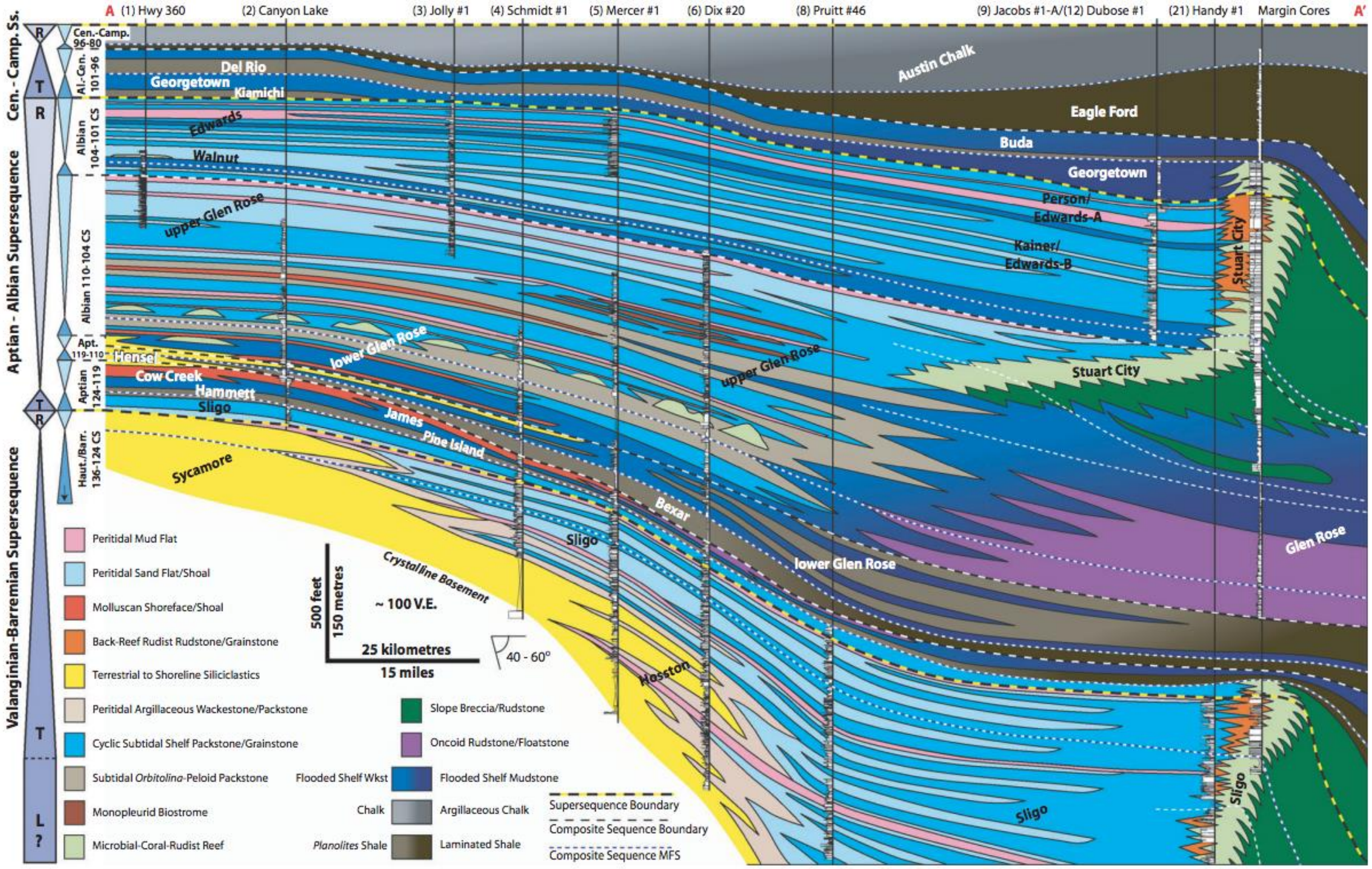

Figure 1: Architecture of Gulf Coast Cretaceous carbonate platforms and organic-rich shales/mudrocks. The Comanche shelf is characterized by the alternations of platform carbonates and organic-rich mudrocks (Phelps et. al., 2014) At the top of the supersequences Eagle Ford-Austin Chalk deposition is observed.

The Eagle Ford Formation of South Texas is a mixed siliciclastic//carbonate unit (Dawson, 1997; Dawson, 2000; Harbor, 2011; Workman and Grammer, 2013). This study addresses petrographic characterization of the Eagle Ford Formation in subsurface core samples and outcrop samples (Figure 2). Regionally, Eagle Ford strata consist of two major depositional units: the lower (transgressive) unit dominated by dark well-laminated calcareous shales and the upper regressive unit consisting of interstratified mudrocks and limestones (Dawson, 1997). Two main facies, corresponding roughly to the units described above, are identified by Fishman et al. (2013) including foraminiferal mudstones with high total organic carbon (TOC) contents (Zhang et. al., 2014) deposited in the lowermost transgressive system track (TST) or near maximum flooding surface (MFS) intervals, and limestones with relatively low TOC contents, interbedded with and deposited in the overlying high stand system interval.

The Eagle Ford was deposited in distally steepened ramp without shelf margin during Cenomanian-Turonian (Phelps et. al., 2014). Volcaniclastic sediments were delivered by winds, directed from west-southwest to east-northeast (Figure 4). Transport and reworking of volcaniclastic sediments into the Maverick and Gulf Coast Basins contributed to the overall nutrient-rich sediment budget (Sinton and Duncan, 1997; Jennings and Antia, 2013; and Phelps et. al., 2014) (Figure 4). Identification of the grain assemblage is essential to understanding the effects of volcanism in the deposition of Eagle Ford.

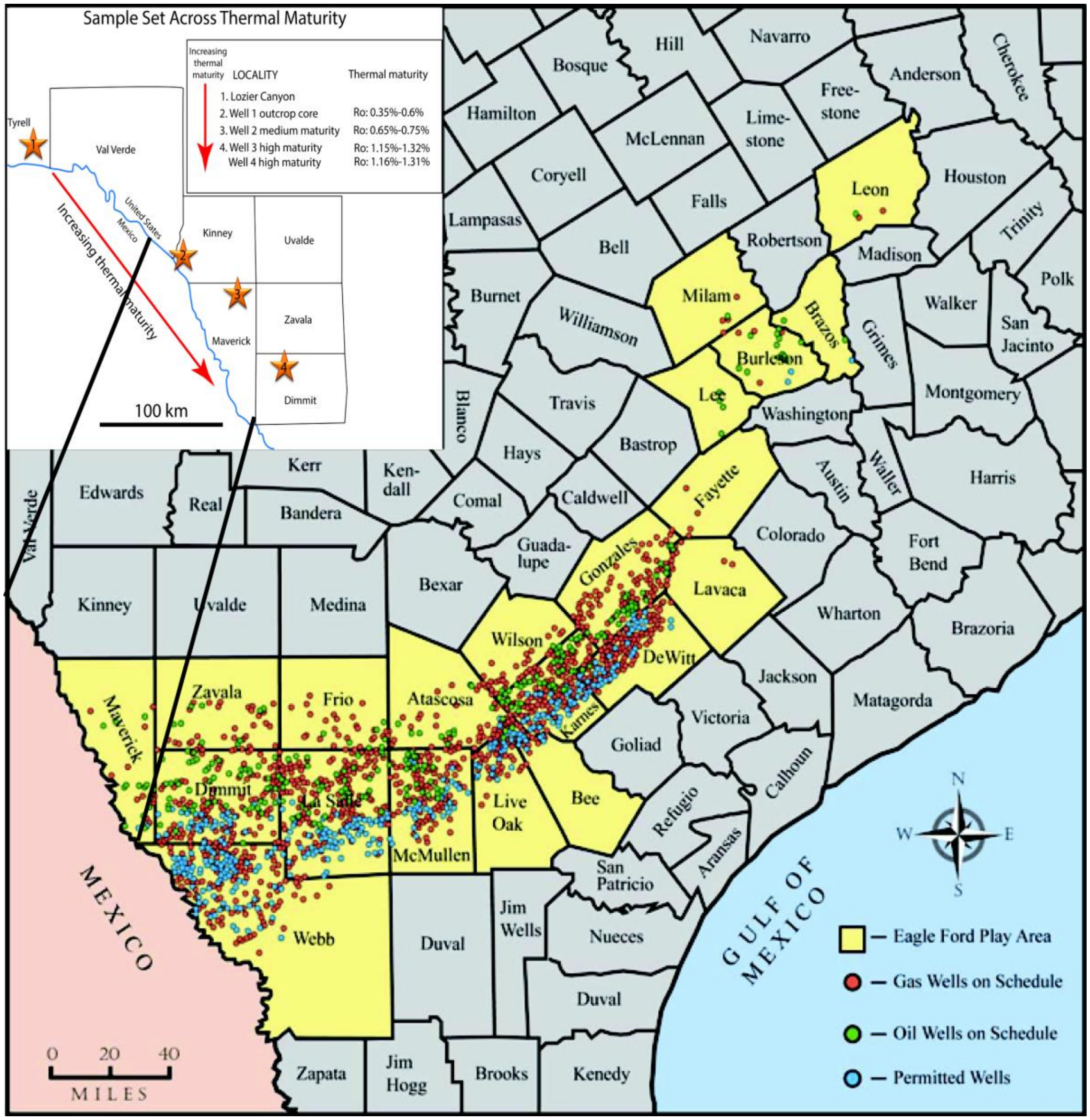

Figure 2: Map of Texas that shows the geographic extent of the current Eagle Ford play area and drilling activity (modified from the Railroad Commission of Texas, 2012). The study area and the sample locations are shown at the upper left corner of the map.

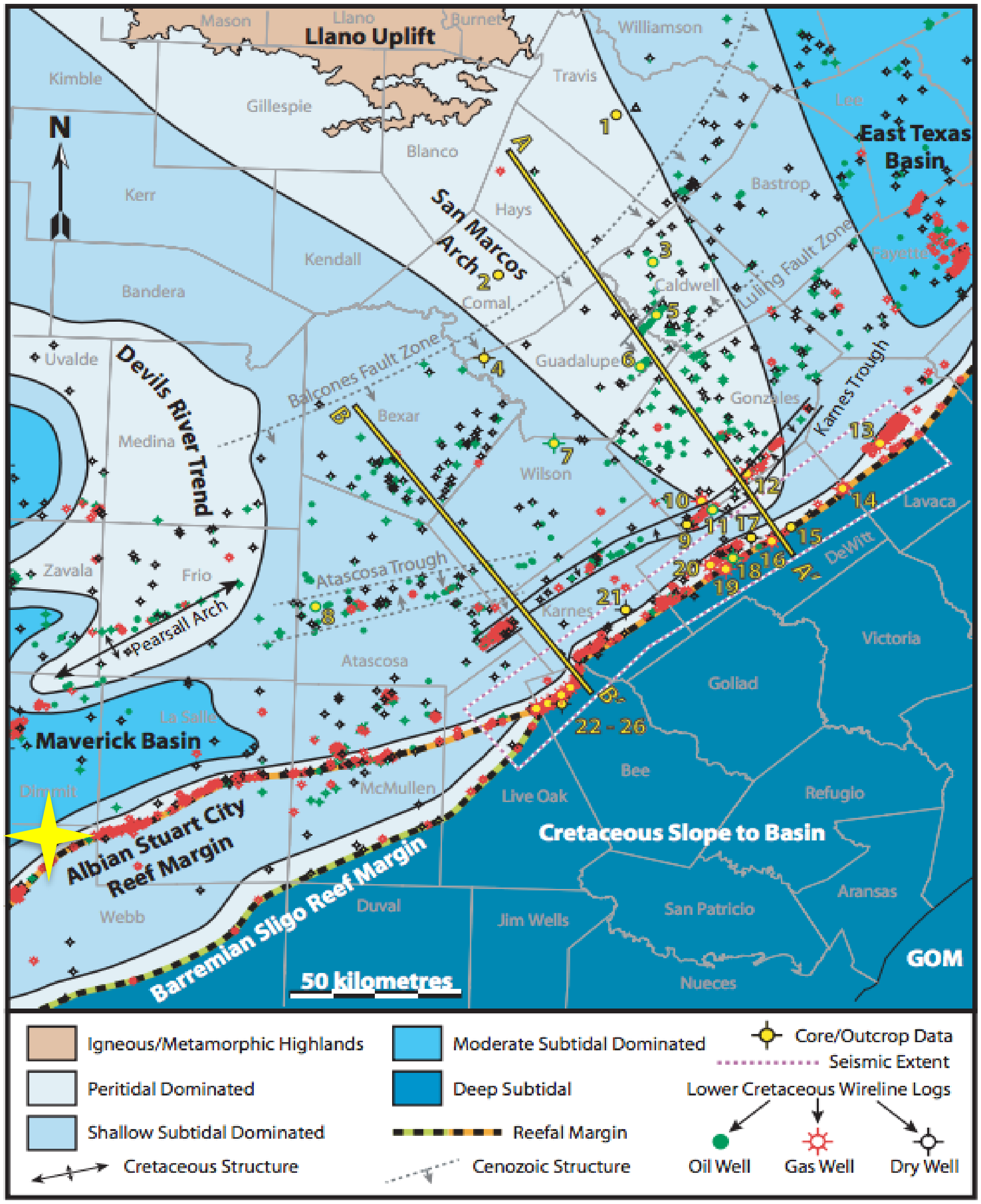

Figure 3: Paleogeographic map of South Texas area with Cretaceous and Cenozoic structural features (Phelps et. al., 2014). Note that extent of Maverick Basin (part of the study area indicated by yellow star) and East Texas Basin and San Marcos Arch are observed.

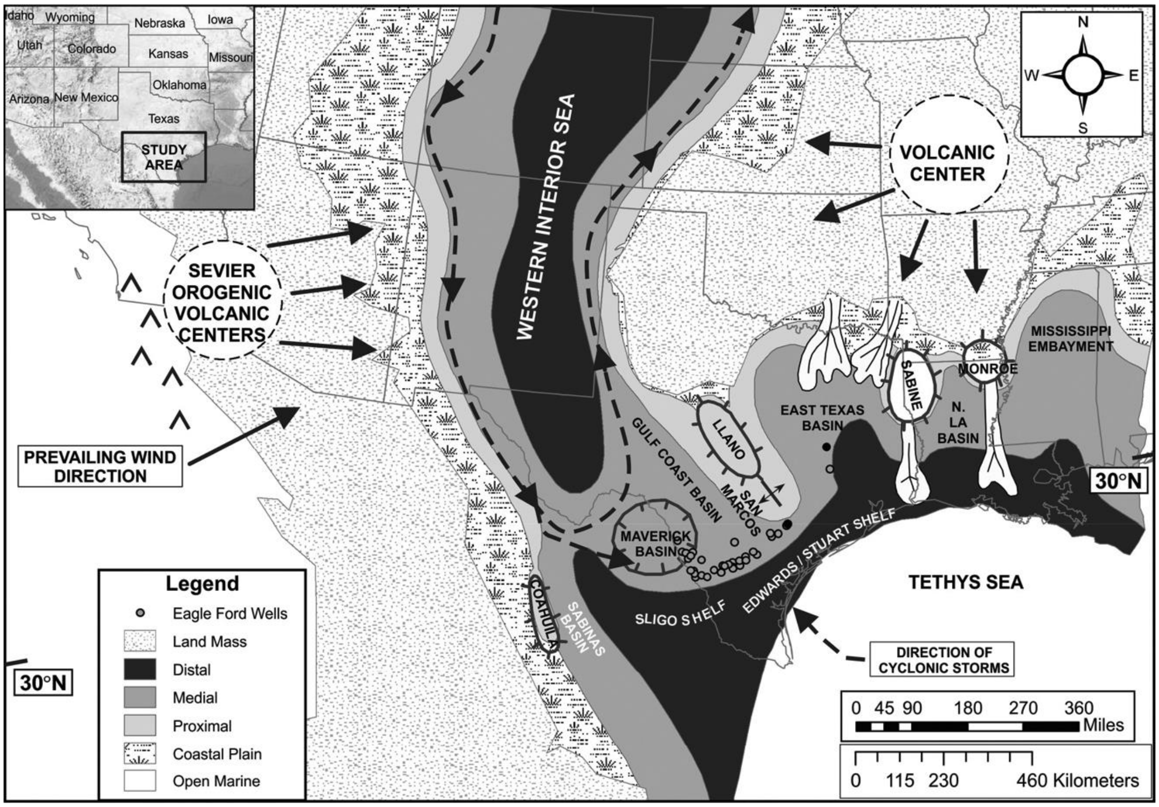

Figure 4: Late Cenomanian paleogeography and volcanism from Jennings and Antia, (2013). Dashed lines with arrows indicate interpreted marine current directions and directions and the direction of Cenomanian-Turonian cyclonic storms. The black arrows radiating from the volcanic center show the direction of transported continental sediments.

Study Location

The type locality of the Eagle Ford is in Dallas County near the village of Eagle Ford was established by R.T. Hill in 1887 (Adkins and Lozo, 1951). The Eagle Ford Group within northern East Texas is divided into three formations including Tarrant, Britton, and Arcadia Park Formations because of lithologic heterogeneity by W.L.

Moreman in the study of Sellards et. al., 1932. An Eagle Ford outcrop stratigraphy and a thickness variation from about 100 ft near Dallas, Texas to around 10 ft in Austin were proposed in his study. According to his observations, the contact with the Austin Chalk is unconformable as supported by the occurrence of clay, gypsum, phosphatic nodules, reworked pelecypods and fish remains at the transition zone. This transition zone at the top of the Eagle Ford was interpreted as a condensed zone in the southern and central Texas in the following year (Sellards et. al., 1932). In the same study (Sellards et. al., 1932), it was stated that borings at the base of the Austin Chalk are filled with glauconitic chalk in Hays and Travis counties. In the following years, the contact between the Eagle Ford and Austin Chalk continued to attract attention due to its variable thickness and thinning of the Eagle Ford towards to south onto the San Marcos Arch was explained as non-deposition at the base and truncation at the top in the study of Brown and Pierce, 1962. Montgomery (1991) also supported the existence of an unconformity on the San Marcos Arch is located. In the outcrop-based biostratigraphic study of Jiang (1989), based on ammonites and planktonic foraminifera, it is shown that Coniacian Austin Chalk is underlain unconformably by the Turonian upper Eagle Ford rocks. The boundary between Eagle Ford and Austin Chalk is interpreted as diachronous at the regional scale in the dissertation of Phelps, 2011 since it becomes younger down the depositional dip. The age of Eagle Ford is defined as Cenomanian to Turonian, and the time span in Eagle Ford-Austin Chalk supersequence is determined as 14 Ma (94-80 Ma) in the study of Jiang (1989).

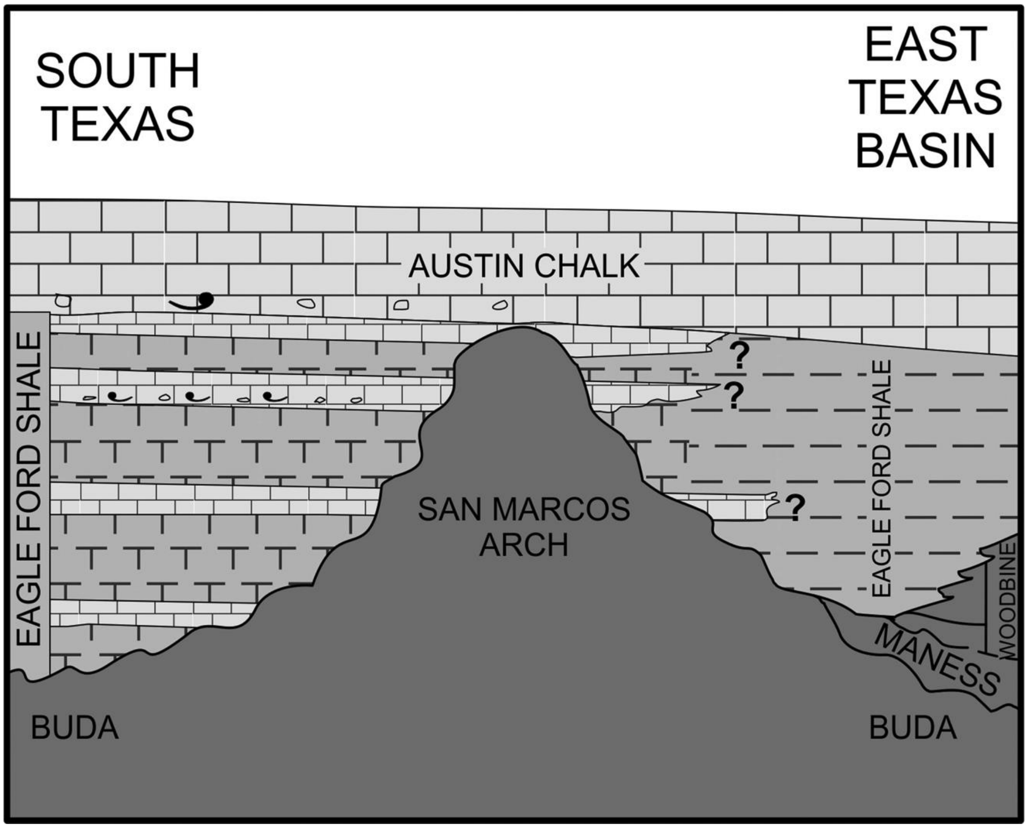

Figure 5: Generalized regional stratigraphic model. The San Marcos arch separates the East Texas Basin from the Gulf Coast Basin and Maverick Basin in South Texas. In South Texas, which is the focus of this study, the Eagle Ford directly overlies the Buda Limestone (Jennings and Antia, 2013).

More recent work on the stratigraphy and depositional environment of the Boquillas Formation, the age-equivalent of the Eagle Ford in the southwest Texas area is reported by Miller (1990) The Boquillas contrasts with the subsurface from Eagle Ford lithologically in terms of having a higher proportion of thin calcareous flagstone beds relative to black, organic-rich shale (Miller, 1990). In the study of Miller (1990), they tried to figure out the abrupt lithologic change between Buda and Boquillas contact and they explained this sharp contact with tectonic subsidence instead of gradual rise in sea level and this causes rapid transgression of lowermost part of the Boquillas Formation onto the Buda platform.

Additional work on the sequence stratigraphy and geochemistry of the condensed section in the Eagle Ford Group, East-Central Texas area is the study of Liro et. al., 1994. According to Hancock (1993) this condensed interval corresponds to one of the greatest and most rapid sea level rises in Earth history, which remains controversial. The Eagle Ford Formation, which was deposited during mid-Cretaceous second-order eustatic transgression (Haq et. al., 1988; Hancock. 1993), is divided into lower and upper members, which are also used in the later study of Grabowski (1984). Lithologic variability in lower and upper portions of the Eagle Ford is defined in terms of sequence stratigraphic principles and geochemistry (Liro et. al., 1994). Analysis based on sequence stratigraphy and organic geochemistry shows the depositional cyclicity at higher frequency (3rd order eustatic cycles). The data obtained from the geochemical variations reveals the control mechanisms of cyclicity, which are defined as clastic and organic sediment sources and possibly climate and water chemistry (Liro et. al., 1994). Stratigraphic variations are explained with the relative sea level changes and while the reason of lateral variations are associated with the proximity to the coast in their study. Different types of intrabasinal grains, texture and grain size affect the interpretation about the depositional setting and depositional conditions of the Eagle Ford. Abundance of marine fossils suggest largely shallow marine paleoenvironment of deposition for the Eagle Ford (Pessagno, 1969; Jiang, 1989) on the other hand, mixture of marine fossils and terrestrial debris inside the siltstone and fine-grained sandstone indicates the lagoonal or deltaic depositional setting.

More recently, outcrop based studies in the North-Central Texas were conducted by Dawson between 1997 and 2000. The Eagle Ford has two different depositional trends including global transgression and following highstand of eustatic sea level in terms of sequence stratigraphic concepts (Liro et. al., 1994 and Dawson, 1997). In the study of Ekdale and Mason (1988) a characteristic trace fossil assemblage in transgressive shales as an indicator of oxygen-depleted conditions is also discussed in the study of Miller (1990), Liro et. al., (1994) and Dawson (1997), This study is supported by the lack of bioturbation, identification of Chondrites burrows (Dawson, 1997; Lock et. al., 2010; Harbor, 2011; McGarity, 2013; Workman and Grammer, 2013), predominance of framboidal pyrite (Wilkin and Barnes, 1997), and organic enrichment in the transgressive shales (Dawson, 1997; Robison, 1997). In Late Cenomanian to early Turonian time interval, these transgressive shales are known with their highly reduced sedimentation rates in global scale (Dawson, 1997).

Source rock potential of Eagle Ford in East Texas Basin (Figure 5) was described in the study of Surles, 1987 and subdivided into different formations according to lithological variations which were firstly described in the study of Sellards et. al., 1932. This discrimination is based on the relative contributions deltaic and fringing marine sands, and dark bituminous laminated clay amount (Surles, 1987). Although Eagle Ford is known as an intrabasinal-grain-rich mudrock today, it is obvious that siliciclastic influx has a pronounced effect on Eagle Ford deposition. Maverick Basin in the South Texas area, which is the mainly the study area, and East Texas Basin are considered as increased subsidence and sedimentation zones (Phelps et. al., 2014) (Figure 3). The source of the sediments are river-dominated deltas which includes dominantly mud deposits and their progradation from north and northwest through marine shelf of east Texas and Woodbine erosion which are considered as productive conditions for organic rich laminated shale sedimentation in Eagle Ford time (Surles, 1987). Another source of siliciclastic sediment supply is accepted as the Sabine uplift that resulted in erosion in the East Texas in the study of Surles (1987). In the study of Cotera (1956), it is indicated that Upper Woodbine has two sources to the east of the East Texas Basin which are the Precambrian and Paleozoic rocks at the southern end of the Appalachian Mountains and Ouachita Mountains or mid-continent region and southwestern Arkansas. San Marcos Arch, which is located between these two basins and composed of granitic and metamorphic rocks derived from LIano Uplift (Figure 3), is less subsided compared to adjacent basins (Phelps et. al., 2014) (Figure 3). East Texas Basin is totally different from the South Texas Basin in terms of detrital assemblage (Jennings and Antia, 2013) and South Texas Basin has more restricted siliciclastic influx due to hindering effect of San Marcos Arch (Ozkan et. al., 2014).

Climatic Events

The events, which cause organic-rich fine-grained sediment deposition where the worldwide oxygen depleted zones occur in the world ocean, firstly recognized by Schlanger and Jenkyns (1976). They came up with the idea that this globally widespread deposition of organic-rich sediments was controlled of major geologic and climatic factors instead of local mechanisms. These events named as 'Oceanic Anoxic Events (OAEs)' occur in pelagic sedimentary sequences of Aptian-Albian and Cenomanian-Turonian age with the latter corresponding to the Eagle Ford (Schlanger and Jenkyns, 1976). Cenomanian-Turonian Anoxic Event, which is prior to the deposition of the Eagle Ford, can be correlated with the maximum high stand sea level (Arthur et. al., 1987). In the later studies, more OAEs were defined in Cretaceous section of South Texas, which include Late Aptian OAE 1a (Pine Island), Aptian-Albian OAE 1b (Upper Bexar//Lower Glen Rose), Albian/Cenomanian OAE 1d (Upper Georgetown/Del Rio), and Cenomanian/Turonian OAE 2 (Eagle Ford) (Phelps et. al., 2014).

The key factor in organic matter enrichment globally in oceans is the major transgressive episodes, which provide the driving mechanism for nutrient enrichment and organic matter production and have an effect on climate and bottom-water currents (Schlanger and Jenkyns, 1976; Arthur and Sageman, 2004). Global drivers for intensified organic matter burial are increased sea-floor spreading rates and surface volcanic activity and that releases large amounts of CO_2 into the atmosphere and increases global temperatures. Oxygen minimum zones form in the world ocean during globally correlative climatic events, (OAEs; Oceanic Anoxic Events) during which these zones expand geographically and vertically (Schlanger and Jenkyns, 1976).

Geochemical analysis, which was mostly supported by carbon isotope composition, has shown that an increase in rate of burial of organic carbon coincides with a major global rise in sea level near Cenomanian-Turonian (C/T) oceanic anoxic event (OAE2) (Arthur et. al., 1988). Alternating oxygenation levels, which can be associated with Oceanic Anoxic Event-2 (OAE-2), cause variety in texture (Macquaker and Gawthorpe, 1993) of Upper and Lower Eagle Ford Formations (Dawson, 1997; Dawson, 2000; Jennings and Antia, 2013; Workman, 2013; Corbett and Watkins, 2013).

Regional factors relevant to understanding the Eagle Ford Formation are conditions of lowered oxygenation caused by the rise in sea level, the expansion of nutrient-rich waters and an increase in the organic carbon production (Miller, 1990). Nutrient-rich waters, which are also recorded at the Cenomanian-Turonian boundary, is considered as associated with volcanism, which is resulted in consumption of seawater O_2 and organic carbon flux to the sea floor (Sinton and Duncan, 1997). These conditions are suitable for the deposition of organic-rich shale (Schlanger and Jenkyns, 1976). According to Lash (1987) climate is another significant parameter affecting the deposition of organic rich shale in the study area. Also, when stratigraphic changes in Eagle Ford are compared with the study of global paleoenvironmental and geochemical changes conducted by Ulicny et. al. (1993), consistency can be easily realized. The correlation between the oxygen depletion steps and eustatic sea level rise shows that major transgression is responsible for the anoxic event in global scale (Ulicny, 1993).

Lozier Canyon outcrops in South Texas were studied by Miller (1990). Geochemical analysis based on C/S (carbon/sulphur) ratios cannot be used to document euxinic conditions for Eagle Ford deposition because subaerial exposure and weathering conditions at the surface have altered the C/S ratio. Overestimated C/S ratios arise from the loss of sulphur, during weathering and the formation of gypsum and iron oxides (Dawson, 2000).

Previous Work on Mudrock Classification

There is no current consensus on the classification of fine-grained sedimentary rocks. Several methods of classification have been developed as a result of ongoing debates (Spears, 1980). For instance, classification methods are proposed on the basis of (1) grain size and composition (quartz content) (Spears, 1980), (2) texture (Flemming, 2000; Folk, 1954; Shepard, 1954: Macquaker and Adams, 2003), (3) from an engineering point of view (Grainger, 1984; Fontoura, 2002), (4) on the source of the organic matter (terrestrial, lacustrine or marine organic shale) (Hutton, 1987), (5) texture (grain size) and laminations (presence or absence) in combination (Lundegard and Samuels, 1980; Folk, 1965), (6) color (variable with the source of detritus) (McBride, 1974) and (7) geochemistry (Herron, 1988). In the study of Schieber and Zimmerle (1998), it is stated that compositional variations were mostly used as a main variable instead of texture and fabric to categorize shales. On the other hand, they proposed that texture and fabric are inevitable for descriptive classification because of their great variety. Here, a three-component system of calcareous-biogenic, siliceous-biogenic and non-biogenic extrabasinal components is used and an approach strongly influenced by the classification developed by Dean et, al., 1985. Flawn (1953) stated that the mineral composition of the rock has been modified by alteration (except for weathering), which results from increased temperature and pressure rather than various types of lithification (deposition), drawing the line between the sedimentary rocks and low-grade metamorphic rocks, which should be considered while making classification of argillaceous sedimentary rocks. Here, diagenetic minerals are excluded because they represent an overprint on primary composition. The approach of excluding authigenic minerals in our mudrock classification derives from the emphasis on grain assemblages in both the carbonate and sandstone classifications of Folk (1980).

A key controversy in the nomenclature for fine-grained sedimentary rocks concerns the distinction between shales and mudstones. The term shale, “a laminated clayey rock” was used in the English mining district of Derbyshire (Tourtelot, 1960). Today, a common definition of shale is a fissile (Tourtelot, 1960; Pettijohn, 1975) (Figure 6) or laminated rock more than a class name for fine-grained rocks, whereas a mudstone is neither fissile nor laminated (after Blatt et. al., 1972; Spears, 1976 and 1980; Lundegard and Samuels, 1981; Shaw, 1997). Spears (1980) considered fissility as a classification property (Figure 6) because it is the surface manifestation of the lamination while in the reply of Lundegard and Samuels (1981), it is stated that due to the importance of knowing depositional conditions, classification should be based on primary sedimentation features.

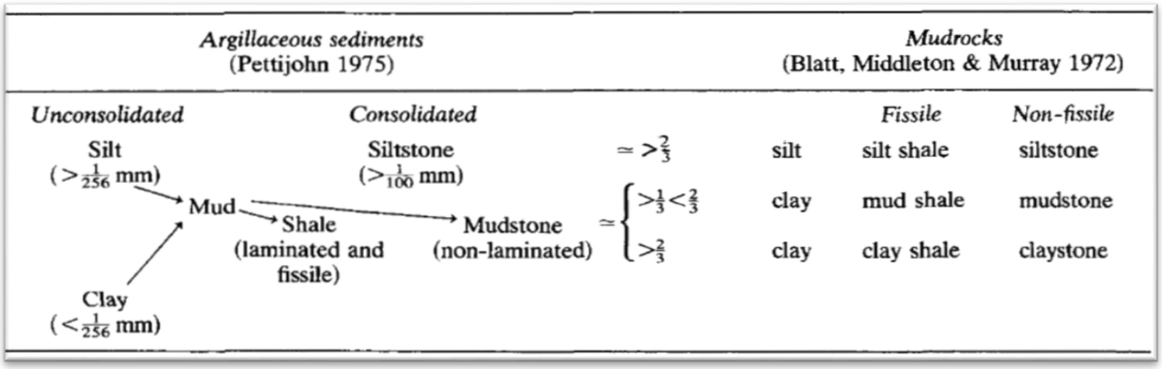

	Mudrocks (Blatt, Middleton & Murray 1972)	*Fissile*	*Non-fissile*
$\simeq >\frac{2}{3}$	silt	silt shale	siltstone
$\simeq >\frac{1}{3} < \frac{2}{3}$	clay	mud shale	mudstone
$>\frac{2}{3}$	clay	clay shale	claystone

Figure 6: Classification of fine-grained sedimentary rocks (Spears, 1980)

A simple compositional classification for the fine-grained sedimentary rocks is tested in this study. Calcareous allochems, biosiliceous grains and terrigeneous and volcanic grains are defined as the end-members of the three-component system, which is developed by Milliken (unpublished). The utility of this simple nomenclature of the fine-grained sedimentary rocks is tested with the examination of the effects of grain assemblage on diagenesis. Classification is carried out by point counting of X-ray maps on which grain boundaries and grain types can be observed and grains, including those of near-clay size, can be discriminated from crystals of authigenic minerals.

METHODS

In this study, mostly qualitative petrographic methods are used. Light microscopy can be used to delineate the majority of lithologic, textural, and faunal assemblage variations, however it is inadequate for characterization of the dominant particle fraction that is smaller than 30 µm (thickness of a standard thin section). Field-emission scanning electron microscopy (FE-SEM) is used because its higher magnifications allow inspection of the silt- and clay-size fractions.

Developments in the SEM studies of sandstones and limestones provided new opportunities to differentiate authigenic and detrital phases because interpretation of clay assemblages became possible (Wilson and Pittman, 1977). Wilson (1971) applied those SEM techniques to discriminate authigenic from detrital kaolinite using the Devonian sedimentary rocks in Scotland. Today, SEM techniques and other new techniques are used not only for identification of authigenic and detrital clay minerals (O'Brien and Slatt, 1990) but also, to examine a variety of other diagenetic changes (Macquaker and Gawthorpe, 1993) although there are still some challenges to interpret all diagenetic features because some important rock components remain too small to image (Schieber and Zimmerle, 1998).

Observations

Petrographic analyses of the Eagle Ford Formation reported here are conducted by mainly qualitative methods. Lozier Canyon outcrop samples, low-maturity outcrop core samples, medium-, and high-maturity core samples are used to make detailed lithologic and textural assessments. Samples at different maturity levels and from different parts of the basin are analyzed on the basis of thin section observations (Table 1 & Figure 7). Analyses are performed by using light microscopy, and scanning electron microscopy (FE-SEM) including both backscattered electron (BSE) and secondary electron imaging techniques and X-ray mapping techniques. Cathodoluminesence (CL) imaging, based on both light microscopy and FE-SEM, is another method to differentiate grain types from authigenic phases.

Table 1: Sample set from the different maturity levels and depths used for imaging.

Sample No	Sample No	Depth(m)	Sample No	Depth (m)	Sample No	Depth (m)	Sample No**	Depth (m)**
LZ-1	23*	56.63-56.6	CH1	911.28	EF3 1-31	2524.77	EF3-1	2519.02
LZ-2	22*	57.11-57.08	CH2	915.79	EF3 1-61	2533.88	EF3-2	2524.81
LZ-3	21*	69.88-69.85	CH3	950.24	EF3 1-66	2535.49	EF3-3	2529.32
LZ-4	20*	79.68-79.65	CH4	953.22	EF3 1-136	2556.66	EF3-4	2533.89
LZ-5	19	81.28-81.25	CH5	963.78	EF4 1-5	2775.04	EF3-5	2535.37
LZ-6	18*	88.93-88.8	CH6*	969.95	EF4 1-10	2776.62	EF3-6	2547.43
LZ-7	17	92.84-92.81	CH7*	973.26	EF4 1-25	2781.10	EF3-7	2547.90
LZ-8	16*	98.11-98.08			EF4 1-35*	2784.09	EF3-8	2549.06
	15	99.85-99.82			EF4	2787.70	EF3-9	2553.68
	14	104.86-104.83			EF4	2790.75	EF3-10	2556.69
	13*	106.47-106.44			EF4 1-75	2796.24	EF4-1	2775.07
	12	110.04-110.01			EF4 1-80	2797.93	EF4-2	2776.53
	11*	115.48-115.45			EF4 1-90	2800.90	EF4-3	2778.15
	10	122.94-122.91			EF4 1-100	2803.99	EF4-4	2780.43
	8	128.91-128.88			EF4 1-123	2811.06	EF4-5	2781.10
	7*	133.71-133.68			B 1 HB	2966.01	EF4-6	2785.73
	4	139.88-139.85					EF4-7	2792.71
	2*	149.52-149.49					EF4-8	2796.28
	1	151.88-151.85					EF4-9	2797.77
							EF4-10	2802.35
							EF4-11	2803.87
							EF4-12	2809.49
							EF4-13	2811.00

** represents samples which are imaged by only using light microscopy.

* represents samples which are imaged by also using cathodoluminescence (CL) method.

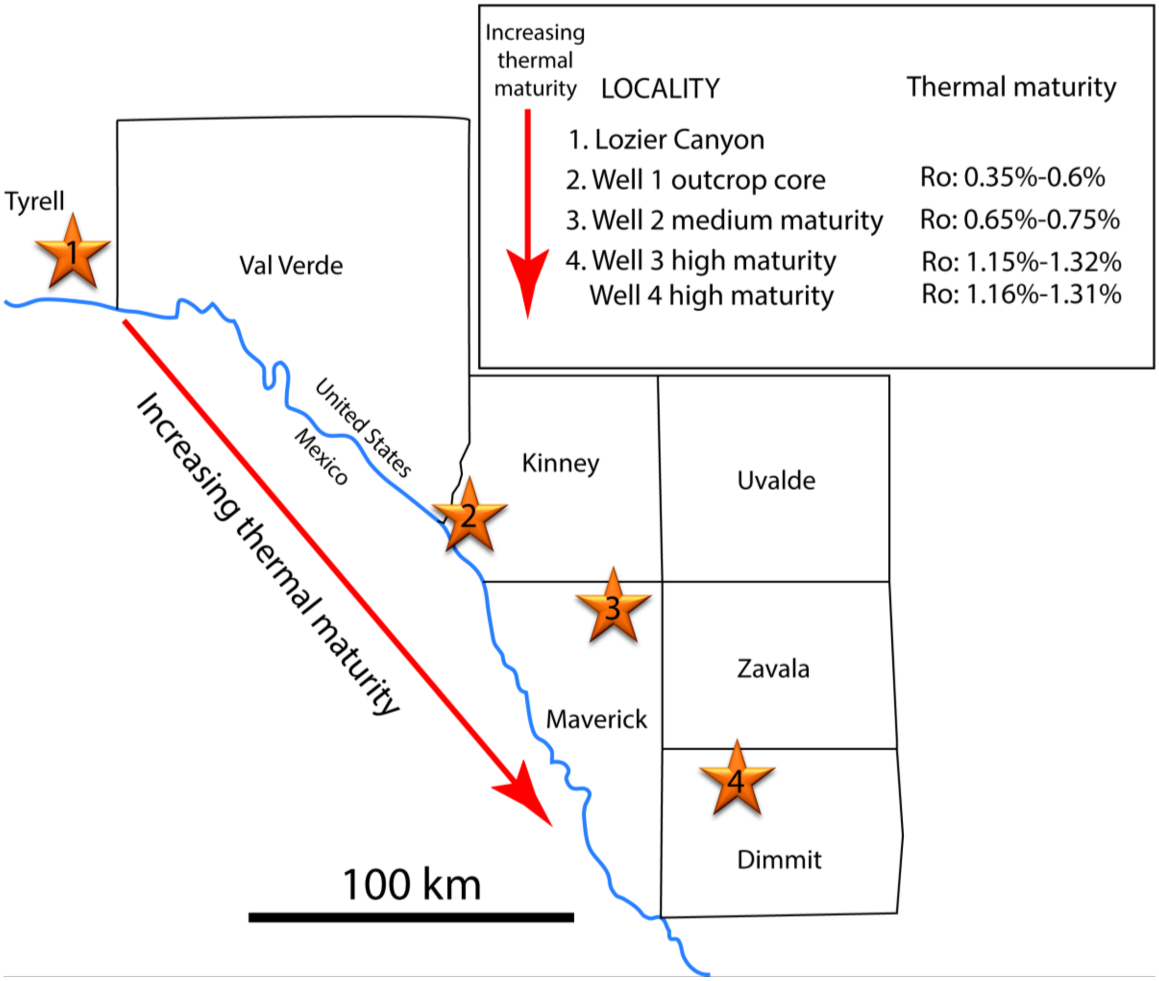

Figure 7: The map of South Texas showing the sample locations and thermal maturity levels. Note that actual thermal maturity (Ro) values are calculated based on organic geochemical thermal maturity indicators (Xun et. al., 2014).

THIN SECTION OBSERVATIONS

Fifty-two samples, which were obtained from both outcrop and core sampling, were sent to Spectrum Petrographics for thin sectioning. Thin section order was done according to scanning electron microscope specifications, which are standard size (27mm*46mm), 25 microns thick, and "probe-quality" polished. The uncovered polished sections are made by using surface impregnation with a low-viscosity medium before final polish to reduce mechanical damage (Milliken et. al., 2012(b)).

Petrographic analyses were performed across a range of magnifications (5x-5000x). The first step was to scan the slides with 4000-pixel/inch resolution by using the 3mm/APS (Ix240) Film Scanner (Nikon Scan SuperCoolScan5000ED). The textural variations (laminations and bioturbation) and relative contributions of clay-size and silt-size grained components were observed in these low magnification images. In order to observe lithological variations at the small scale (bed scale) (Macquaker and Howell, 1999) and to identify the intrabasinal grain assemblage, which includes macro-scale calcareous fossils, optical microscopy analyses were conducted. Eclipse LV 100 POL type light microscopy was used for this purpose and images were taken by using the software, NID Elements D 3.2 64-bit. Although, optical microscopy, which includes both plane-polarized light (PPL) and cross-polarized light (XPL) imaging gives important petrographic information about the general lithological and textural heterogeneity of the Eagle Ford, it is not sufficient for the detailed description of the grains if grain size is smaller than the thickness of thin section (Papazis, 2005). SEM and EDX systems give an opportunity to examine pores, to identify clay-size materials to some degree, and to examine the distribution of minerals within pores with the significantly higher magnification range (Welton, 1984).

The mixed siliciclastic and carbonate components in the Eagle Ford cause some imaging problems. Different luminescence properties of siliciclastic and carbonate minerals require the application of different petrographic and imaging techniques for the identification of authigenic and detrital minerals. Discrimination of quartz types as authigenic versus detrital can only be made with the application of SEM-based cathodoluminescence (CL) method instead of bulk mineralogical or chemical analyses. CL emittance of carbonate minerals is different from the silicate minerals, being generally brighter and more persistent (Reed and Milliken, 2003). Thus, carbonate minerals cannot generally be imaged using SEM-based cathodoluminescence (scanned CL). To overcome this problem, acquiring images using only the shorter wavelength by using a broadband, short wavelength filter is an option (Reed and Milliken, 2003).

Light-microscopy-based cathodoluminescence (CL) for carbonate minerals is applied (1) to make fabrics visible that are not visible by light microscopy (2) to infer cement sequences with the interpretation of equally luminescing zones, which are diagenetically coeval and so have a conclusion about cement stratigraphy, and (3) to make an interpretation about trace element content (Machel, 1985). Crystal defects are the other controls on luminescence, but of less pronounced importance (Machel, 1985). The most common trace elements that affect the intensity of luminescence in carbonate minerals are manganese (Mn) and iron (Fe). According to the enhancing and inhibiting properties of luminescence, trace elements are named as activators or quenchers, respectively. In terms of this definition, Mn is an activators and Fe is a quencher. Existence of Mn and absence of Fe causes more energetic luminescence (bright orange color), absence of both causes darker color and existence of both causes dull (middle-colored) color (Machel, 1985).

After separation of some carbonate-rich samples for conventional light microscope-based CL analyses (cold-cathode), the rest of the samples were prepared for FE-SEM analyses. For the FE-SEM, the sample is coated with a conductive material, in this case carbon (25-30 nm thick), in an evaporative coater. This coating is required to have a clear image of a sample but it should also be so thin that it does not hinder the identification of specific mineral (Welton, 1984). The intensity of the backscattered electron signal is associated with the atomic number of the elements whereas topographic information is detected by the secondary electrons in the system (Welton, 1984). For the FE-SEM imaging, all of the thin sections were analyzed using an FEI Nova NanoSEM 430 FE-SEM under high vacuum (15 KV accelerating voltage, sample current in the range of 1.4 nA). For having secondary and back-scattered images on SEM, spot size was used as 3 to 3.5, working distance was approximately 5 mm and aperture size was 30 µm. For each sample, low magnification image (~500x) for mostly for point counting purposes and high magnification image (~1000x-2000x) for detailed analysis of grain types and authigenic components are acquired.

X-ray mapping is used for additional observations, which are crucial to identify and characterize components (Milliken et. el., 2012(b)). Same thin sections, which are carbon coated for general FE-SEM imaging, are used for X-ray mapping as well. X-rays characteristic for individual elements are analyzed by using the energy dispersive system (EDS) detectors (twin Bruker X-flash 30 mm^2 SDD detectors; 15 KV accelerating voltage; spot size of 4-5; aperture 40 µm) and displayed as a 2D compositional map of the polished sample surface. Elements are selected to highlight particular minerals in distinct colors. Although X-ray mapping is sufficient for the discrimination of larger grains to allow an estimate of the classification, the resolution is still too low to allow full discrimination of clay-size minerals and nanopores. X-ray maps are stacked together above the secondary image to form a multi-layer image (Tovey and Krinsley, 1991). For instance, if the feature created by X-ray maps is rich in both iron and sulphur and low in other elements, the area is interpreted as representative of pyrite (Tovey and Krinsley, 1991).

For X-ray mapping Esprit 1.8 software is used and default parameters are changed. The parameters to acquire an image are defined as full map size, smooth-type map filter of seven and SE filter is set to 'sharpen'. X-ray mapping for Si, Ca, Al, K, Na, Mg, Fe, C, S, P, and Ti was performed for each sample with the ETD (secondary image) as a background. Also, some mixed X-ray maps including Na-Ca-Si/Na-Ca-Si-Fe/Na-Ca-Si-K/Na-Ca-Mg/Na-Ca-Mg-K/Na-Ca-Mg-Fe/Na-Ca-Mg-C were acquired to have knowledge about the detrital versus authigenics in terms of amount and type.

Differentiation of authigenic quartz from the primary quartz using luminescence properties in sandstone petrography firstly described in the study of Sippel, (1968). By analogy to sandstone, SEM-based cathodoluminescence (CL; Gatan ChromaCL detector) was also used to reveal the existence of authigenic quartz for the Eagle Ford in this study. SEM-based CL is mapping is a combination of trace elemental combination and crystal defect structure with variable color and intensity that is invisible in other types of imaging. CL mapping and the knowledge about crystal size, crystal shape and fabric reveal the different quartz types in mudrocks (Milliken, 1994; 2013).

Characterization and Quantification

Lithologic heterogeneity in mudrocks is controlled by the relative proportions of allochthonous, autochthonous and diagenetic components (Macquaker and Gawthorpe, 1993). In this study, allochthonous components and authochthonous components are classified as grains of either extrabasinal and intrabasinal origin. The main concern of the classification is the determination of the main components at the time of deposition rather than under the post-depositional conditions. Quantitative analysis for the purpose of classification excludes diagenetic components due to the fact that diagenesis should not drive the classification, but rather is the goal of prediction from classification. Not only authigenic components, but also pores, organic matter, and minor detrital compoents are excluded in the application of this classification method.

POINT-COUNTING

The point counting technique was described by Chayes (1956). According to Folk (1980), the most suitable way to accomplish point counting is laying out an equi-spaced grid to cover the thin section. The most significant point in applying this technique is randomness (Folk, 1980). The software J-Microvision is used for point counting by using the principle of random distribution of points. One of the main challenges was to choose the scale of X-ray maps to image particles of different sizes. Because grain size is not uniform for each sample, for the samples having dominantly sand- and silt-size particles, images at around 500x machine magnification are used; for the samples having finer-grained silt- and clay-size particles, images at 1000x are used (Figure 8). For the sample containing the sand-size calcite or dolomite crystals (mostly replaced facies) with fine-grained mostly clay-sized material in the interstices, images at two different scales are analyzed. Images at around 500x are used to quantify coarse-grained framework and images at 1000x or higher machine magnification are used to assess fine-grained material in the matrix. Point counting is applied to thirty-seven samples. Due the weathered nature of Lozier Canyon (LZ) and Comstock (CM) outcrop samples, those are not counted. Also, one sample from the low-maturity outcrop Well 1 and three samples from the high-maturity Well 4 are not counted because calcite replacement and quartz cementation are the main components of these samples. To identify relative contributions of extrabasinal and intrabasinal grain assemblages, six different categories are defined. Extrabasinal grains are categorized as quartz, lithics, feldspars, and clay plus mica. Intrabasinal grains are categorized as either calcareous allochems and biosiliceous grains (Figure 9).

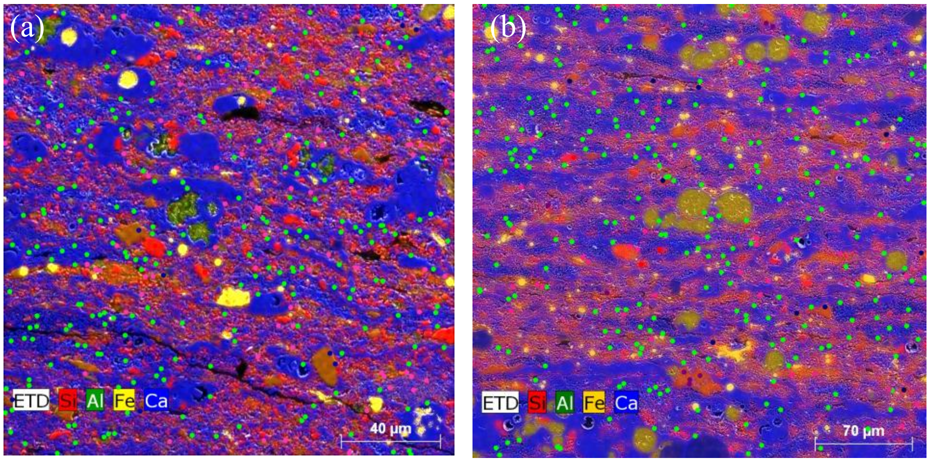

Figure 8: Images with approximately (a) 1000x and (b) 500x machine magnification used for point counting. Note that green dots and pink dots correspond to calcareous allochems and clay+mica, which are the dominant components in the Eagle Ford, respectively.

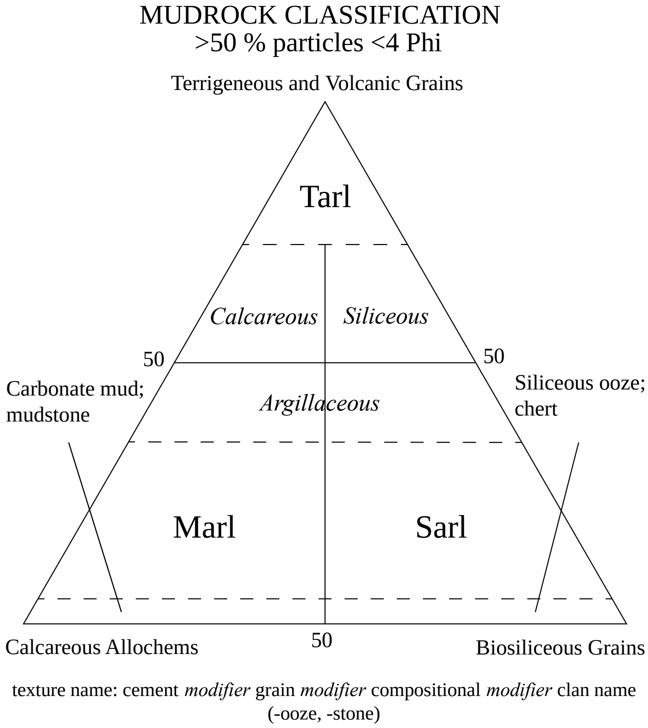

Figure 9: Classification diagram for mudrocks developed by Milliken (unpublished).

The classification can be approximately determined by using EDS X-ray mapping on an SEM, as it allows a more detailed description of the sample compared to conventional light microscopy. Grain type discrimination and grain boundary determination, which is necessary for the application of point count method, are greatly facilitated by X-ray mapping.

The key challenges of mudrock classification are (1) many clay-sized particles cannot be discriminated as to a detrital versus to an authigenic origin (2) discrimination of biosiliceous grains from detrital quartz and authigenic quartz is difficult. Some light microscopy, light microscopy-based CL images, and most X-ray maps reveal the existence of replaced biosiliceous debris in the Eagle Ford. Also, X-ray maps and SEM-based CL were helpful methods to discriminate authigenic microquartz dispersed in the matrix. However, CL could not be applied to the entire sample set due to the abundance of massively calcitized samples and some challenges remain unsolved. These challenges force some assumptions and interpretive results. For instance, although existence of biosiliceous grains (originally from radiolaria) is known, they are ignored for this classification due to the difficulty of discrimination within the Eagle Ford (Figure 10). Grain type proportions are determined relatively on the basis of calcareous allochems, and terrigeneous and volcanic grains due to excluding the biosiliceous grains for Eagle Ford classification. Samples were accumulated on the left edge of the triangle although they are realistically supposed to be plotted somewhat more towards more right due to the existence of biosiliceous grains.

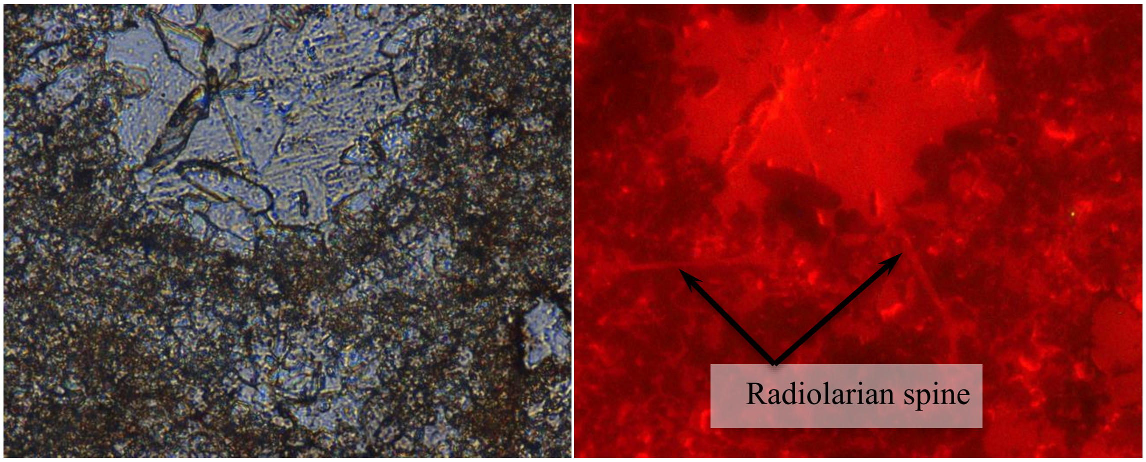

Figure 10: Replaced biosiliceous debris (radiolarian) is shown in the (a) transmitted plane-polarized light microscopy image and (b) light-microscopy based CL image of the low-maturity outcrop Well 1 sample 2 (149.52m)

XRD Data

For some of the low maturity and most of the medium-maturity and high-maturity well samples, XRD data was provided by Shell Oil Company (Table 2, Table 3, Table 4, and Table 5).

Table 2: XRD results of low maturity well samples

Sample NO	Depth (m)	CLAYS+MICA				CARBONATES		OTHER MINERALS								TOTALS		
		Chlorite	Kaolinite	Illite+I/S	Biotite	Calcite	Dolomite	Quartz	K-felds	Plag.	Feldspar	Pyrite	Marcasite	Gypsum	Barite	Clays+Mica	Carb.	Others
~22	57.3	0	0	0	0	98.4	0	1.5	0	0	0	0.1	0	0	0	0	98.4	1.6
~19	81.3	0.9	24.5	62.4	1.9	4.7	0.1	1.6	1.1	0.9	2	2	0.1	0	0	89.7	4.8	5.7
~18	88.9	0	0.7	10.8	0	76.4	0.5	5.1	3.5	1.4	4.9	1	0.7	0	0	11.5	76.9	11.7
~16	97.8	0	0	13.8	0	68.2	0.7	7.8	2.1	4.4	6.5	1.9	1.3	0	0	13.8	68.9	17.5
~15	98.3	0	2.6	31.7	0	53.7	0.2	1.2	0.2	3.7	3.9	5.3	0.3	1.2	0	34.3	53.9	10.7
~13	105.1	0	0	13.9	0	67.1	5.2	6	1.6	3.9	5.5	2.1	0.2	0	0	13.9	72.3	13.8
~12	110.2	0	0	15.6	0	64.3	0.8	11	2.4	3.8	6.2	1.3	0.8	0	0	15.6	65.1	19.3
~7	134.9	0	4.1	17.6	0	52.3	1.7	18.2	0	3.7	3.7	1.7	0.8	0	0	21.7	54	24.4
Average			4.0	20.7		60.6	1.2	6.6	1.4	2.7	4.1	1.9	0.5			25.1	61.8	13.1

Table 3: XRD results of medium-maturity well samples

Sample NO	Depth (m)	Depth (ft)	CLAYS				CARBONATES			OTHER MINERALS							TOTALS		
			Chlorite	Kaolinite	Illite	Mx I/S*	Calcite	Fe-dolomite	Siderite	Quartz	K-spar	Plag.	Feldspars	Pyrite	Apatite	Barite	Clays	Carb.	Other
CH1	911.2	2989.6	1	6	4	1	74	1	Tr	8	Tr	3	3	2	Tr	0	12	75	13
CH2	915.8	3004.5	1	9	8	3	55	1	Tr	14	1	6	7	2	Tr	0	21	56	23
CH3	950.2	3117.3	1	6	5	2	64	Tr	Tr	17	Tr	2	2	3	Tr	0	14	64	22
CH4	953.3	3127.6	Tr	1	1	Tr	82	0	Tr	15	Tr	1	1	Tr	Tr	0	2	82	16
CH5	963.9	3162.3	1	7	5	2	55	Tr	Tr	21	Tr	3	3	5	1	0	15	55	30
CH6	970.0	3182.4	1	7	5	2	60	1	Tr	17	Tr	3	3	3	1	0	15	61	24
CH7	973.1	3192.6	Tr	2	2	Tr	80	1	Tr	11	Tr	1	1	2	1	0	4	81	15
Average				5.4	4.3		67.1			14.7		2.7	2.9				11.9	67.7	20.4

Table 4: XRD results of high-maturity well samples

Sample NO	Depth (m)	Depth (ft)	CLAYS				CARBONATES			OTHER MINERALS								TOTALS		
			Chlorite	Kaolinite	Illite	Mx I/S*	Calcite	Dolomite	Siderite	Quartz	K-spar	Plag.	Feldspars	Pyrite	Apatite	Marcasite	Barite	Clays	Carb.	Other
EF3 1-31	2524.8	8283.5	Tr	Tr	14	1	62	1	Tr	15	1	5	6	1	Tr	Tr	0	15	63	22
EF3 1-61	2533.9	8313.3	Tr	Tr	12	1	54	1	Tr	23	1	6	7	2	Tr	Tr	0	13	55	32
EF3 1-66	2535.4	8318.2	Tr	Tr	5	Tr	77	1	Tr	12	Tr	4	4	1	Tr	0	0	5	78	17
EF3 1-136	2556.7	8388.1	3	Tr	11	1	67	0	Tr	8	Tr	4	4	2	2	2	0	15	67	18
Average					10.5		65.0	0.8		14.5		4.8	5.3	1.5				12.0	65.8	22.3

Table 5: XRD results of high maturity well samples

Sample NO	Depth (m)	Depth (ft)	CLAYS				CARBONATES			OTHER MINERALS							TOTALS		
			Chlorite	Kaolinite	Illite	Mx I/S*	Calcite	Dolomite	Siderite	Quartz	K-spar	Plag.	Feldspars	Pyrite	Apatite	Barite	Clays	Carb.	Other
EF4 1-5	2775.1	9104.5	Tr	Tr	13	5	57	Tr	Tr	15	1	5	6	4	Tr	0	18	57	25
EF4 1-10	2776.5	9109.3	Tr	Tr	9	3	62	Tr	Tr	15	1	5	6	5	Tr	0	12	62	26
EF4 1-25	2781.1	9124.3	Tr	Tr	19	3	53	1	Tr	11	1	5	6	6	1	0	22	54	24
EF4 1-35	2784.1	9134.1	Tr	Tr	4	Tr	83	Tr	Tr	10	Tr	1	1	1	1	0	4	83	13
EF4 1-75	2796.3	9174.1	1	Tr	10	2	58	Tr	Tr	21	1	3	4	4	Tr	0	13	58	29
EF4 1-80	2797.8	9179.0	Tr	Tr	3	Tr	77	5	Tr	11	1	2	3	1	Tr	0	3	82	15
EF4 1-90	2800.9	9189.3	3	Tr	11	2	55	Tr	Tr	21	Tr	3	3	4	1	0	16	55	29
EF4 1-100	2803.9	9199.0	Tr	Tr	5	Tr	74	2	Tr	15	Tr	2	2	1	1	0	5	76	19
Average					9.3		64.9			14.9		3.3	3.9	3.3			11.6	65.9	22.5

RESULT

Grain Assemblages

BACKGROUND

Unconsolidated muds and consolidated mudstones are mixtures of siliciclastic, biosiliceous, and carbonate material in both modern and ancient deposits. Grain types described in the sandstone and limestone literature are grouped as (1) non-carbonate extrabasinal grains (typical framework of the sandstone) (Gazzi, 1966; Gazzi et.al., 1973), (2) carbonate extrabasinal (derived from an uplifted carbonate source terranes) (Gazzi and Zuffa, 1970; Zuffa, 1980; Milliken and Land, 1993), (3) non-carbonate intrabasinal (biosiliceous debris, glauconite, gypsum, etc.) (Folk, 1980) and (4) carbonate intrabasinal (typical framework grains of limestone) (Folk, 1959, 1962, and 1980). These grain types can all be observed in fine-grained sedimentary rocks. According to Folk (1980), it is essential to discriminate mineral composition of sedimentary rocks as (1) terrigeneous minerals (2) chemical minerals including (2a) allochemical minerals (transported) and (2b) orthochemical minerals (forming in place). Although generally, intrabasinal to extrabasinal type grain discrimination is applied to mudrocks (e.g., Milliken et al., 2012 (b)), partitioning of mineral components across these categories can be challenging because, a given mineral can be present as grains derived from both extrabasinal and intrabasinal (allochemical or authigenic) sources.

Similar to mineral grains, organic matter can also be both intrabasinal and extrabasinal in origin. Kerogen can be derived from plant materials including algae, and higher plants as well as zooplankton, of both terrestrial and marine origin (Tissot and Welte, 1984; Vandenbroucke and Largeau, 2007). Variations in depositional environment also influence organic matter type and preservation (Huc et. al., 1990; Vandenbroucke and Largeau, 2007). Kerogen composition varies with the detrital assemblage and chemical modifications in the subsurface during diagenesis (Vandenbroucke and Largeau, 2007; Tissot and Welte, 1984). Total organic carbon (TOC) measures the amount of carbon bound in an organic compound (Spaw, 2012). TOC measurements include both detrital organic matter (both intrabasinal and extrabasinal) and bitumen; hence, TOC can be considered as inappropriate to measure detrital organic matter content in some rocks.

EXTRABASINAL GRAINS

Extrabasinal grains are derived from outside of the basin of deposition. They formed by chemical and mechanical breakdown of older sedimentary rocks and transported into basin through a variety of processes (Folk, 1980). The following extrabasinal grain types are observed in the Eagle Ford sample set.

Quartz

The detrital nature of quartz in the Eagle Ford mudrocks is established through a combination of light microscopy (Figure 11), X-ray mapping (Figure 12 and Figure 13), and CL imaging. Quartz of extrabasinal origin shows angular shape and variable cathodoluminescence (CL) intensity and color (Milliken, 2013). Subangular to angular monocrystals of detrital quartz, which are mostly silt-size are present almost all samples of the Eagle Ford.

The average bulk quartz percentage, which includes quartz of both detrital and authigenic origins, is 6.6, 14.7, 14.5, and 14.9 percent in the XRD results for Well 1 (low maturity outcrop), Well 2 (medium-maturity), Well 3 (high-maturity) and Well 4 (high-maturity) samples, respectively (Table 2, Table 3, Table 4, and Table 5). Average values for detrital quartz determined from point-counting are 1.8, 0.95, 2.25, and 3 (Table 10, Table 11, Table 12, and Table 13) from the same wells, respectively.

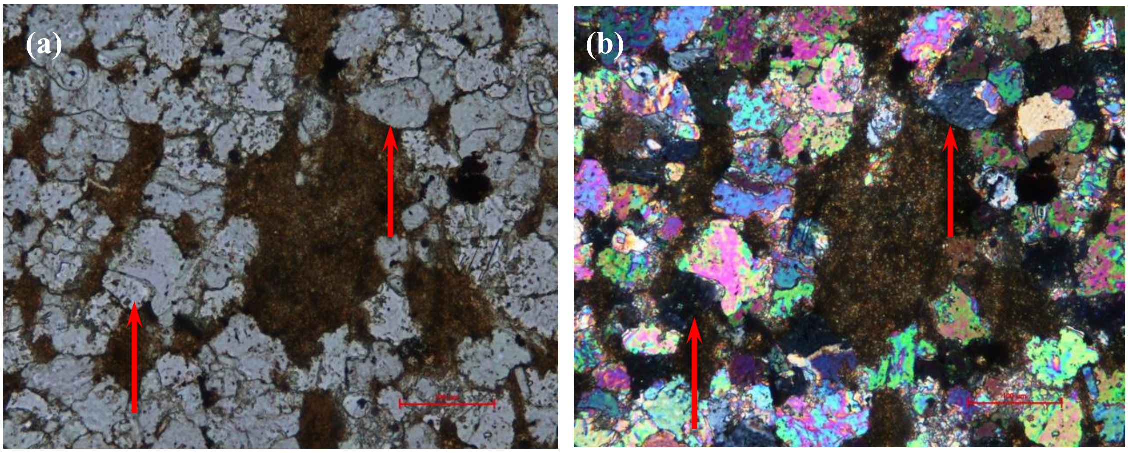

Figure 11: Detrital quartz grains are shown in transmitted (a) plane-polarized (b) cross-polarized light image of the outcrop Lozier Canyon LZ-6 sample.

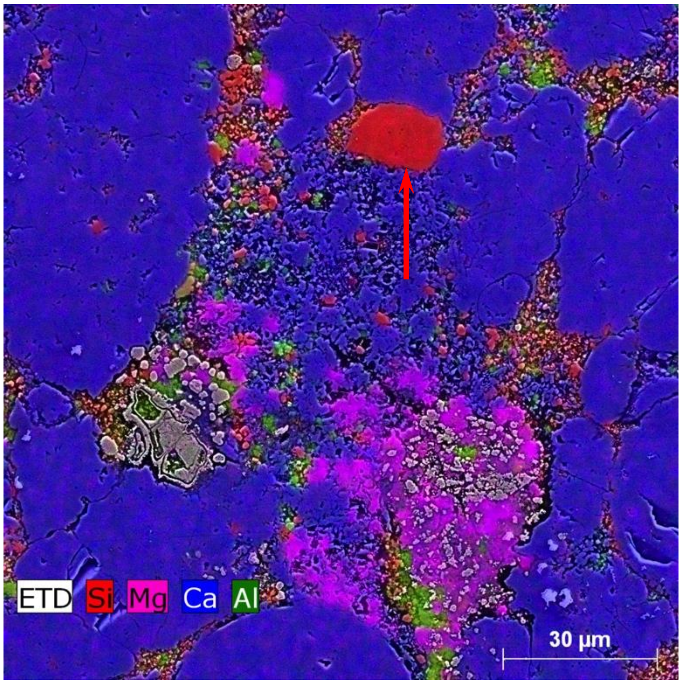

Figure 12: Detrital quartz grain is shown in the EDS X-ray map of the outcrop Lozier Canyon LZ-6 sample. Note that general views of the same sample, showing detrital quartz grains between the recrystallized calcite, are shown in both light microscopy (Figure 11) and X-ray map (Figure 12).

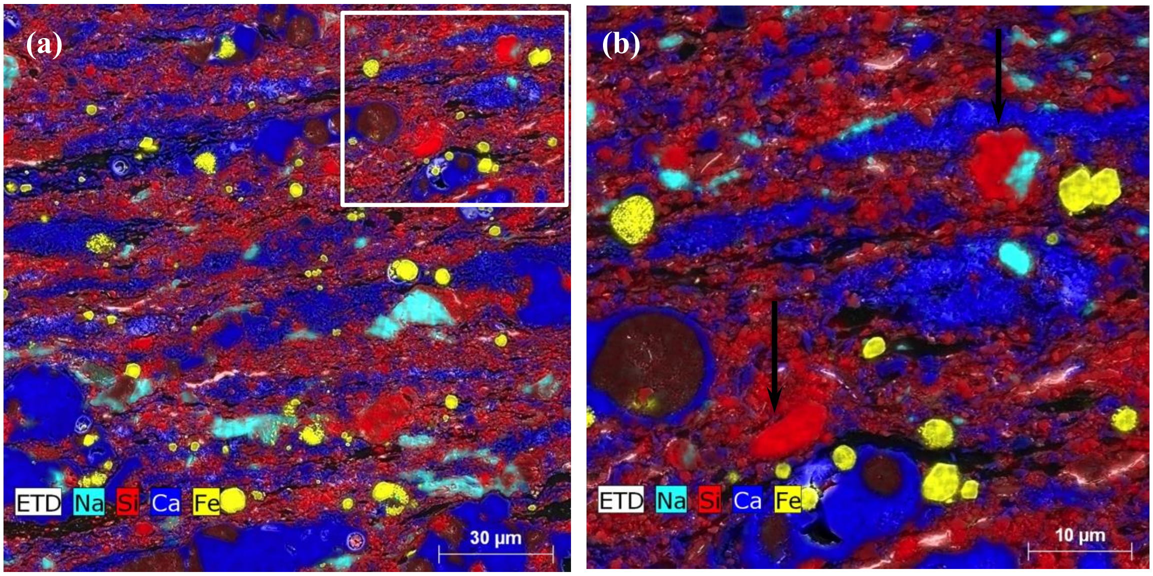

Figure 13: Silt- to clay-size angular to sub-angular detrital quartz grains (red) are shown in the EDS X-ray map of (a) 1000x machine magnification image (b) higher machine magnification (~3000x) image of the low-maturity outcrop Well 1 sample 7. Bright blue is carbonate (calcite and minor dolomite); aqua is Na-feldspar, yellow is pyrite. Note that black arrows indicate detrital quartz in the higher magnification image.

Feldspars

Detrital feldspar including plagioclase and K-feldspar are identified in almost all samples of the Eagle Ford (Figure 14 and Figure 15). Silt- to clay- size feldspars in the Eagle Ford, are similar to detrital quartz in terms of size. Detrital feldspars are sub-rounded to sub-angular in shape. K-feldspar is mostly observed in the shallower, low-maturity outcrop samples whereas albite (Na-plagioclase) is more abundant in the deeper medium- and high-maturity samples, consistent with the studies of Milliken (1992) in Gulf Coast mudstones, and others studies in sandstones (Land and Milliken, 1981; Boles, 1982 and Milliken, 1989) that document the high reactivity of feldspars in burial diagenesis.

XRD results confirm that the majority of feldspars are plagioclase whereas K-feldspars are dominantly observed as trace except for low maturity outcrop Well 1 samples. The average total feldspar values of Well 1, Well 2, Well 3, and Well 4 are 4.1, 2.9, 5.3, and 3.9 percent (Table 2, Table 3, Table 4, and Table 5), respectively, almost five times less than the total quartz percentage in Eagle Ford samples. When point count results are analyzed, however, it becomes apparent that detrital quartz and feldspar amounts do not differ substantially (Table 11, Table 12, and Table 13). The contrast with the XRD data relates to the abundance of authigenic quartz, which derives from alteration of the intrabasinal bio-siliceous detritus (below).

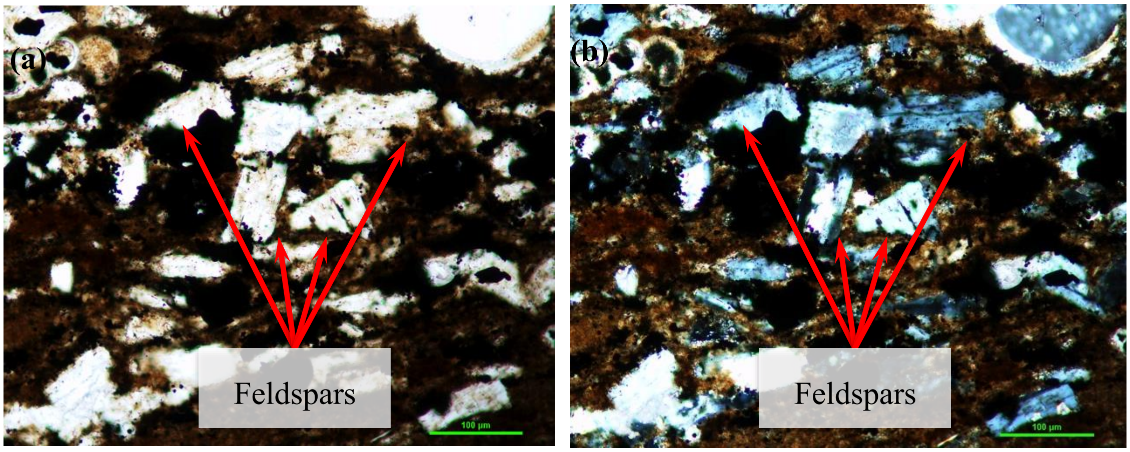

Figure 14: Feldspars are shown in transmitted (a) plane-polarized (b) cross-polarized light image of medium-maturity Well 2 sample CH3. Note that it is extremely difficult to confirm an authigenic (replacement) versus detrital feldspar using light microscopy. The size, angularity, and spatial distribution of these feldspars support a detrital origin.

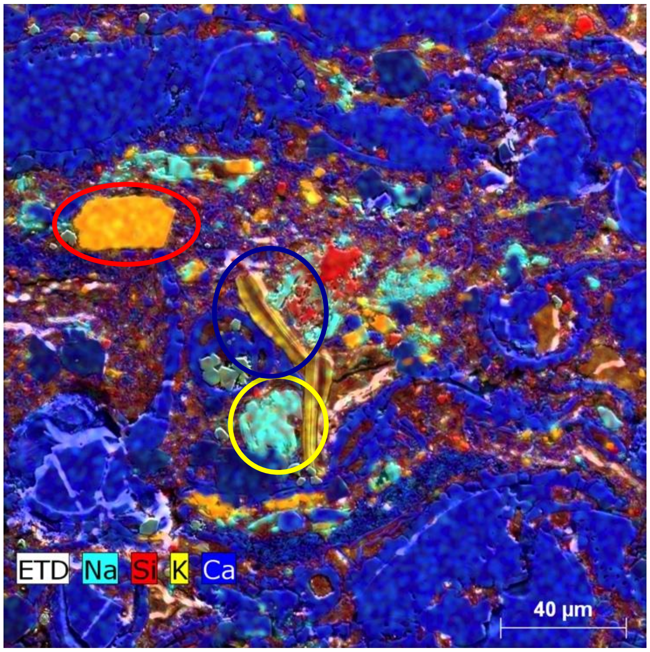

Figure 15: Detrital K-feldspar (bright yellow, shown in red circle), detrital albite (aqua, shown in yellow circle), and detrital mica (pale yellow) (shown in dark blue circle) are shown in the EDS X-ray maps of the low-maturity outcrop Well 1 sample 13 (106.47-106.44)

Lithic grains

Lithic fragments, which are mostly polycrystalline aggregates are also observed in the Eagle Ford. Grain size of lithic fragments is mostly sand- to silt- size, somewhat larger than quartz and feldspar. Lithic grains are sub-rounded to sub-angular. This most common lithic type is a combination of K-feldspar and albite crystals. These are likely felsitic volcanic-lithic fragments (Figure 16).

In XRD results showing bulk composition, lithic-type detrital grains cannot be differentiated although their presence affects the total feldspar percentage. Point counts reveal that almost all Eagle Ford samples have lithic fragments.

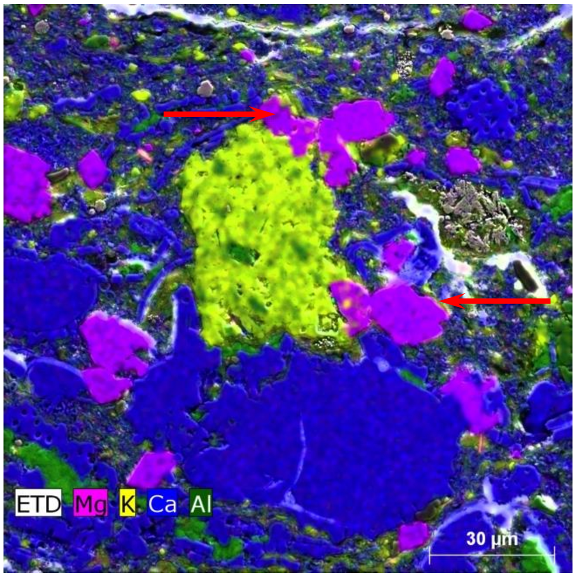

Figure 16: Lithic fragment composed of both K-feldspar (yellow) and albite (greenish) is shown in the EDS X-ray map of the low-maturity outcrop Well 1 sample 13. Note that dolomite that is partially replacing the lithic fragment is also indicated with red arrows.

Clay and Mica

By volume, the main extrabasinal components in the Eagle Ford are detrital clay minerals. Because they are clay-size, discrimination of authigenic as opposed to detrital clay is problematic. Coarser crystals of clay that fill former pore space, e.g., kaolinite in foraminifer tests, are clearly authigenic; however clay in the form of pore-filling material is only a small portion of the total clay.

Detrital mica minerals exist in some of the low-maturity Well 1 samples (Figure 17). In light microscopy, they can be discriminated easily by their shape and composition (K- or Mg-rich) (Figure 18). The flaky shape and dark color in light microscopy and K and Mg content observed in EDS X-ray maps indicate that some of the mica is biotite.

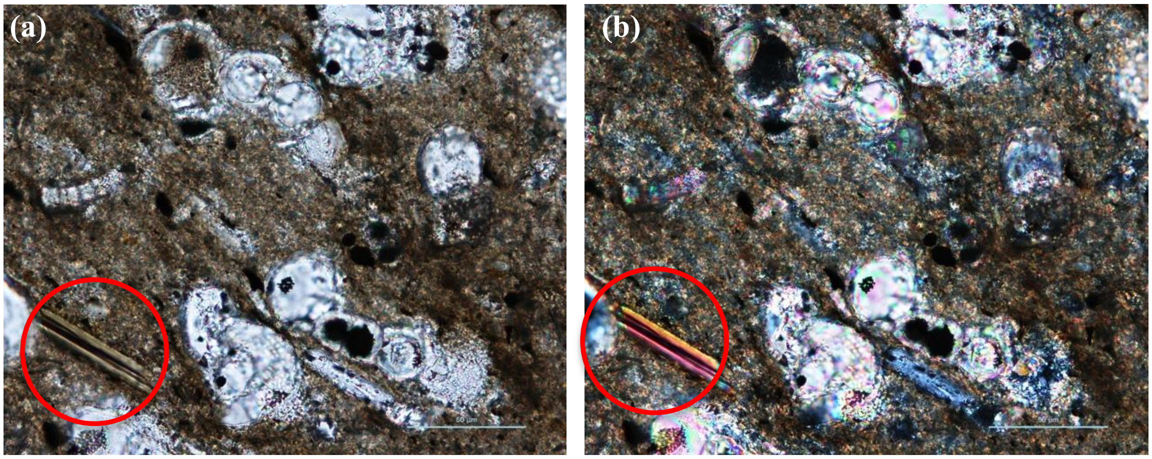

Figure 17: Biotite grain is shown in transmitted (a) plane-polarized (b) cross-polarized light image of the low-maturity outcrop Well 1 sample 14. (104.86-104.83m)

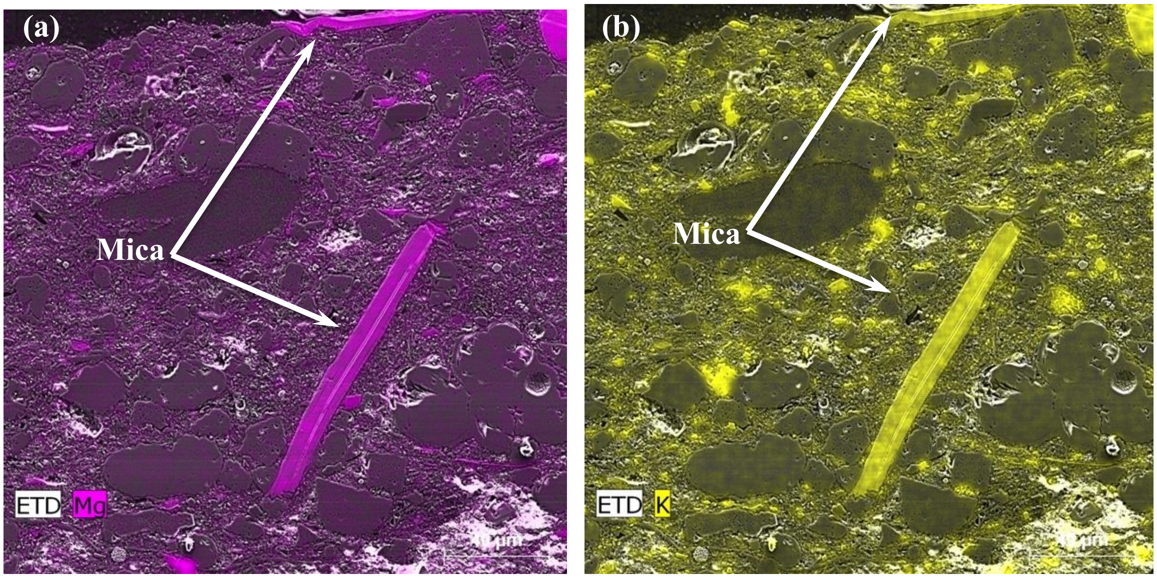

Figure 18: Biotite grains are shown (a) in the EDS X-ray Mg-map (b) in the EDS X-ray K-map of the low-maturity outcrop Well 1 sample 19 (81.28m). Note that Fe- content is observed in addition to Mg and K, indicating that the mica is biotite.

Organic matter

Organic matter can also be derived from extrabasinal or intrabasinal sources or it can be authigenic, formed during diagenesis (Tissot and Welte, 1984; Vanderbroucke and Largeau, 2007). Two types of organic matter are present in the Eagle Ford, a particulate-type organic matter (kerogen) (Figure 19 and Figure 20) and pore-filling bitumen (Fishman et. al., 2013; Jennings and Antia, 2013).

Extrabasinal type organic matter defined in the Eagle Ford is sharp-edged, curved shaped woody fragments, which are formed as a result of the fragmentation of the porous cellulosic structure of wood (Tissot and Welte, 1984). The discrimination of marine kerogen and terrigeneous kerogen can be made according to the different compaction and deformation behavior. Marine kerogen is more deformed due to compaction compared to terrigeneous kerogen (Milliken et. al., 2013; Milliken et al., 2014). Detrital organic matter is mostly widely distributed in the matrix of the Eagle Ford and few isolated nanopores and micropores are identifiable in the detrital organic matter (Dawson and Almon, 2010, Pommer, 2014). However, organic matter-hosted pore development is associated with the organic matter formed during thermal maturation (further discussion below).

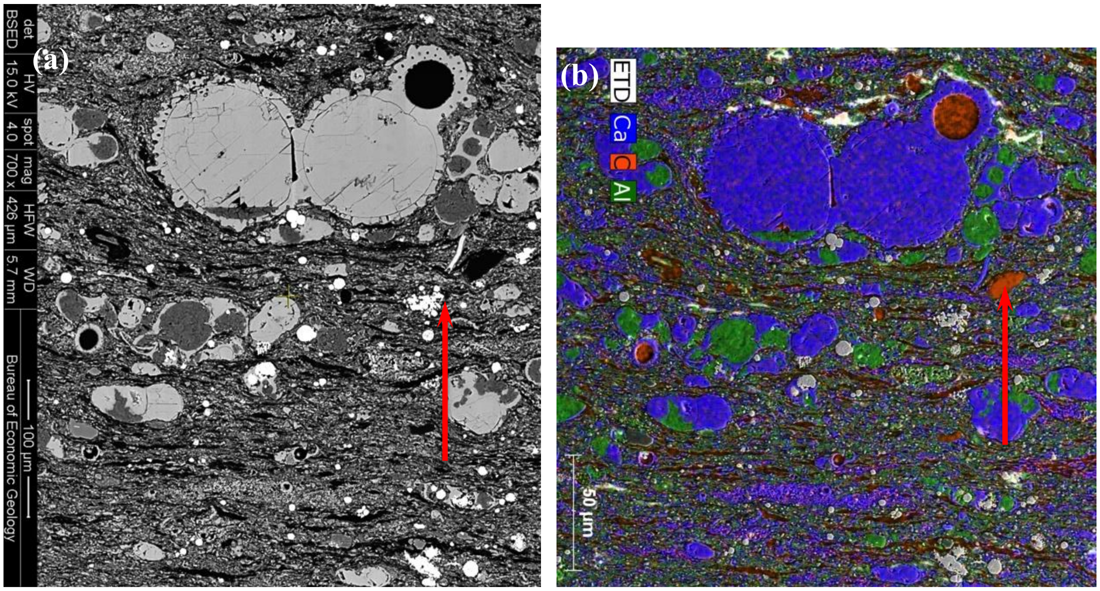

Figure 19: Particulate organic matter (red arrows) in the Lower Eagle Ford (LEF) is shown in the (a) BSED (b) EDS X-ray maps of the low-maturity outcrop Well 1 sample 1 (151.88-151.85m). In the EDS map, organic matter, mapped in orange, is also widely dispersed between mineral grains and also fills the foraminifer test, upper right.

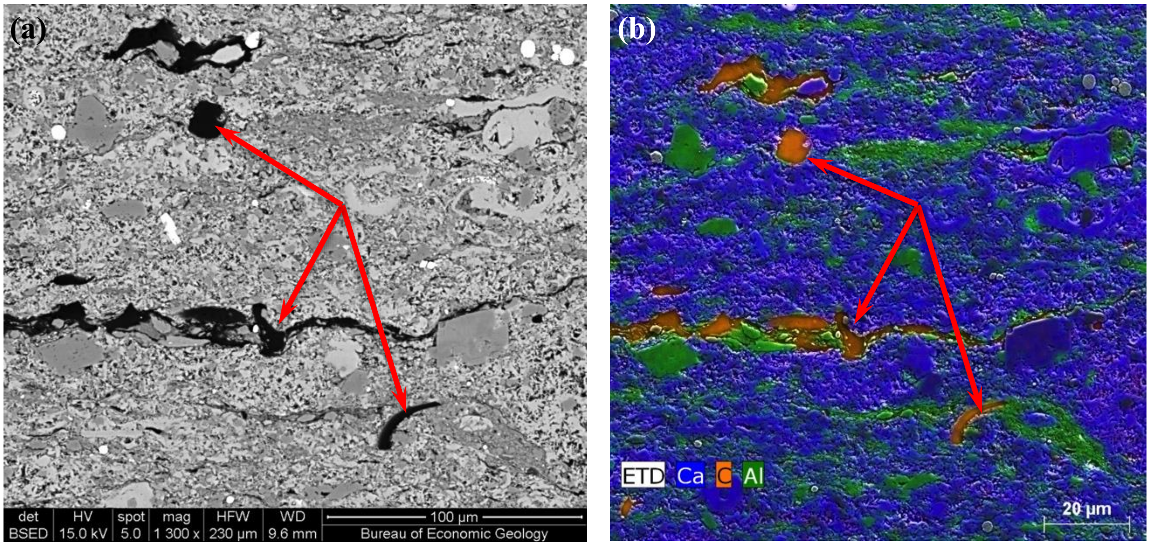

Figure 20: Particulate organic matter (red arrows) is shown in the (a) BSED (b) EDS X-ray map of the medium-maturity Well 2 sample (950.24 m)

INTRABASINAL GRAINS

Intrabasinal grains including skeletal fragments, sediment aggregates, and organic matter are formed within the basin of deposition. These grains are subdivided into calcareous fossils, non-calcareous fossils (including radiolaria and vertebrate debris), carbonate aggregates, phosphatic intraclasts (Table 6, Table 7, Table 8, and Table 9), and organic matter. The Eagle Ford is rich in intrabasinal grains. They are most easily identified using light microscopy because internal structures of fossil fragments can be observed.

Calcareous Fossils

Dominant calcareous fossils (Table 6, Table 7, Table 8, and Table 9) in Eagle Ford include pelagic foraminifers (Fig. 19), benthic foraminifers (Figure 21), inoceramids (Figure 22), oysters (Figure 25), echinoderms (Figure 23), thin-walled mollusks (Figure 24), and calcispheres (Figure 23). The most common calcareous fossils are pelagic foraminifers and inoceramids. Pelagic foraminifers are observed in all samples coming from different parts of the basin. Amounts of calcareous fossils vary and are a noticeable contributor to the calcareous allochem percentage and thereby classification; however, there is not any systematic change observed in the type of calcareous fossils. Oysters, echinoderms, and calcispheres are rare compared to others although where they occur they are mostly well-preserved. Calcareous fossils and carbonate aggregates are counted as calcareous allochems for the purpose of classification.

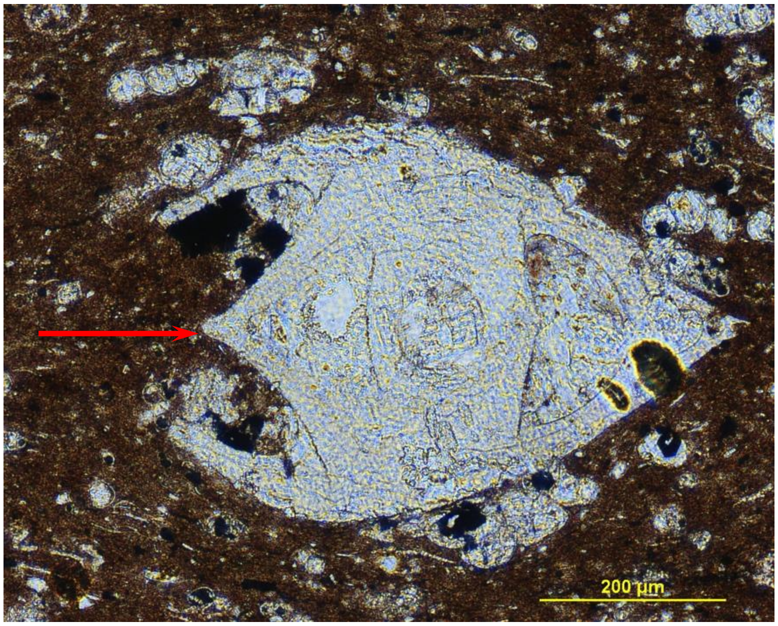

Figure 21: Benthic foraminifer shown in transmitted plane-polarized light image of high-maturity Well 4 sample (2780.43 m)

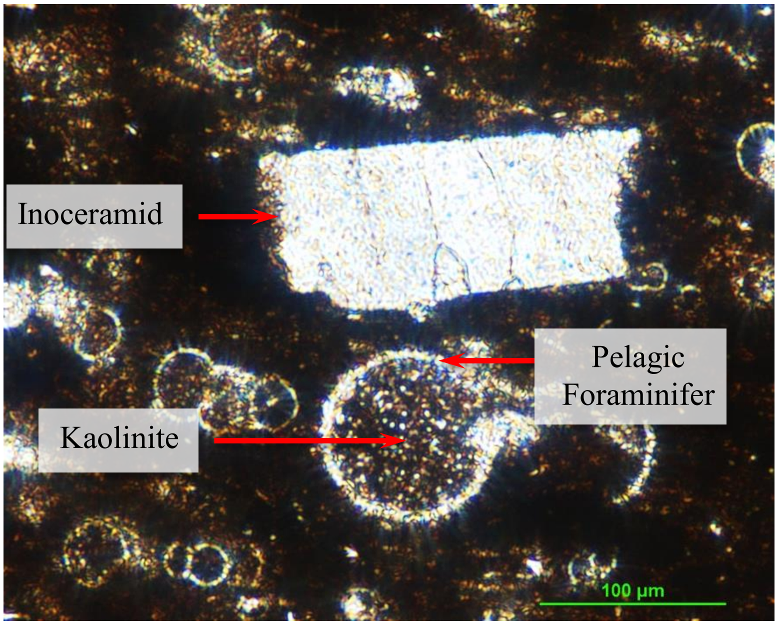

Figure 22: Fractured inoceramid plate and kaolinite infilling globigerinid pelagic foraminifer are shown in transmitted plane-polarized light image of high-maturity Well 4 sample (2809.49m)

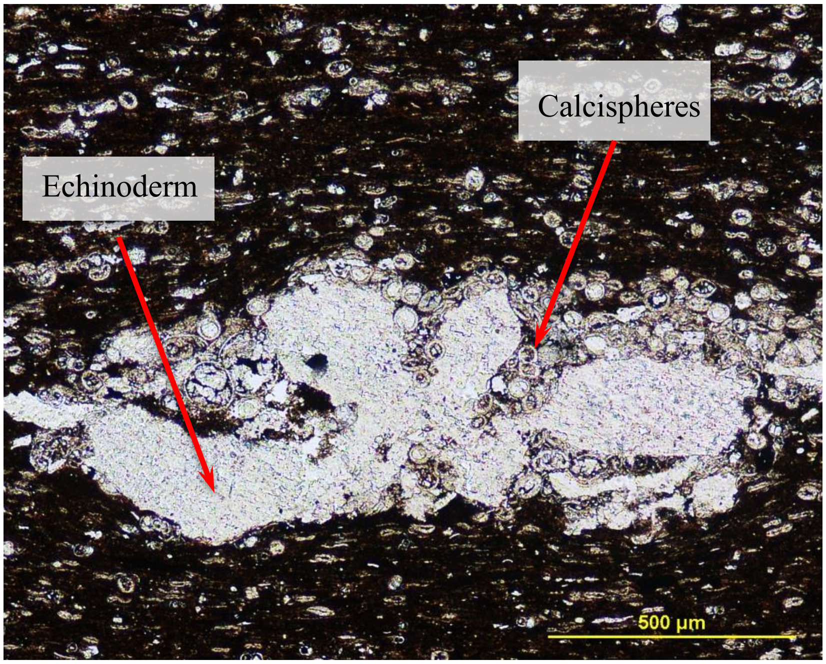

Figure 23: Echinoderm and calcispheres is shown in transmitted plane-polarized light image of high-maturity Well 4 sample (2781.1m)

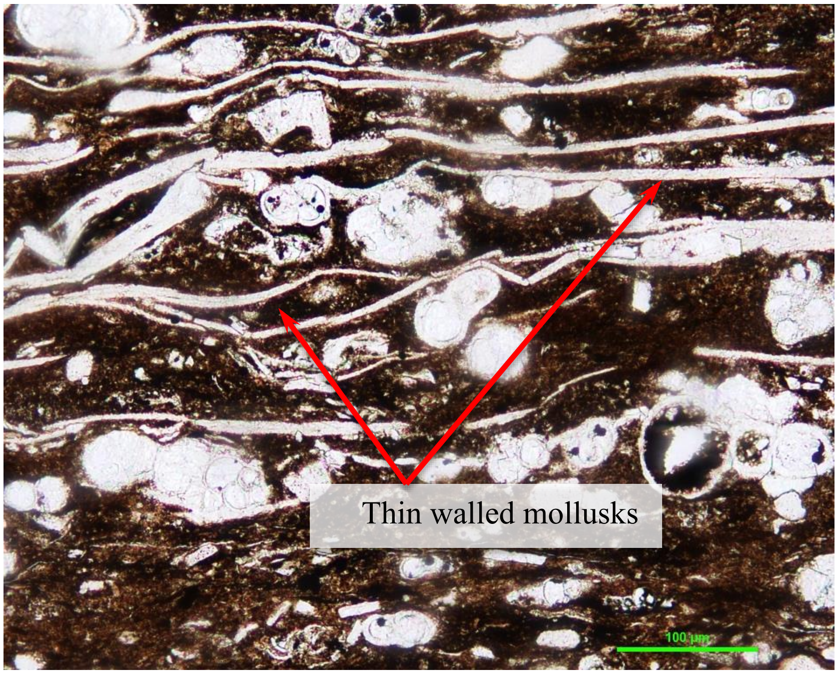

Figure 24: Thin-walled mollusks are shown in transmitted plane-polarized light image of high-maturity Well 3 sample (2529.3 m)

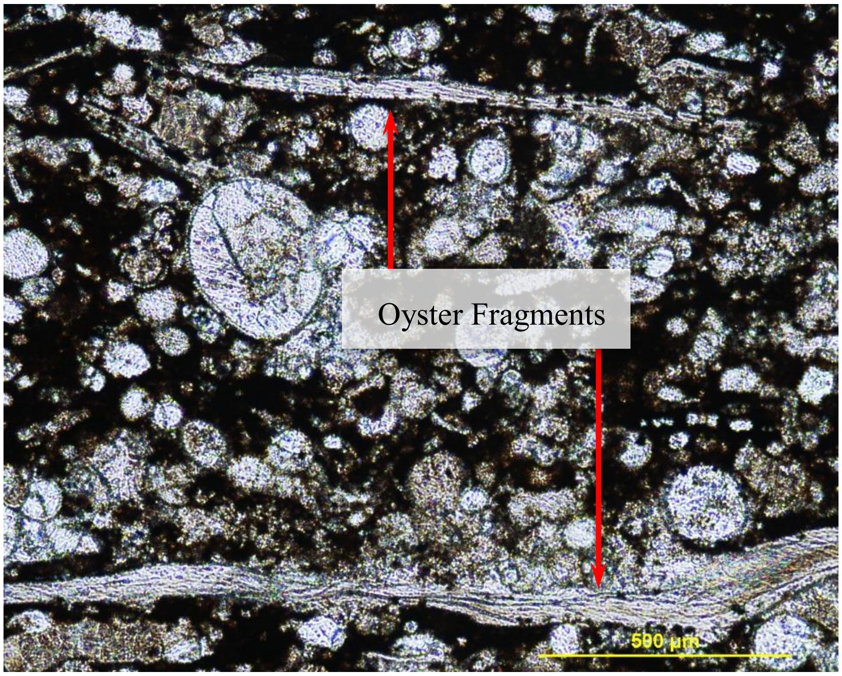

Figure 25: Oyster fragments (red arrows) shown in transmitted plane-polarized light image of high-maturity Well 3 sample (2535.4 m)

Non-Calcareous Fossils

Variable amounts of non-calcareous fossils are present in the Eagle Ford. The main types are phosphatic fossils and calcified radiolarian (Table 6, Table 7, Table 8, and Table 9).

The yellow color and isotropic nature of phosphate particles makes them easy to discriminate using light microscopy under cross-polarized light. Two different types of phosphate-rich particles, fossiliferous and non-fossiliferous, are present in the Eagle Ford. Fossil phosphate is present in the form of fish bones and teeth. Naturally occurring pore spaces of phosphatic fossils are filled with kaolinite, calcite (Figure 26 and Figure 27), and other authigenic minerals (Figure 28), similar to the cementation observed within foraminifers. Some of the phosphate fragments are crushed and broken into smaller pieces due to their brittle nature (Figure 29). Phosphatic bone and teeth are commonly observed in the low-maturity outcrop samples whereas; phosphatic intraclasts and authigenic phosphate precipitation are more common in the high-maturity Well 3 and 4 samples (below). Radiolaria are challenging to identify because they are mostly replaced by calcite. Radiolarians are discriminated by their spines and discrete, porous shell structure (Figure 30) using a combination of light microscopy, light-microscope-based CL and also X-ray mapping (Figure 31, Figure 32, and Figure 33). Originally composed of amorphous silica (biogenic opal) they are recrystallized to more stable quartz forms or replaced by other minerals in Pre-Tertiary specimens (Scholle and Ulmer-Scholle, 2003), mostly calcite in the Eagle Ford.

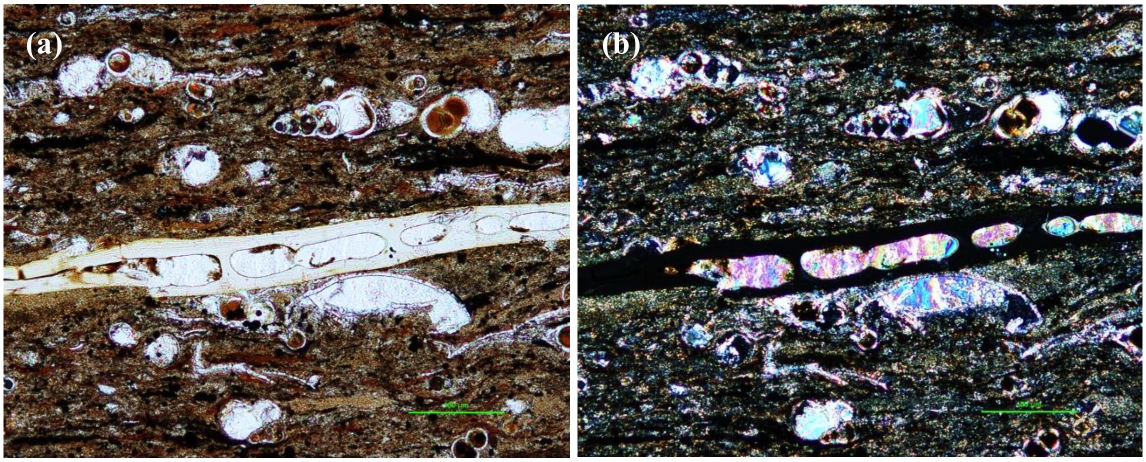

Figure 26: Phosphatic fossil with calcite cement inside the pores is shown in transmitted (a) plane-polarized (b) cross-polarized (isotropic and black in color) light image of the low-maturity outcrop Well 1 sample 4 (139.88-139.85m)

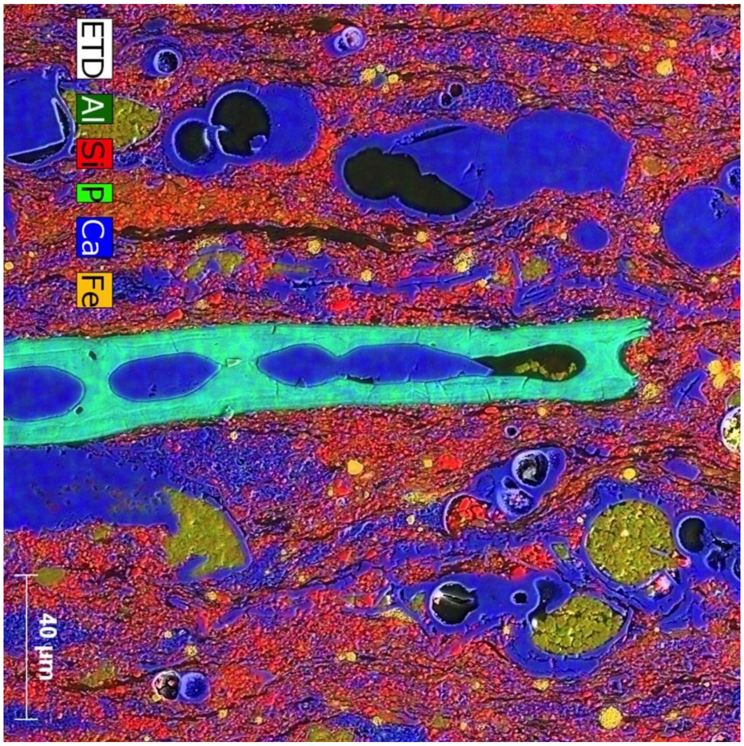

Figure 27: Phosphatic fossil (fish teeth/bone) and calcite & kaolinite precipitation inside the pores is shown in the EDS X-ray map of the low-maturity outcrop Well 1 sample 4 (139.88-139.85m)

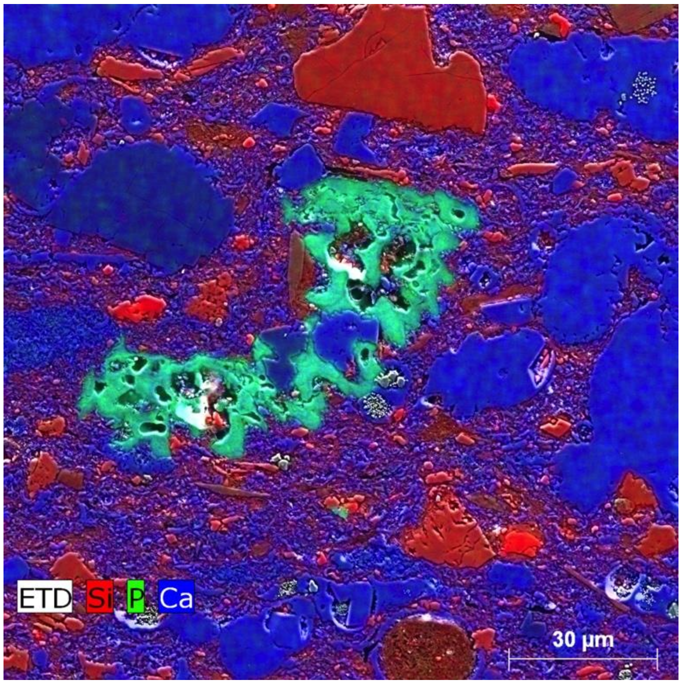

Figure 28: Phosphatic fossil (fish teeth/bone) and pore space filling calcite and dolomite cement is shown in the EDS X-ray map of the low-maturity outcrop Well 1 sample 21 (69.88-69.85m).

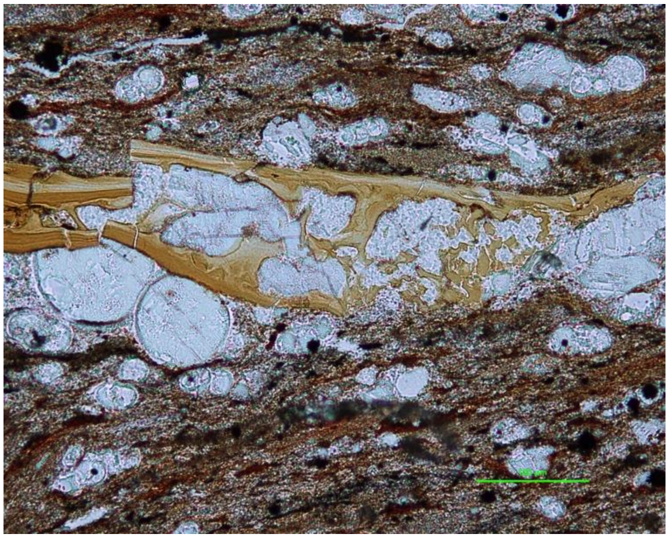

Figure 29: Crushed phosphatic grain and calcite cement filling primary intragranular pores, shown in transmitted plane-polarized light image of the low-maturity outcrop Well 1 sample 7 (133.71-133.68)

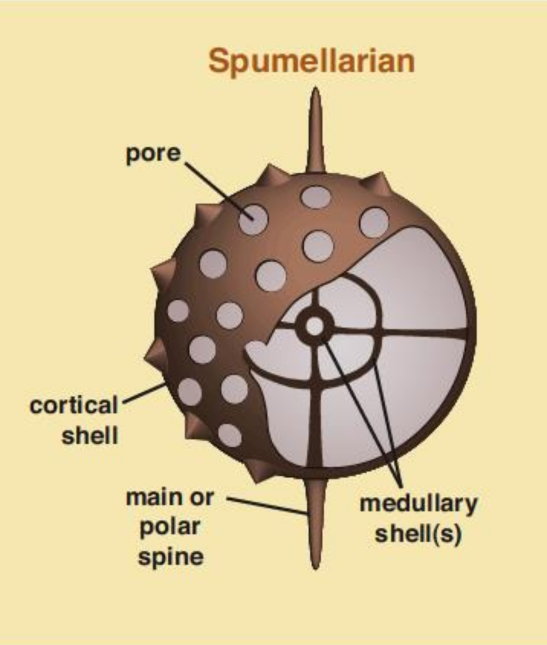

Figure 30: Diagram showing internal and external morphologic features of a spumellarian radiolaria skeletal type (from Scholle and Ulmer-Scholle, 2003).

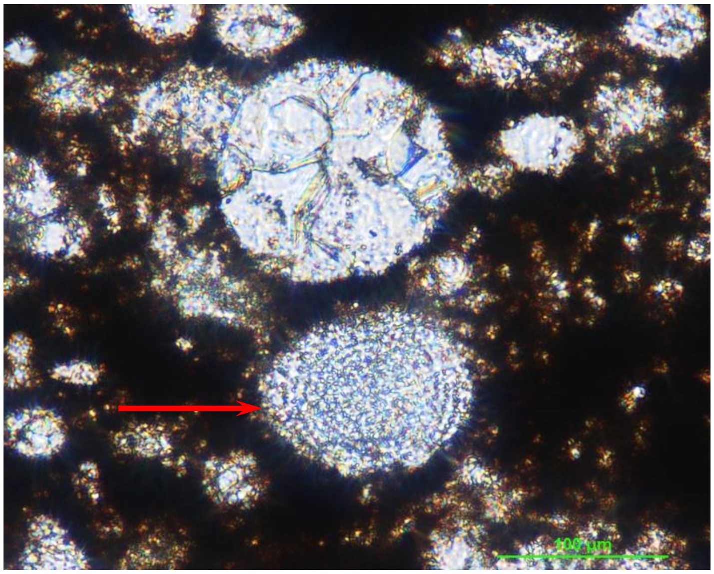

Figure 31: Radiolaria (internal structure and porous walls can still be discriminated)(red arrow) replaced with calcite, shown in transmitted plane-polarized light image of the high-maturity Well 4 sample (2776. 62m)

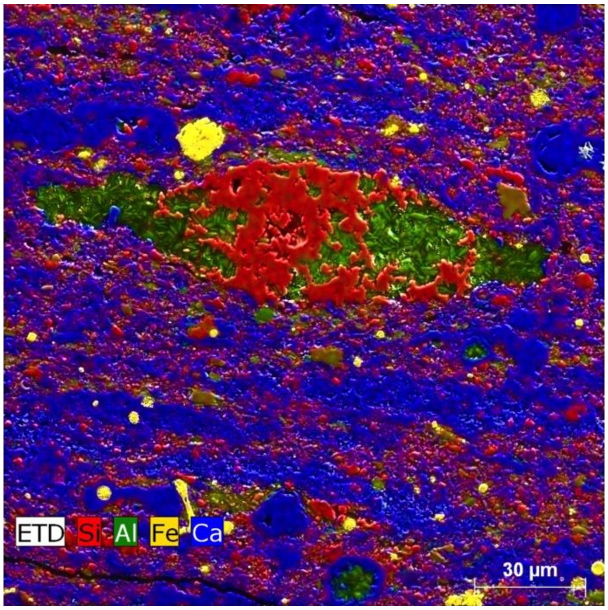

Figure 32: Remnants of dissolved biosiliceous grain (radiolaria) partially replaced by quartz (red) with internal pore space filled partly by kaolinite (green) and partly by Mg-chlorite (explained further below) is shown in the EDS X-ray map of the high-maturity Well 4 sample 1-5 (2775.04 m)

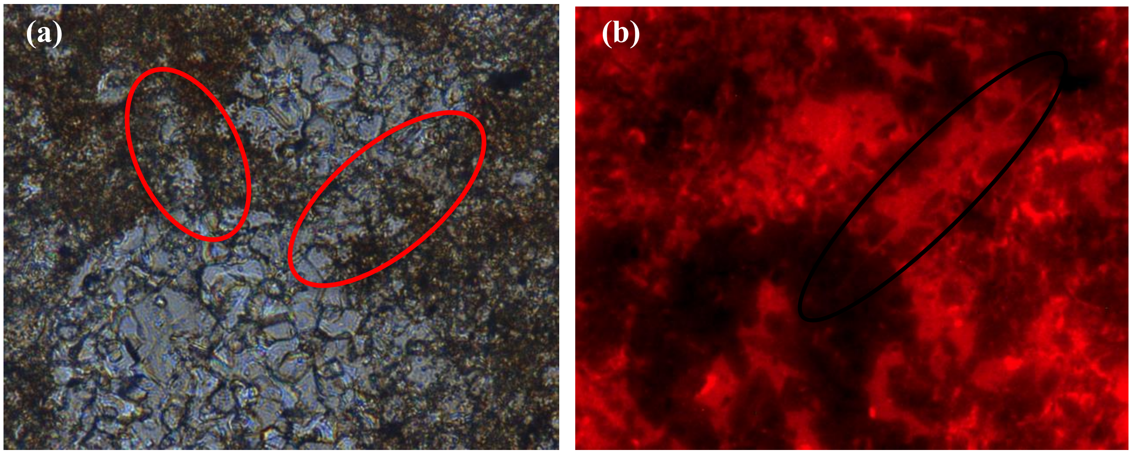

Figure 33: Replaced biosiliceous grains (radiolaria) with spines, shown in the (a) transmitted plane-polarized light image, and (b) CL image (identified with the bright orange luminescence properties) of the low-maturity outcrop Well 1 sample 2 (149.52-149.49m)

Carbonate Aggregates

Fecal pellets and coccolith-rich lenses within the Eagle Ford are classified here as carbonate aggregates. In the Lower Eagle Ford, such aggregates are thin and 10 to 100 μm in length. In the Upper Eagle Ford, aggregates are longer and they are more widely distributed compared to the Lower Eagle Ford (Figure 34 and Figure 35). Such carbonate aggregates are common in Upper Cretaceous chalk formations worldwide (Hattin, 1981; Pollastro, 2009). Macquaker et. al. (2010) suggests that generally two types of pellets including biomineral-rich and clay-rich pellets are described. Biomineral-rich pellets consist of phytoplankton, which are a widespread primary producer of organic matter during Cretaceous (Tissot and Welte, 1984), either coccoliths or recrystallized and less porous remains of these (Figure 36). The less porous pellets, which have different texture, can be interpreted as the product of other phytoplankton. Their size and distribution are variable in Upper and Lower Eagle Ford (Figure 34 and Figure 35).

Textural heterogeneity within Eagle Ford mudrocks is strongly influenced by the presence of pellets (Figure 36). If pellets are preferentially oriented, they are mostly elongated in the plane of bedding and they may show pronounced compactional bending around rigid particles (Figure 34) with preservation of shelter porosity beneath. Coarse-grained framework, which is dominantly composed of foraminifers, also contributes to textural heterogeneity. If grains are in contact, they can create shelter pores and preserve the uncompacted lens-shape of carbonate aggregates and also intergranular porosity, open or organic-matter filled, within the carbonate aggregates (Figure 39). This coarse-grained framework can affect textural variations related to bioturbation and lamination (Figure 37 and Figure 38). Coccolith plates and pellets are widely dispersed in bioturbated samples. Also, the presence of large rigid grains (larger-diameter foraminifers) can disrupt horizontally aligned fabric (Figure 40). By analogy to the study of Day-Stirrat (2010) dominant elongate grain types in the Eagle Ford, including carbonate aggregates (Figure 40), brittle biosiliceous grains, ductile clay minerals, and organic matter, are aligned conformable or unconformably to the bedding depending on the presence of foraminifers due to the effect of vertical stress.

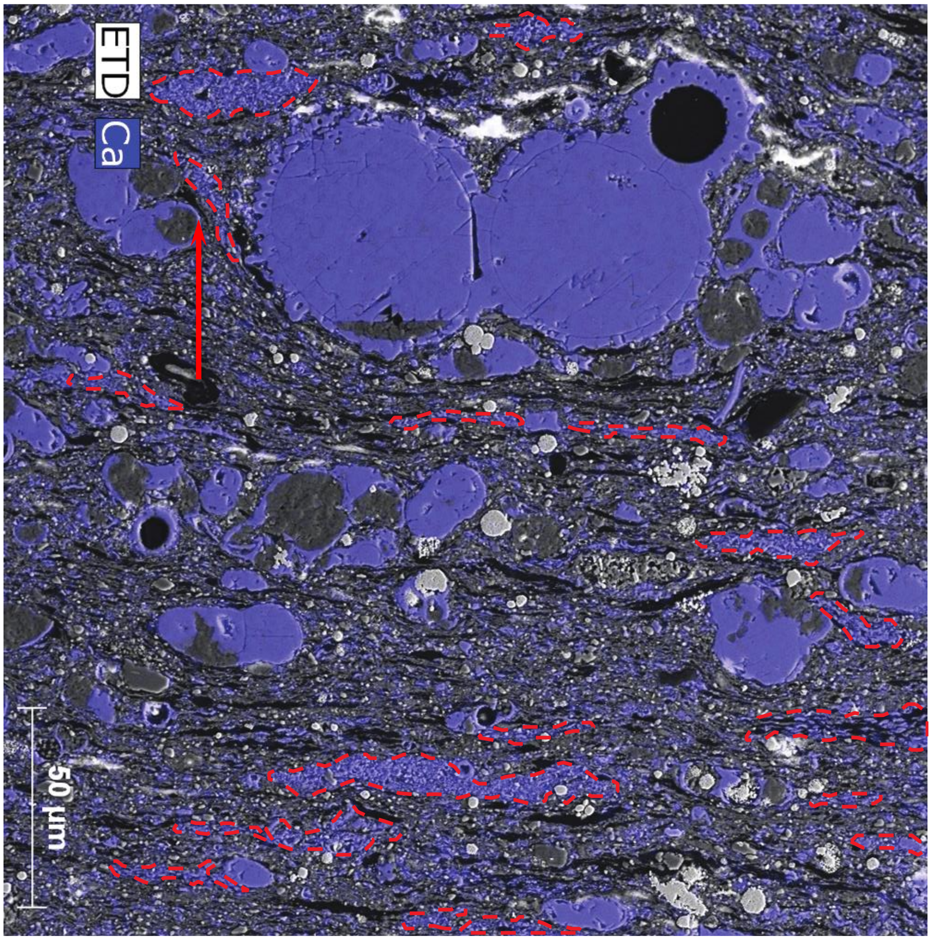

Figure 34: Carbonate aggregates in Lower Eagle Ford, shown in the EDS X-ray map of the low-maturity outcrop sample 1 (151.88-151.85m). The one shown with the red arrow is bent around the larger-diameter foraminifer.

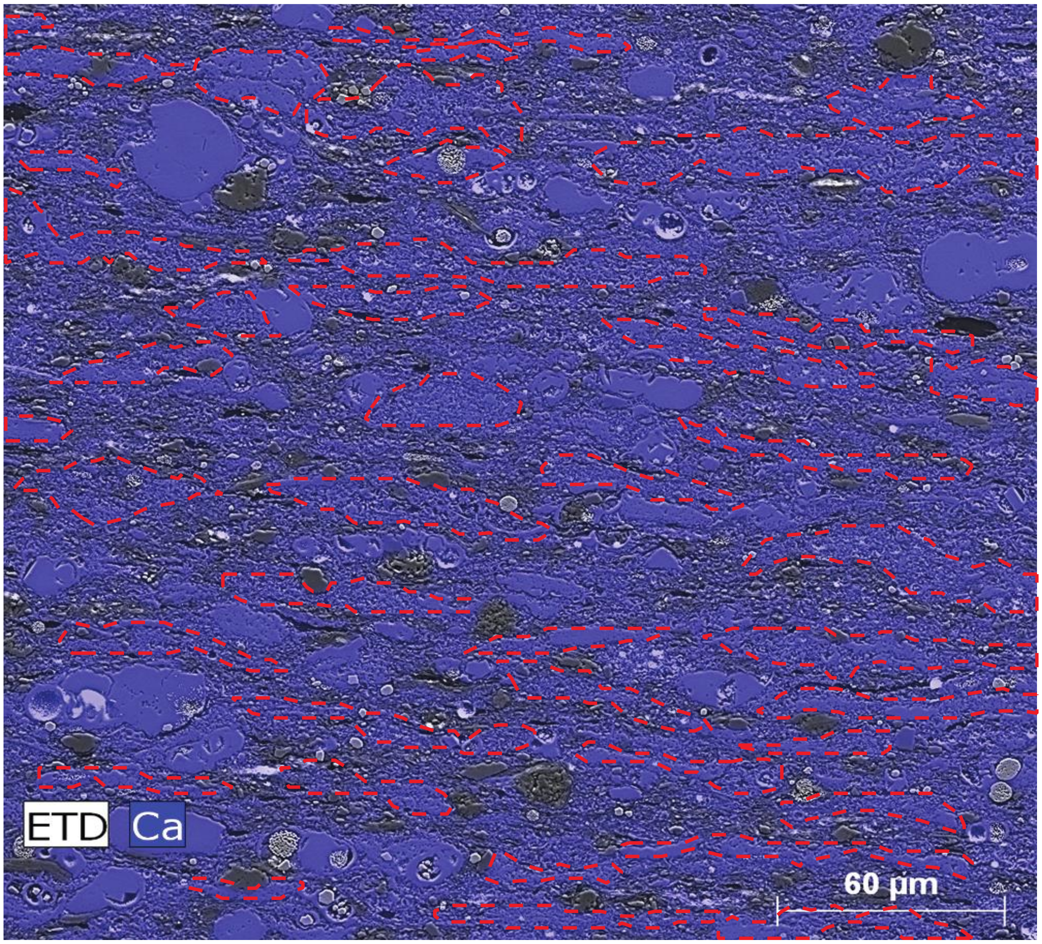

Figure 35: Carbonate aggregates in Upper Eagle Ford, shown in the EDS X-ray map of the low-maturity outcrop sample 23 (56.63-56.6m).

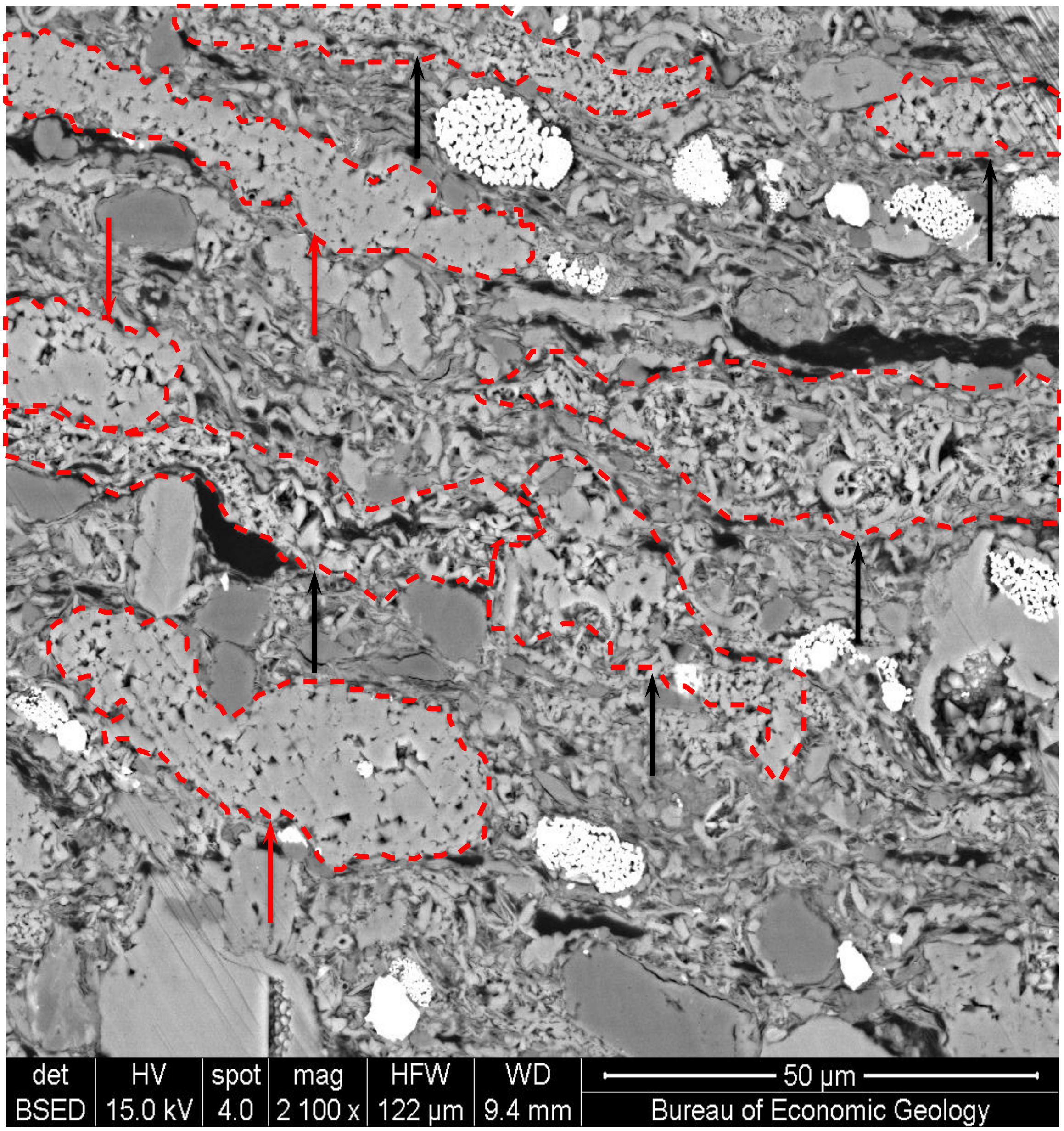

Figure 36: Heterogeneity in carbonate aggregates including loosely packed pellets (coccolith fragments can still be discriminated) (black arrow) and recrystallized pellets (euhedral calcite crytals can be seen) (red arrow) is shown in the BSED image of low-maturity outcrop Well 1 sample 23 (56.63-56.6m). Porosity decline can be observed in the recrystallized pellets. Note that possible explanation to this textural heterogeneity of pellets is formation by different organisms. (Image is taken by Max Pommer, 2013)

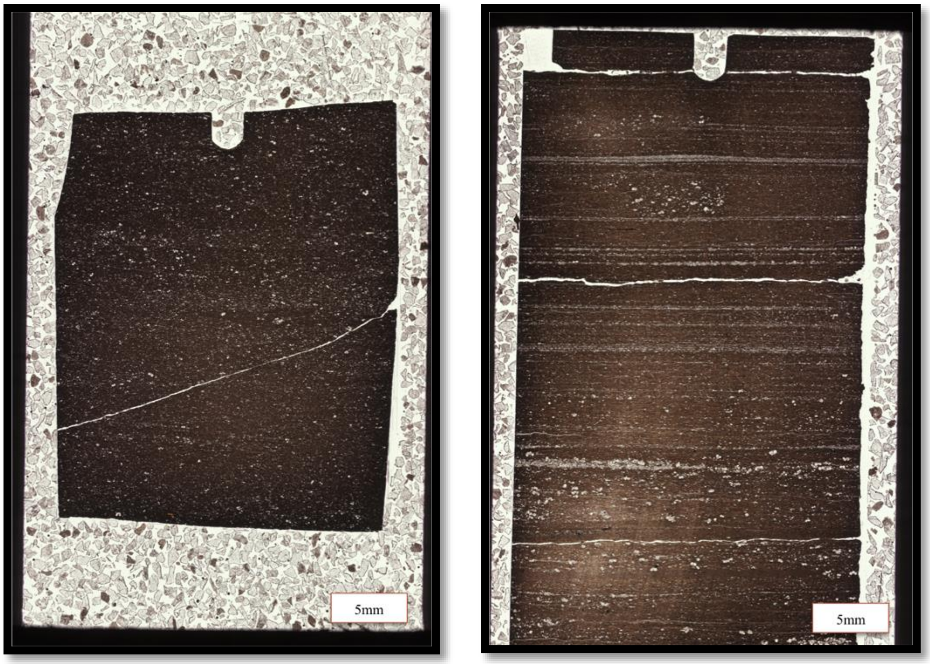

Figure 37: Scanned images of Well 1 sample 14 (on the left-bioturbated) and sample 16 (on the right-laminated) showing textural differences at the sample scale.

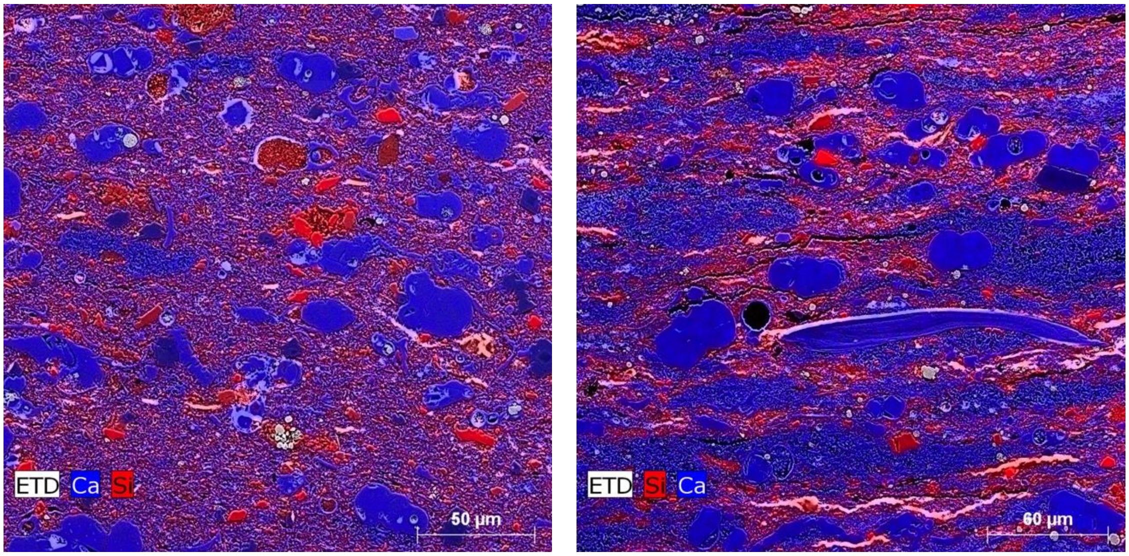

Figure 38: X-ray maps of Well 1 sample 14 (on the left, bioturbated) and sample 16 (on the right, laminated) showing textural differences at the sample scale.

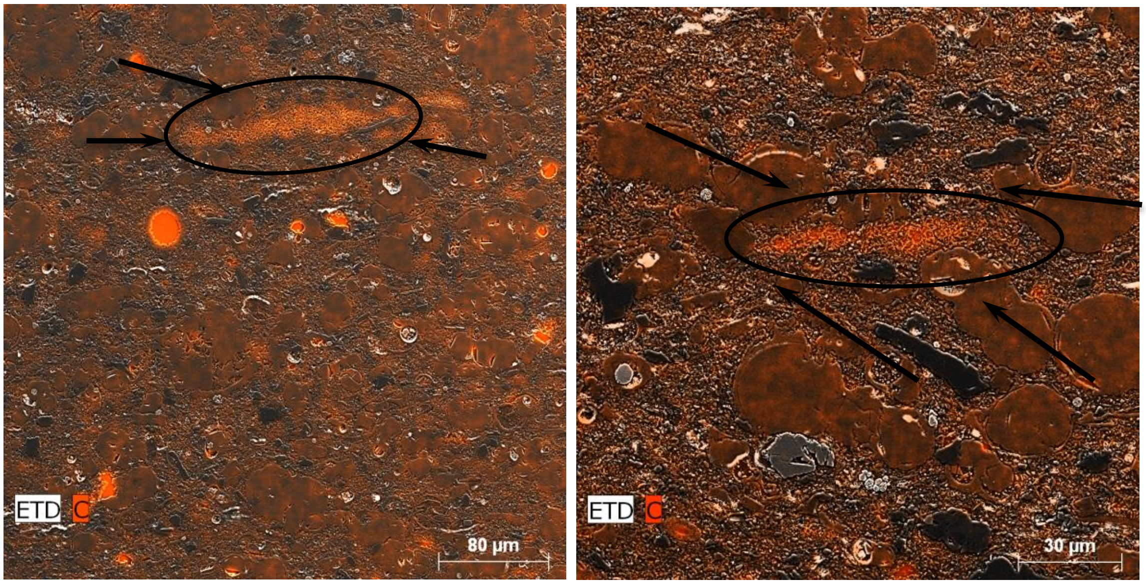

Figure 39: Preservation of shelter porosity within the carbonate aggregates between the silt-sized foraminifer grains are shown in the EDS X-ray maps of the (a) Well 1 sample 21 (500x machine magnification) (b) Well 1 sample 14 (1000x machine magnification). Note that lens shapes of carbonate aggregates are not preserved except for the one sheltered between the silt-sized foraminifers.

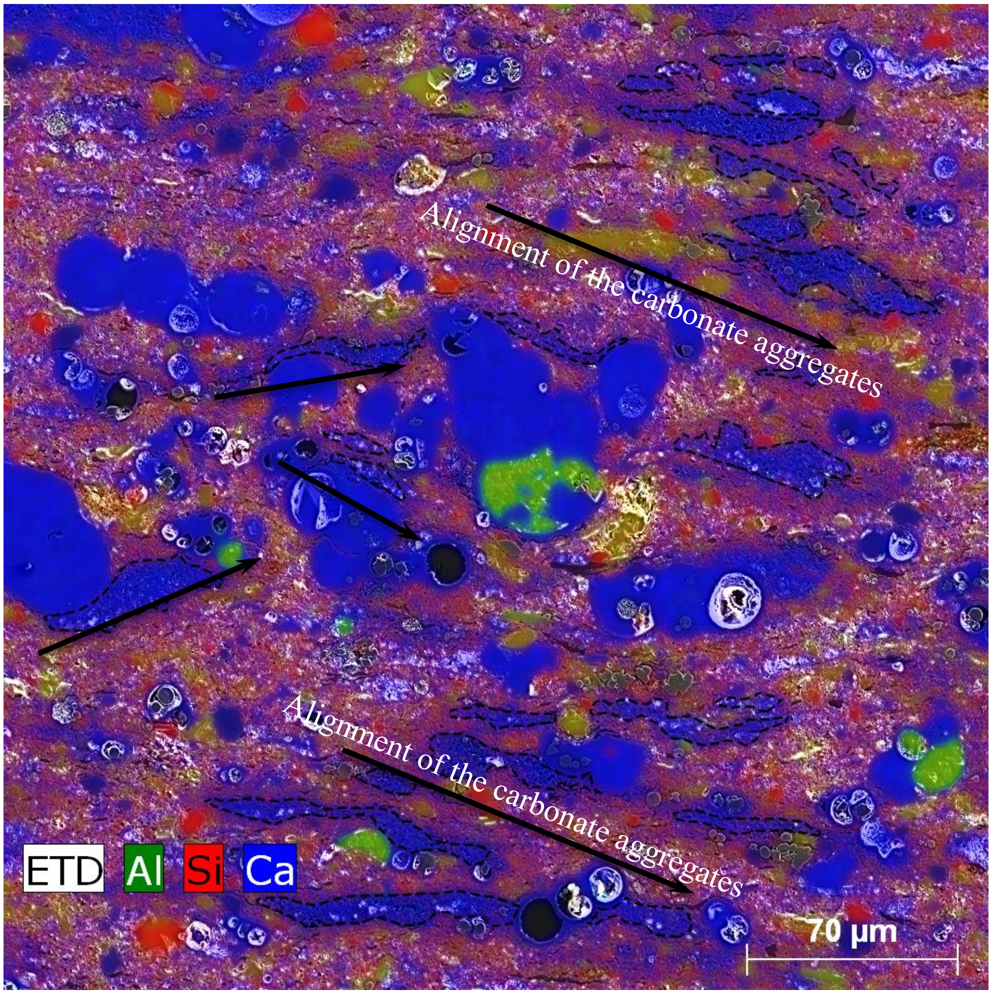

Figure 40: Alignment disruption of the fabric composed of carbonate aggregates by the presence of the larger-diameter foraminifers is shown in the EDS X-ray map of the low-maturity outcrop Well 1 sample 15. Note that carbonate aggregates show more compactional alignment where they surrounded by clay-size matrix compared to ones preserved between the larger-diameter foraminifers.

Phosphatic Intraclasts

Phosphatic intraclasts are non-fossiliferous microcrystalline phosphate grains, which are noted in other mudrocks (Papazis, 2005), and are not common in the Eagle Ford. However, some samples have local intervals of 5-10mm thickness of these particles

(Figure 41). These phosphatic intraclasts are discriminated from fossiliferous phosphate grains (bones and teeth) by amorphous shape (bones and teeth has more discrete shape and naturally occurring pores) and some detrital grain content. Phosphatic intraclasts are identified in all maturity levels; however their abundances are different. In Well 3 and 4, some intervals have phosphatic intraclasts in relatively large amounts, whereas other samples noted as phosphatic intraclast-bearing have this kind of intrabasinal particle in minor amounts (Table 6, Table 7, Table 8, and Table 9). This type of coarse grain accumulation has been interpreted as a lag layer related to a phosphate-cemented hardground (Papazis, 2005). In this interval, broken inoceramid plates, kaolinite-filled pelagic foraminifers, and also benthic foraminifers, occur in the grain assemblage with the phosphatic intraclasts (Figure 41 and Figure 42). Phosphatic intraclast type grains are mostly observed in the high-maturity well samples (Figure 44) and rarely in the low-maturity well samples (Figure 43).

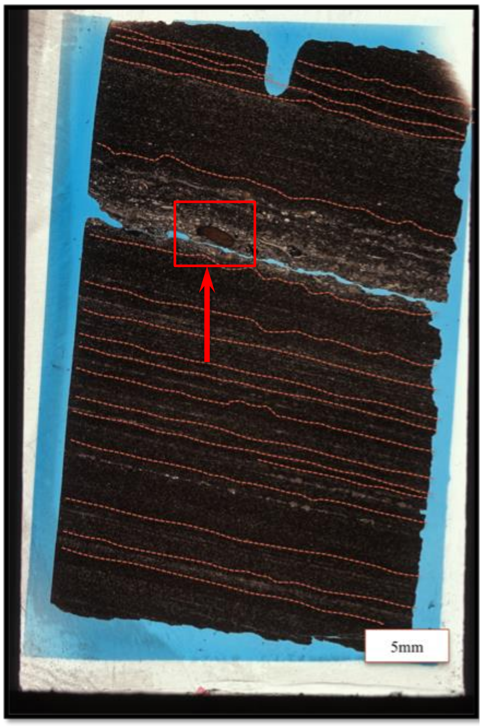

Figure 41: Phosphatic intraclast-bearing fossil lag layer is shown in the scanned image of the high-maturity Well 4 sample (2809.49m). Note that possible coprolite shown in the Figure 42 is indicated by red rectangle and arrow.

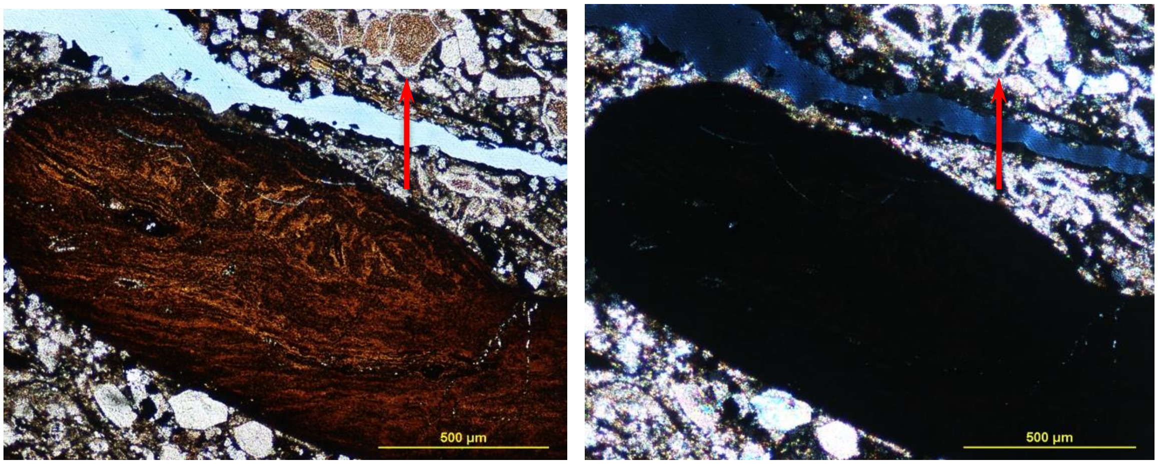

Figure 42: Phosphatic intraclast, a possible coprolite, shown in transmitted (a) plane-polarized (b) cross-polarized (black due to the isotropic property) light image of the high-maturity Well 4 sample (2809.49m) Red arrow indicates foraminifers.

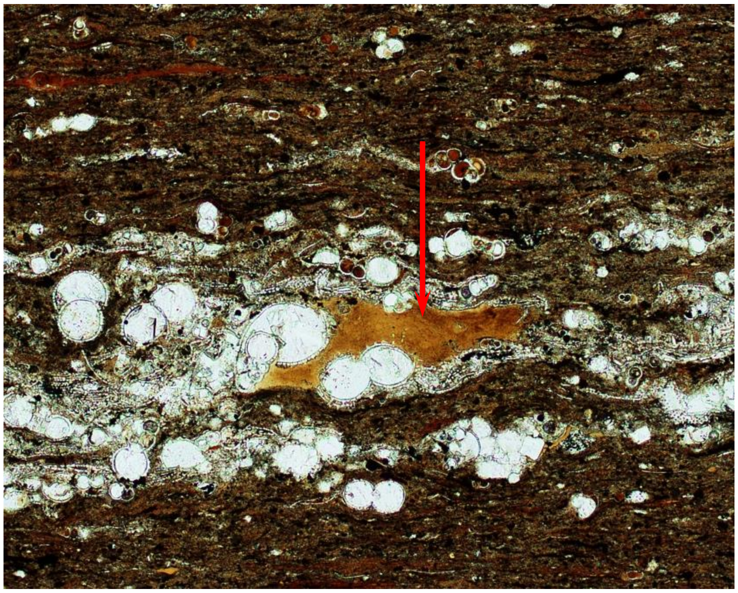

Figure 43: Compacted phosphatic intraclast (brown) deformed between rigid foraminifer tests is shown in transmitted plane-polarized light image of the low-maturity outcrop Well 1 sample 4 (139.88-139.85m).

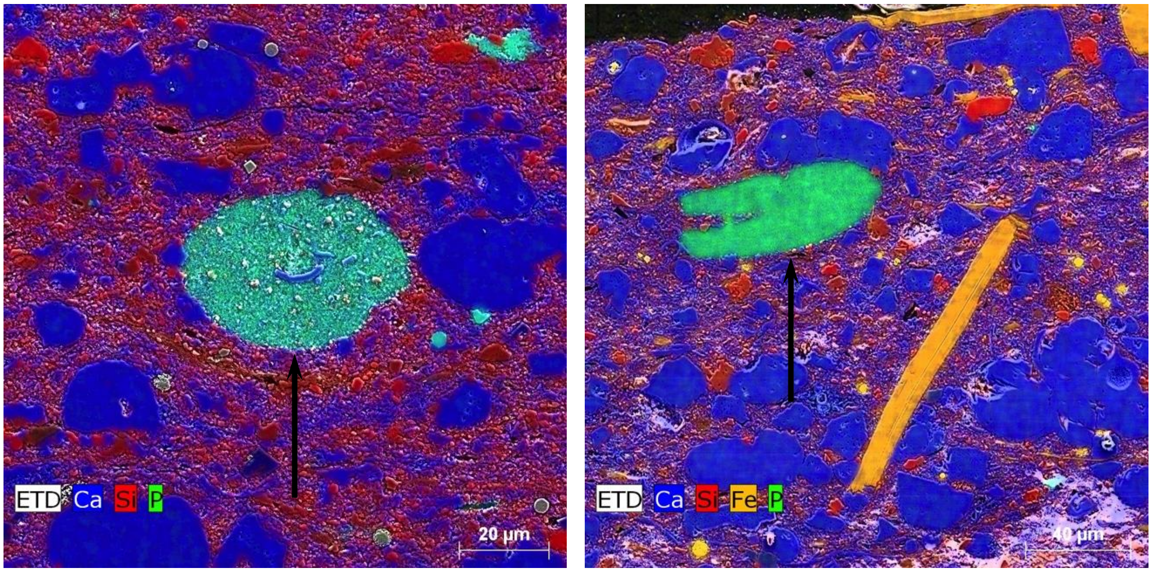

Figure 44: Phosphate intraclasts, possible coprolites, are shown in the EDS X-ray maps of (a) the high-maturity Well 3 sample 1-61 (2533.88m) (b) the low-maturity outcrop Well 1 sample 19 (81.28m).

Organic Matter

Intrabasinal organic matter, which is another type of detrital organic matter in the Eagle Ford, occurs as organomineralic aggregates (OMA) (Figure 45), recognizable algal spores (Figure 46), and dispersed, amorphous organic matter. One source of detrital organic matter that is widespread in mudrocks is marine snow which is described by Bennett et. al. (1991) as a biosediment aggregate. These aggregates, which are composed of both extrabasinal transported detrital particles and intrabasinal organic masses are important components of organic-rich sediment (Macquaker et. al., 2010; Slatt and O' Brien, 2013). Algal spores are prone to compaction and they are mostly observed as collapsed instead of having discrete shape, somewhat in contrast with the extrabasinal organic matter (woody fragments). Amorphous organic matter is generally observed without clear outlines, distinct shape and identifiable structure (Tissot and Welte, 1984) (Figure 47). Amorphous kerogen is defined as weakly or cryptically structured kerogen either originated from marine or terrigeneous (Teerman et. al., 1995; Milliken et. al., 2013).

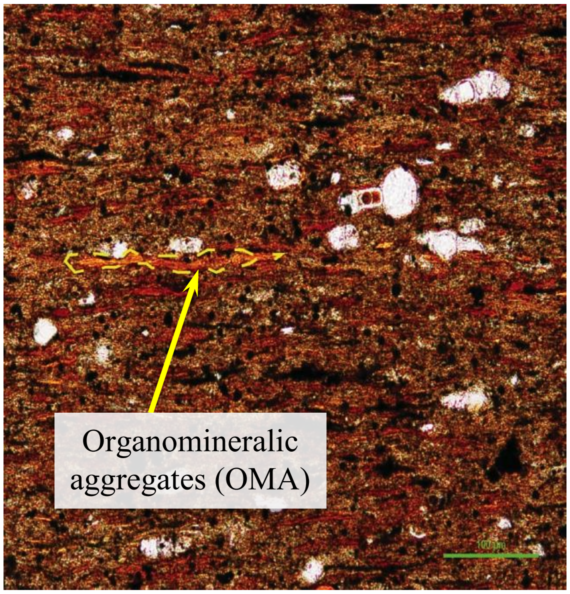

Figure 45: Organomineralic aggregates (OMA), which are ancient marine snow (Macquaker et. al., 2010), are shown in transmitted plane-polarized light image of the low-maturity outcrop Well 1 sample 1.

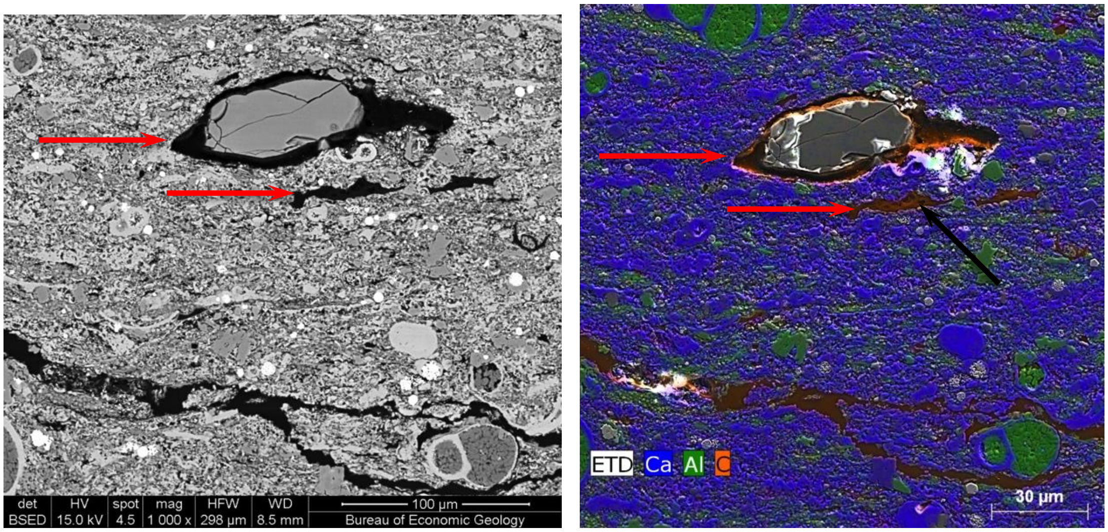

Figure 46: Algal spore type intrabasinal organic matter (lower red arrow) is shown in the (a) BSED image (b) EDS X-ray map of the medium-maturity Well 2 sample CH5 (963.78m). Upper red arrow show intraparticle pore within the organic particle, possibly algal spore. Note that most likely diagenetic micropores are identified within the organic matter (black arrow).

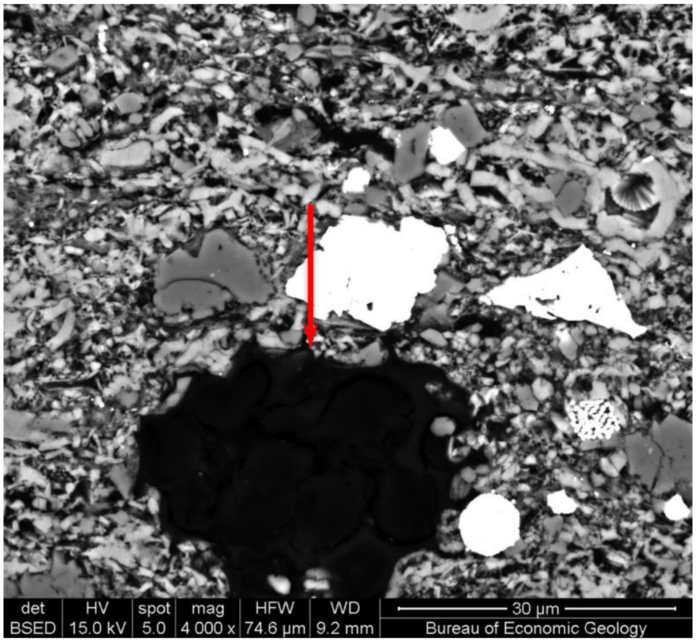

Figure 47: Particulate type organic matter is shown in the backscattered image of the medium maturity Well 2 sample CH5 (963.8m). Note that due to lack of distinct shape and structure it can be interpreted as amorphous type organic matter but there is not enough evidence.

Table 6: Intrabasinal grain assemblages showing major categories of calcareous, non-calcareous fossils and phosphatic intraclasts of low-maturity outcrop well samples

Sample NO	Depth (m)	Calcareous Fossils							Non-calcareous Fossils		Phosphatic Intraclasts
		Pelagic Forams	Bethic Forams	Inoceramids	Oysters	Echinoderms	Thin-walled mollusks	Calcispheres	Bones&Teeth	Siliceous	
23	56.63-56.6	🟩		🟩		🟩			🟩	🟩	
22	57.11-57.08	🟩		🟩		🟩			🟩		
21	69.88-69.85	🟩		🟩	🟩				🟩		
20	79.68-79.65	🟩		🟩	🟩				🟩		
19	81.28-81.25	🟩		🟩					🟩		🟩
18	88.93-88.8	🟩		🟩					🟩	🟩	
17	92.84-92.81	🟩					🟩		🟩		
16	98.11-98.08	🟩		🟩					🟩		
15	99.85-99.82	🟩		🟩					🟩		🟩
14	104.86-104.83	🟩		🟩					🟩		
13	106.47-106.44	🟩					🟩		🟩		
12	110.04-110.01	🟩	🟩						🟩		
11	115.48-115.45	🟩							🟩		
10	122.94-122.91	🟩		🟩			🟩		🟩		
8	128.91-128.88	🟩	🟩	🟩					🟩		
7	133.71-133.68	🟩		🟩		🟩			🟩		
4	139.88-139.85	🟩			🟩		🟩		🟩		🟩
2	149.52-149.49	🟩	🟩	🟩		🟩		🟩	🟩	🟩	
1	151.88-151.85	🟩					🟩		🟩		

Table 7: Intrabasinal grain assemblage showing major categories of calcareous, non-calcareous fossils and phosphatic intraclasts of medium-maturity well samples

Sample NO	Depth (m)	Depth (ft)	Calcareous Fossils							Non-calcareous Fossils		Phosphatic Intraclasts
			Pelagic Forams	Bethic Forams	Inoceramids	Oysters	Echinoderms	Thin-walled mollusks	Calcispheres	Bones&Teeth	Siliceous	
CH1	911.3	2989.8	🟩		🟩		🟩					
CH2	915.8	3004.6	🟩		🟩					🟩		
CH3	950.2	3117.6	🟩		🟩					🟩		
CH4	953.2	3127.4	🟩		🟩			🟩				
CH5	963.8	3162.0	🟩		🟩					🟩	🟩	🟩
CH6	969.9	3182.3	🟩							🟩		🟩
CH7	973.3	3193.1	🟩		🟩	🟩						

Table 8: Intrabasinal grain assemblage showing rough categories of calcareous, non-calcareous fossils and phosphatic intraclasts of high-maturity well samples

Sample NO	Depth (m)	Depth (ft)	Calcareous Fossils							Non-calcareous Fossils		Phosphatic Intraclasts
			Pelagic Forams	Bethic Forams	Inoceramids	Oysters	Echinoderms	Thin-walled mollusks	Calcispheres	Bones&Teeth	Siliceous	
EF31-31	2524.8	8283.4	🟩		🟩							
EF3 1-61	2533.9	8313.3	🟩		🟩	🟩		🟩				🟩
EF3 1-66	2535.5	8318.6	🟩		🟩	🟩	🟩	🟩	🟩		🟩	
EF3 1-136	2556.7	8388.0	🟩				🟩			🟩		🟩

Table 9: Intrabasinal grain assemblage showing major categories of calcareous, non-calcareous fossils and phosphatic intraclasts of high-maturity well samples

Sample NO	Depth (m)	Depth (ft)	Calcareous Fossils							Non-calcareous Fossils		Phosphatic Intraclasts
			Pelagic Forams	Bethic Forams	Inoceramids	Oysters	Echinoderms	Thin-walled mollusks	Calcispheres	Bones&Teeth	Siliceous	
EF4 1-5	2775.0	9104.5	🟩					🟩			🟩	🟩
EF4 1-10	2776.6	9109.7	🟩		🟩	🟩		🟩	🟩		🟩	
EF4 1-25	2781.1	9124.4	🟩		🟩			🟩	🟩			🟩
EF4 1-35	2784.1	9134.2	🟩						🟩		🟩	
EF4	2787.7	9146.0	🟩					🟩				🟩
EF4	2790.7	9156.0	🟩		🟩							
EF4 1-75	2796.2	9174.0	🟩								🟩	
EF4 1-80	2797.9	9179.6	🟩						🟩		🟩	🟩
EF4 1-90	2800.9	9189.3	🟩		🟩							🟩
EF4 1-100	2804.0	9199.5	🟩		🟩		🟩		🟩		🟩	
EF4 1-123	2811.1	9222.7	🟩									🟩

CLASSIFICATION OF EAGLE FORD

Observations of the grain assemblage in the Eagle Ford are used here as a test case for a classification scheme that uses by the end-members of terrigeneous and volcanic grains, biosiliceous grains, and calcareous allochems (Figure 9).

Here the quantitative results based on the point-count of the detrital grains (extrabasinal and intrabasinal grains) are reported. Point counting is applied to all samples (Table 10) (Table 11), (Table 12) and (Table 13) (except for sample 2 from low maturity Well 1 and 1-10, 1-35 and 1-80 from high maturity Well 4). Relative percentages of detrital grains acquired from the point count results are plotted to the variety in different samples and different maturity levels (Figure 48). Calcareous allochems are higher in percentage in the deeper samples and some UEF section of the shallow samples. This variation is directly associated with the decreasing clay and mica percentages.

The samples plot along the left edge of the triangle along the join between the terrigeneous and volcanic grains and calcareous allochems. By this classification scheme, samples plot as marls, argillaceous marls, and calcareous tarls (Figure 49, Figure 50, Figure 51 and Figure 52) (Table 10, Table 11, Table 12, and Table 13). The same end members, which are used to give, are clan names to the mudrocks are also used as compositional modifiers (Figure 9). Only the sample at the lowermost part of Well 1 falls into the region of calcareous tarls (Figure 49). Other Lower Eagle Ford samples of Well 1 and some Upper Eagle Ford samples of Well 1 plot as argillaceous marls (Figure 49).

Other Upper Eagle Ford samples of Well 1, medium-maturity and high-maturity samples of the Eagle Ford are classified as marls.

Table 10: Point count results and class names of low-maturity outcrop well samples

Sample NO	Depth (m)	Class Name	Quartz%	Feldspars%	Clay+Mica%	Lithics%	Calcareous Allochems%	Terrigeneous and Volcanic Grains%
1	151.88	calcareous tarl	2	0	51.33	0	46.67	53.33
4	139.88	argillaceous marl	0.67	0	42.67	0	56.67	43.34
7	133.71	argillaceous marl	2	3.33	31.67	4	59	41
8	128.91	argillaceous marl	1	2.67	36	4.33	56	44
10	122.94	argillaceous marl	0.33	1	35	1	62.67	37.33
11	115.48	argillaceous marl	1.67	1.33	35.67	1.33	60	40
12	110.04	argillaceous marl	4.33	1.33	28	6	60.33	39.66
13	106.47	argillaceous marl	3.67	6.67	22.67	6	61	39.01
14	104.86	argillaceous marl	0.33	3.67	33.33	1	61.67	38.33
15	99.85	marl	2.67	5.33	19.67	1.67	70.67	29.34
16	98.11	marl	2	2.67	17.67	2.33	75.33	24.67
17	92.84	marl	1	1	21.67	0.67	75.67	24.34
18	88.93	marl	1	1.33	11.67	5	81	19
19	81.28	marl	3.84	6	16.5	1.67	72	28
20	79.68	marl	0.67	4	15	2	78.33	21.67
21	69.88	marl	2.33	4.67	15	3.67	74.33	25.67
22	57.11	argillaceous marl	2.33	7.33	18.33	9.67	62.33	37.66
23	56.63	marl	0.67	6.33	16.33	2	74.67	25.33

Table 11: Point count results and class names of medium-maturity well samples

Sample NO	Depth (m)	Depth (ft)	Class Name	Quartz%	Feldspars%	Clay+Mica%	Lithics%	Calcareous Allochems%	Terrigeneous and Volcanic Grains%
CH1	911.28	2989.75	marl	0.67	1.67	14	1.67	82	18.01
CH2	915.79	3004.55	marl	1.67	6.33	12.67	3	76.33	23.67
CH3	950.24	3117.6	marl	1.33	5	15.67	1.33	76.67	23.33
CH4	953.22	3127.35	marl	0.33	6.67	10	0.33	82.67	17.33
CH5	963.78	3162	marl	1	4.33	16	1.33	77.33	22.66
CH6	969.95	3182.25	marl	0.67	4.67	14.33	0.33	80	20
CH7	973.26	3193.1	marl	1	3.33	11.33	2.67	81.67	18.33

Table 12: Point count results and class names of the high-maturity well samples

Sample NO	Depth (ft)	Depth (m)	Class Name	Quartz %	Feldspar %	Clay+Mica%	Lithics %	Calcareous Allochems %	Terrigeneous and Volcanic Grains %
EF3 1-31	8283	2524.66	marl	2.33	6.67	13	0	78	22
EF3 1-61	8313.25	2533.88	marl	3.67	7.33	12.67	1.33	75	25
EF3 1-66	8318	2535.33	marl	1.67	4	8.33	1.67	84.33	15.67
EF3 1-136	8388	2556.66	marl	1.33	0.67	16.33	0	81.67	18.33

Table 13: Point count results and class names of the high-maturity well samples

Sample NO	Depth (ft)	Depth (m)	Class Name	Quartz%	Feldspars%	Clay+Mica%	Lithics%	Calcareous Allochems%	Terrigeneous and Volcanic Grains%
EF4 1-5	9104.45	2775.04	marl	1	2.67	24	0	72.33	27.67
EF4 1-25	9124.35	2781.1	marl	2.33	1.67	23.67	0.33	72	28
EF4	9146	2787.7	marl	3.33	4	20	1	71.67	28.33
EF4	9156	2790.75	marl	1.67	11	15.87	0.67	71	29.21
EF4 1-75	9174	2796.24	marl	1.67	2	23.33	0	73	27
EF4 1-90	9189.3	2800.9	marl	2.67	2.33	17.33	0	77.67	22.33
EF4 1-100	9199.45	2803.99	marl	5	1	12.33	1.67	80	20
EF4 1-123	9222.65	2811.06	marl	6.33	1	16	1	75.67	24.33

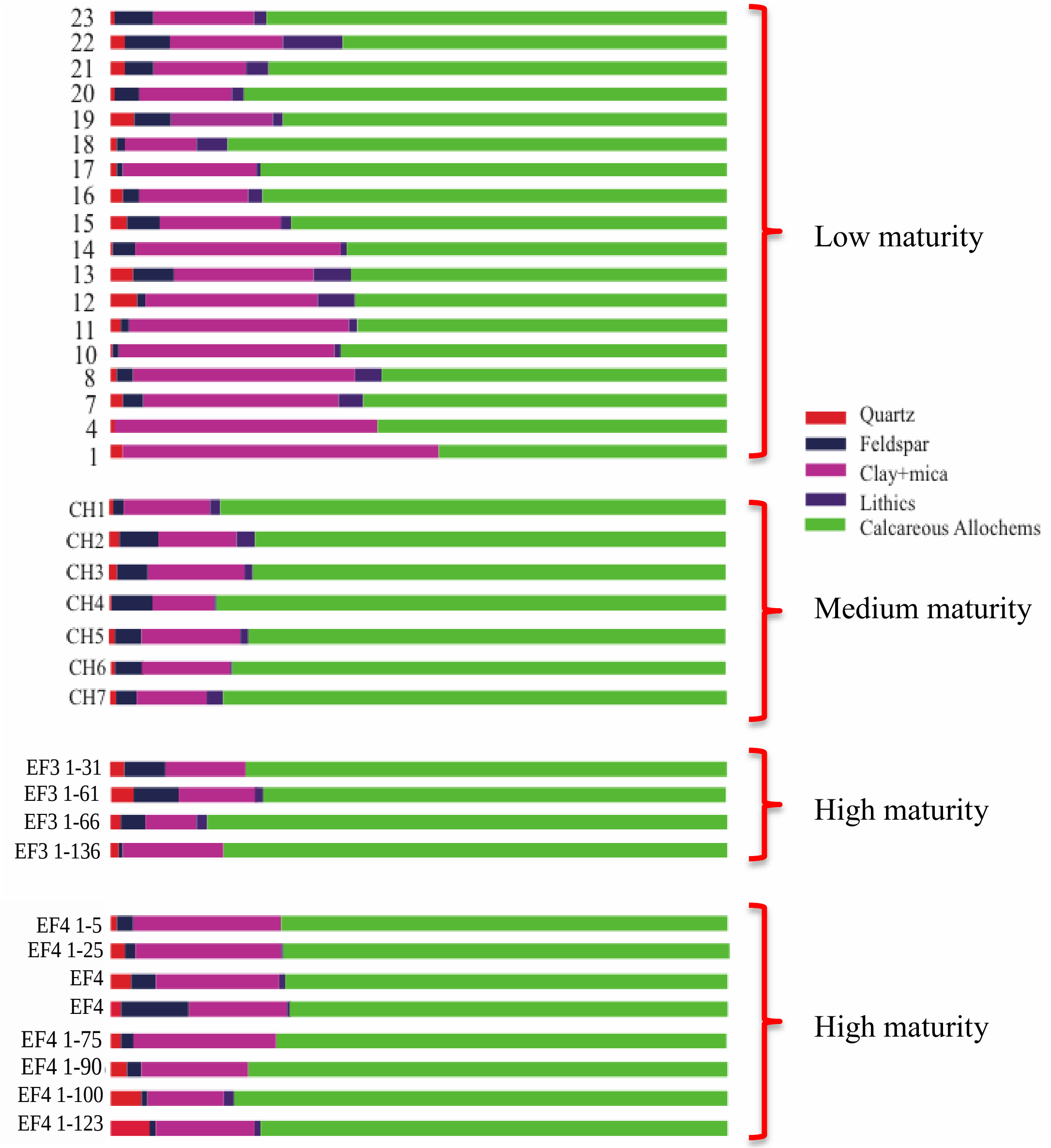

Figure 48: Relative percentages of detrital grains in different wells obtained from point counts. Note that same colors with the point counting categories (Figure 8) are used.

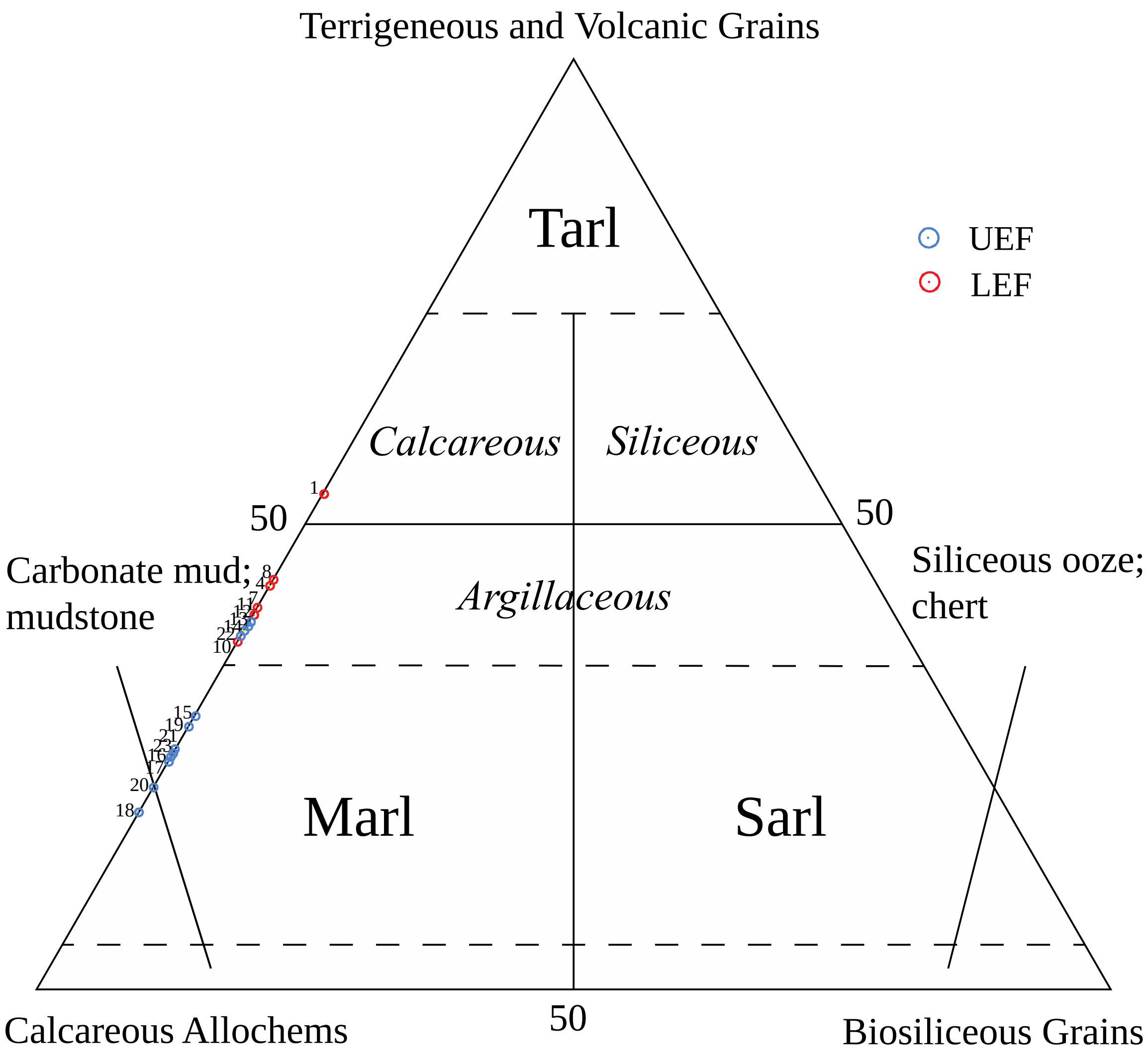

texture name: cement *modifier* grain *modifier* compositional *modifier* clan name
(-ooze, -stone)

Figure 49: Plotted samples of low-maturity outcrop well on the mudrock classification scheme. Red and blue represent samples from Lower Eagle Ford and Upper Eagle Ford, respectively.

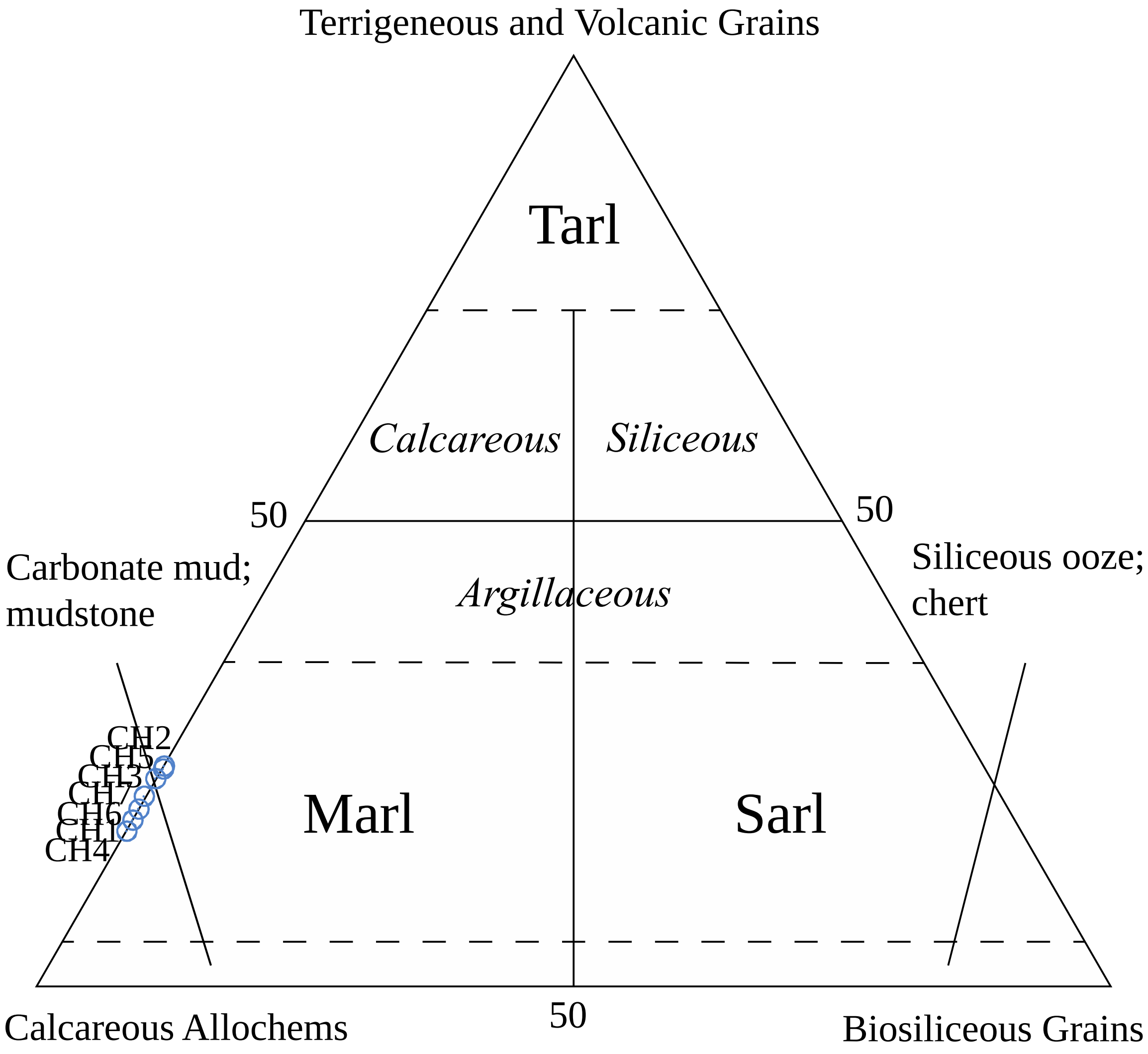

texture name: cement *modifier* grain *modifier* compositional *modifier* clan name (-ooze, -stone)

Figure 50: Plotted samples of medium-maturity well on the compositional mudrock classification. Note that UEF and LEF boundary is not known and the blue color does not correspond to UEF samples

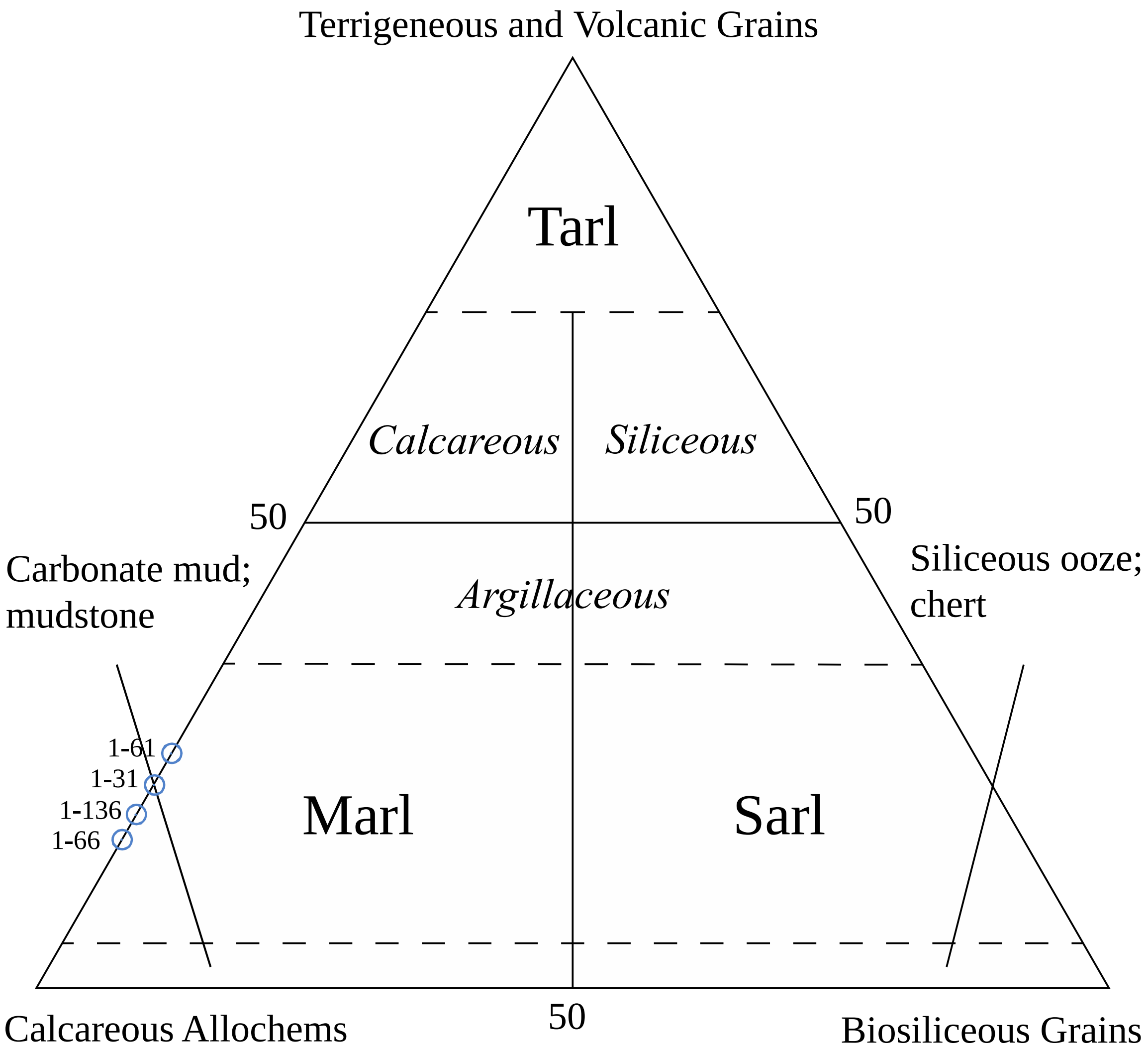

texture name: cement *modifier* grain *modifier* compositional *modifier* clan name (-ooze, -stone)

Figure 51: Plotted samples of high-maturity well samples on the mudrock classification scheme. Note that UEF and LEF boundary is not known and the blue color does not correspond to UEF samples

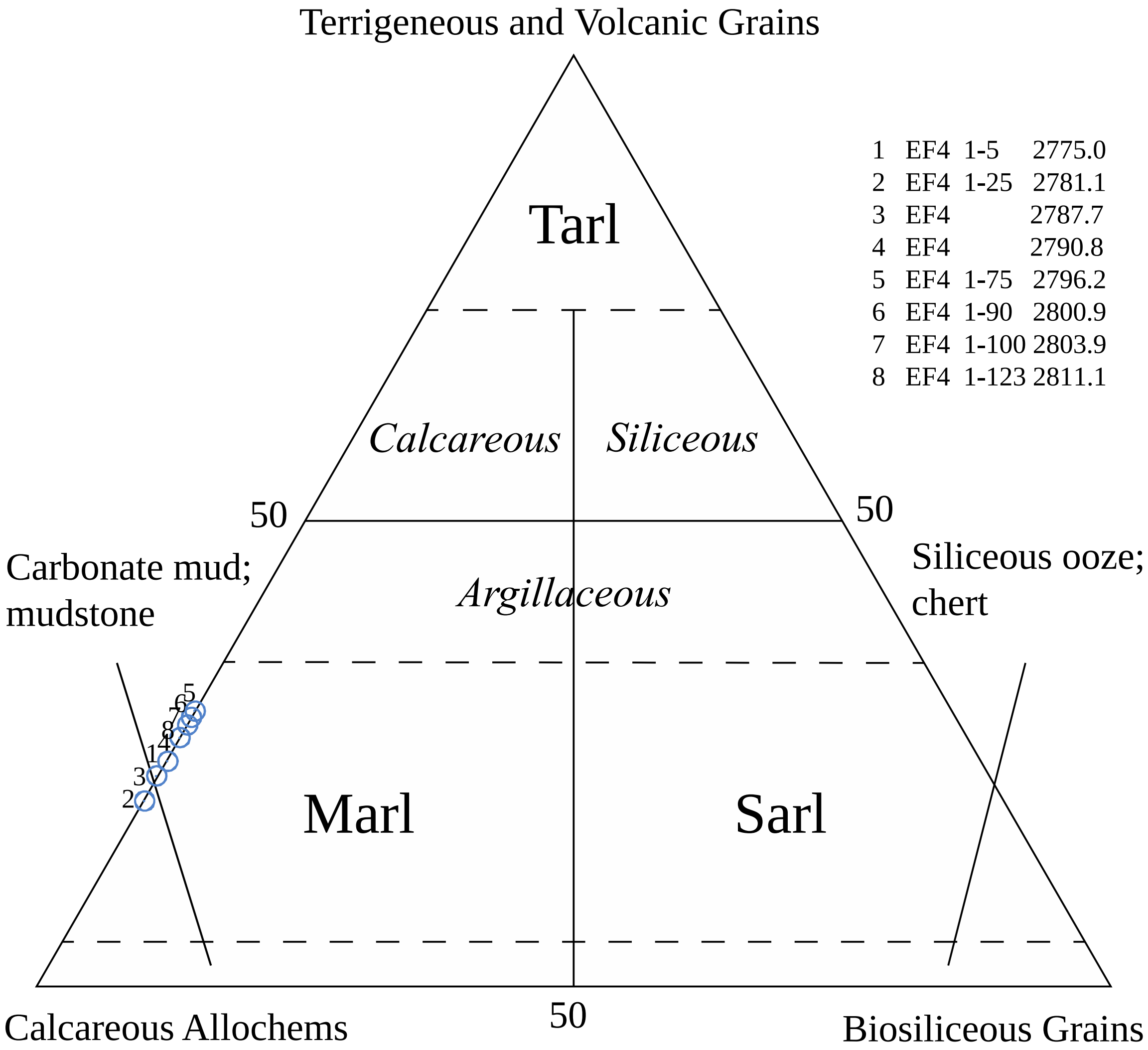

texture name: cement *modifier* grain *modifier* compositional *modifier* clan name (-ooze, -stone)

Figure 52: Plotted samples of high maturity well samples on the mudrock classification scheme. Note that UEF and LEF boundary is not known and the blue color does not correspond to UEF samples.

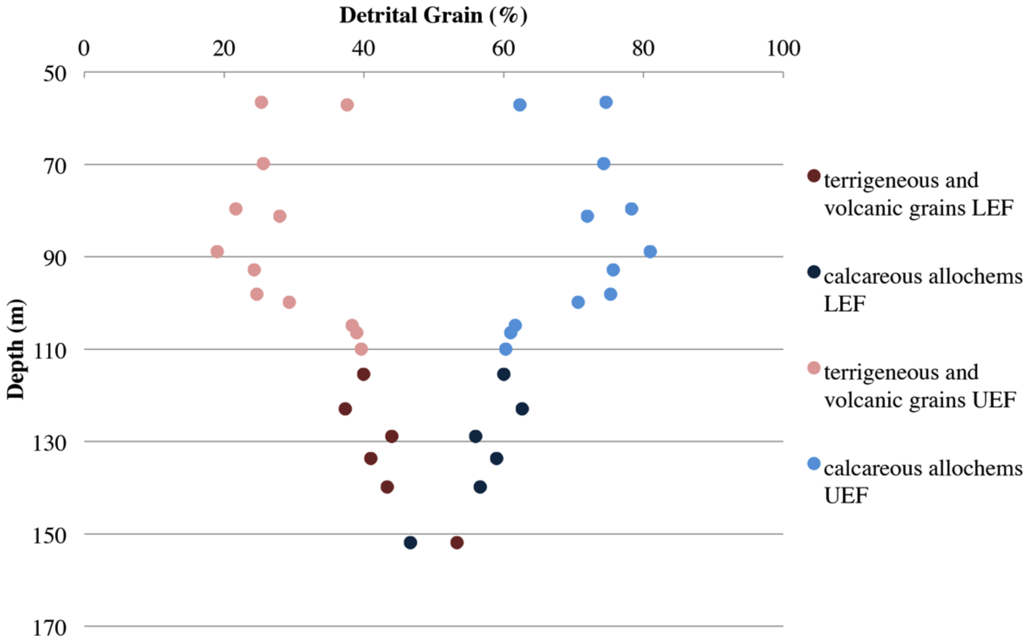

Figure 53: Compositional variation with depth in the low-maturity outcrop Well 1. Percentages of all grains total to 100%.

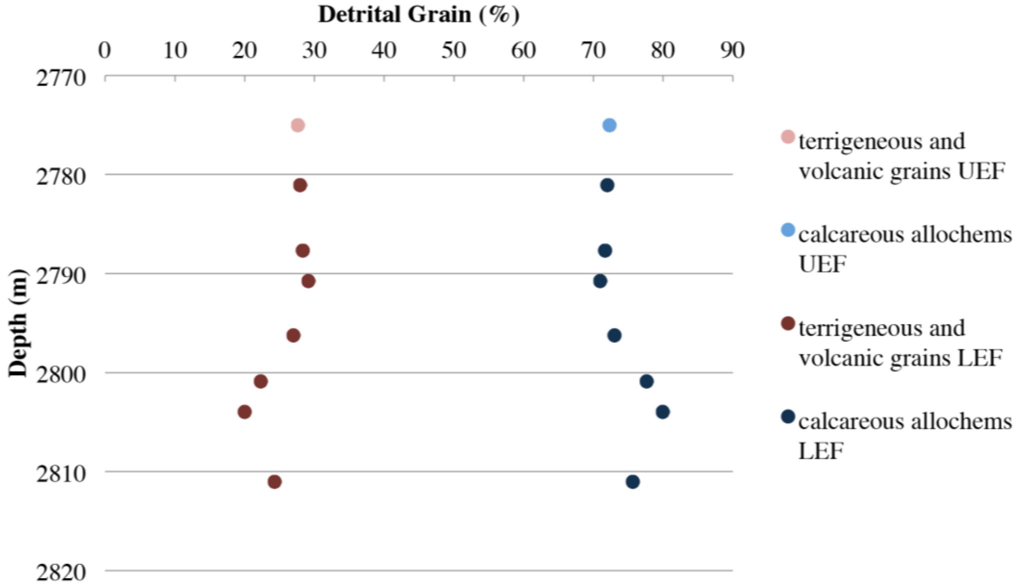

Figure 54: Compositional variation with depth in the high-maturity Well 4 samples. Percentages of all grains total to 100%.

Calcareous Tarls

Tarl is the term used here for the both consolidated and unconsolidated sediments, which have more than 50% terrigenenous and volcanic grains (by weight or volume). Calcareous tarls contain calcareous allochems in amounts greater than 25% (Figure 55). They can be considered as extrabasinal-dominated mudrocks and their enrichment in terrigeneous and volcanic grains can be related to terrigeneous influx. In Well 1, terrigeneous and volcanic grains increase with stratigraphic depth in the formation and vice versa in the Well 4 samples (Figure 53 and Figure 54). Where siliciclastic sediments dominate the detrital assemblage, calcareous allochems, dominated by pelleted coccolith-rich carbonate aggregates, become less common.

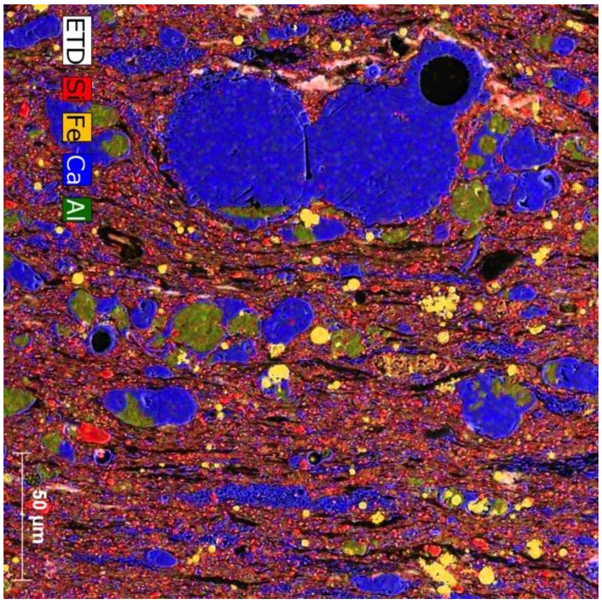

Figure 55: Representative EDS X-ray map image of the calcareous tarl from the low-maturity outcrop Well 1 sample 1. Note that abundance of terrigeneous and volcanic grains and relative scarcity of calcareous allochems.

Argillaceous Marl

Argillaceous marl has more than 50% calcareous allochems within the grain assemblage (Figure 56). If marl contains more than 25% terrigeneous and volcanic grains, which are dominated by argillaceous sediments in mudrocks, they are designated as argillaceous marl. The placement of the boundary between argillaceous marl and marl is placed here so as to discriminate samples that are visually different in this particular sample set of low-maturity outcrop Well 1. The boundary effectively separates all LEF samples of Well 1 and few UEF samples of Well 1 from the samples of the Upper Eagle Ford, which are also different in their OM content (Xun et. al, 2014).

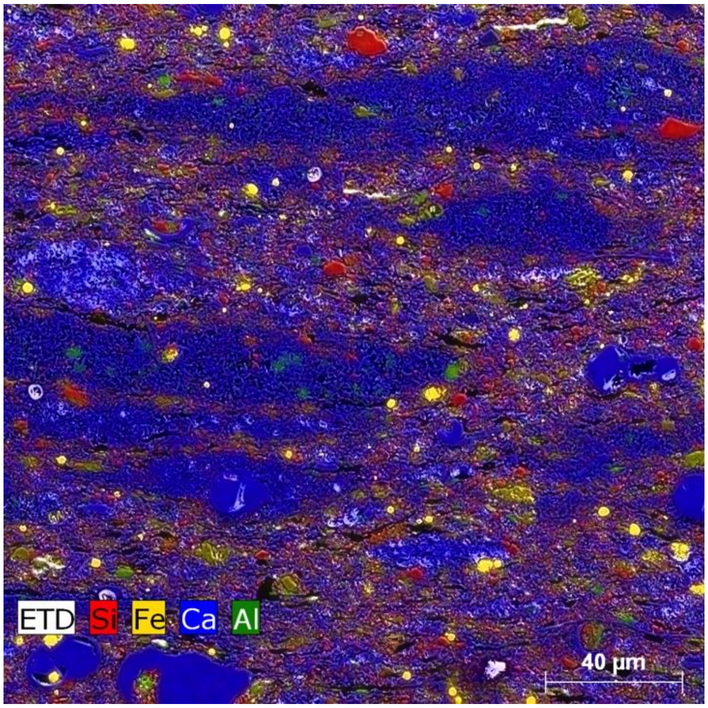

Figure 56: Representative EDS X-ray map of the argillaceous marl example from the low-maturity outcrop Well 1 sample 10 (122.94m).

Marl

In the study of Longman et. al. (1998), the classification on the basis of carbonate to shale spectrum defined by Pettijohn (1975) is modified. Sedimentary rocks are named as pure chalk to shale with the variable clay to carbonate percentages. Rocks having 95% to 100% carbonates are called as pure chalk and 65% to 35% carbonates are named as marl (Longman et. al., 1998) (Figure 58). Both of these classifications fail to recognize the importance of non-clay minerals in the mixing of extrabasinal and intrabasinal sediments. In the classification applied here the boundary between argillaceous marl and marl is set at 25% extrabasinal grains; This boundary between argillaceous marl and marl can be very close as 65% to 70% carbonate content used by Longman (1998) as the boundary between marly shale and marl. Point count results show that, majority of the samples are classified as marl but none of them are located in the "pure chalk" section of the classification triangle. Excepting only four samples, the samples of the Well 2, Well 3 and Well 4, and UEF section of the Well 1 are classified as marl (Figure 57).

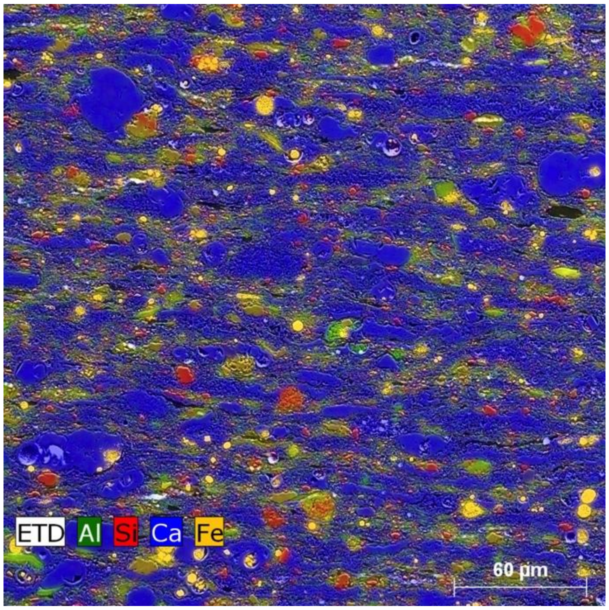

Figure 57: Representative EDS X-ray map of the marl example from low-maturity outcrop Well 1 sample 23 (56.63m)

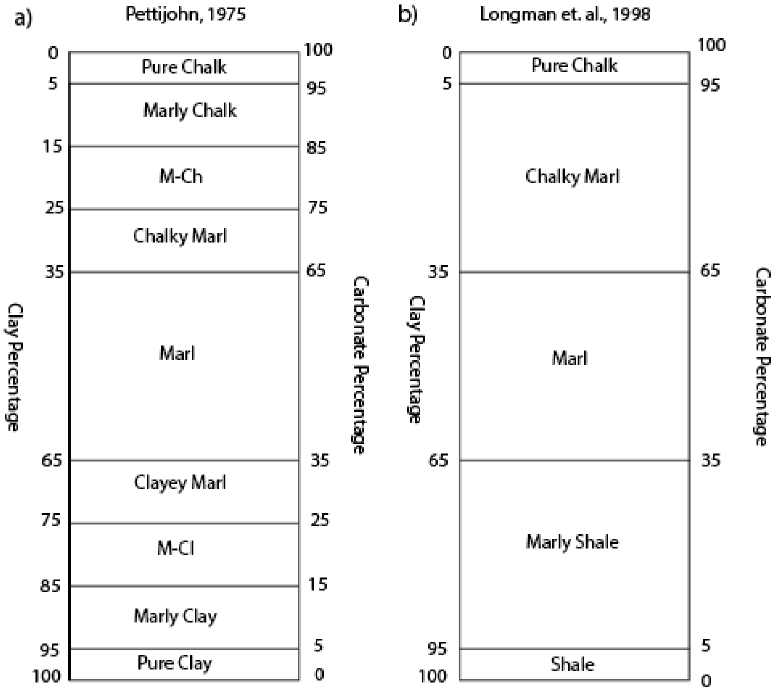

Figure 58: Carbonate to shale spectrum and different nomenclature defined in the study of (a) Pettijohn (1975) (b) Longman et. al. (1998).

Diagenetic Features

Diagenesis encompasses chemical and mechanical processes in the subsurface, following deposition and prior to the commencement of metamorphism or weathering (Muller, 1967; Bjorlykke, 1983; Milliken, 2003). Diagenesis includes the processes that transform unconsolidated sediments to hard rocks (compaction, cementation, dissolution, replacement, and fracturing) and is one of the most important parameters in the evolution of mechanical rock properties (Milliken, 2013). In the diagenesis of the Eagle Ford the main processes responsible for the mechanical rock behavior and other reservoir properties are compaction and cementation. Replacement, dissolution, and fracturing have minor effects on the evolution of mechanical behavior of the Eagle Ford. It is proposed that cementation has a pronounced impact on the sediment strength, brittleness, deformation, and porosity due to the binding effect on grain contacts (White et. al., 2011; Milliken, 2013). Due to the challenges related with the imaging techniques of very-fine grained material even using scanning electron microscopy, cementation in mudrocks is not understood well (Milliken and Day-Stirrat, 2013; Milliken, 2013).

MECHANICAL DIAGENESIS

Compaction is a mechanical process. It is the bulk volume reduction related to loss of pore volume by mechanical rearrangement of the solid rock components in response to overburden load in the subsurface. During compaction grains move closer and the intergranular space between the grains decreases, resulting in bulk volume reduction. The degree of compaction and porosity loss due to compaction is highly variable in mudrocks (Rieke and Chilingarian, 1974; Bjorlykke and Hoeg, 1997). Due to the constraints mostly related to the fine grain size of the dominant mudrock components, it is extremely difficult to assess the relative contributions of compaction and cementation (Milliken and Day-Stirrat, 2013). For instance, for the porosity loss in mudrocks as described in the widely cited porosity-depth plots (Mondol et al., 2007), the separate effects of compaction and cementation are still unknown.

Alignment of different detrital components (Figure 61), broken fragments of brittle grains (Figure 59) and suture-like zones along grain contacts of silt-sized foraminifer grains (Figure 60) are evidence of compaction in the Eagle Ford. Because foraminifers are one of the main silt-size and sand-size components in the Eagle Ford, variations in the fabric formed due to compaction are most clearly seen in association with foraminifer grains.

In the Eagle Ford, the spherical shapes of pelagic foraminifers (globigerinids) are mostly preserved (Figure 64); only in rare cases are some of them collapsed (Figure 62), dissolved or broken into smaller pieces (Figure 63) even in the high-maturity samples, with a few exceptions. This inhibition of compactional collapse of the intraskeletal pores can be explained by the early cementation in the Eagle Ford (Hart et. al., 2013). On the other hand, it is extremely difficult to find completely intact inoceramid plates or thin-walled mollusks, which can be also associated with the physical environment conditions.

In order to understand the effect of compaction on the Eagle Ford, total porosity values and initial porosity values are compared and compactional porosity loss is calculated. Although relative contributions of cementation and compaction are not known in the case of mudrock porosity loss, by analogy to sandstone compactional model proposed by Lundegard (1992) and Ehrenberg (1995) (Equation 2), the upper bounds of compactional porosity loss (COPL) can be at least approximately constrained. For the initial porosity values different studies reviewed in the study of Milliken and Day-Stirrat (2013) are used. Initial porosity value for marine mud is in the range of 80%, as determined from the actual core sampling and measurements of the deep clay-rich Recent to Tertiary sediments reported by Velde (1996). The range of porosity values at the time of deposition for muds is stated as 60% to 80% in the study of Bridge and Demicco (2008). 60% is used as another initial porosity value (P_i). The lower initial porosity values (Pi) used for the porosity decline curves, which is approximately defined as 30% in the study of Proshlykov (1960), reflects the rocks that have been buried and uplifted. Another parameter for the COPL calculation is IGV (Intergranular volume) (Equation 1). Total porosity values provided by Shell Company are used as intergranular porosity value, with the understanding that for this calculation we are using a combination of inter-and intra-granular porosity as potentially involved in the bulk volume loss. For the intergranular cement, three assumptions are employed. In the first case cement is assumed as zero, secondly, as 10%, and thirdly, as 20%, an amount consistent with the visual estimates of cement content in foraminifer-rich samples of the Eagle Ford. If initial porosity values are lower, the effect of cement precipitation increases and compactional porosity loss (COPL) decreases accordingly. Using these constraints, the upper bound of COPL is 79.4% where initial porosity 80%, and total porosity is 3.1% in the medium-maturity Well 2 sample CH4 (953.29m) and no cement precipitation is observed. The calculated COPL values with plausible assumptions are parallel to the expected results. The lowest COPL value, which is approximately 40%, is observed in the relatively shallower samples in the condition of high cement precipitation.

Compactional strain (volume loss caused by compaction and represented by COPL) (Table 14, Table 15, and Table 16) is quite large even with conservative assumptions for initial porosity (Pi) values and a plausible amount of cement. Although high initial porosity (~80%) values are proposed for the muds at the time of deposition, 60% initial porosity value is also used for the calculations to observe how COPL values are affected and to test the relative importance of earlier versus later compaction and cementation on the porosity loss. In the only case where initial porosity and cement value are taken as 60% and 20%, respectively, COPL values fall below 50%. In all other cases, COPL is more than 50%. It can be concluded that, compaction most likely outweighs cementation as a cause of porosity decline in these rocks.

Equation 1: Formula used for the calculation of intergranular volume percentage (IGV%) (Paxton et. al., 2002). The volume of detrital matrix is inappropriate in the calcuation of IGV in mudrocks as all the intergrain spaces need to be considered, even between clay-size particles.

$$IGV(\%) = V_{intergranular\ porosity} + V_{\boldsymbol{intergranular}\ cement} + (V_{detrital\ matrix})$$

Equation 2: Formula of compactional porosity loss defined by Lundegard (1992) and Ehrenberg (1995)

$$COPL = P_i - \frac{(100 - P_i) * IGV}{(100 - IGV)}$$

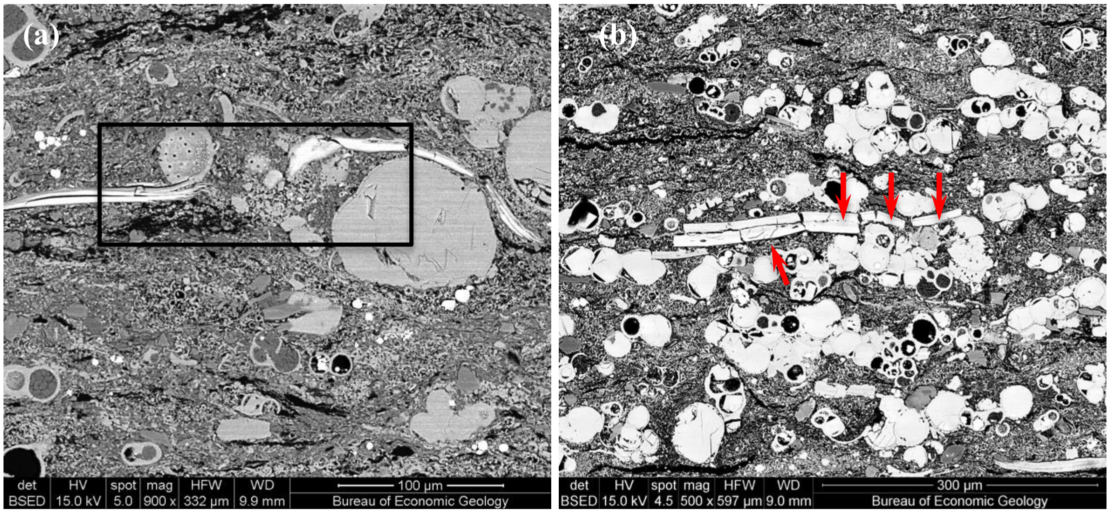

Figure 59: Broken phosphate fragments positioned between the coarser-grained framework in the Eagle Ford indicate compaction are shown in the (a) BSED image of the Well 1 sample 11 (b) BSED image of the Well 1 sample 16. Note that broken Ca-phosphate is wrapping around the big foraminifer grain in the sample 11.

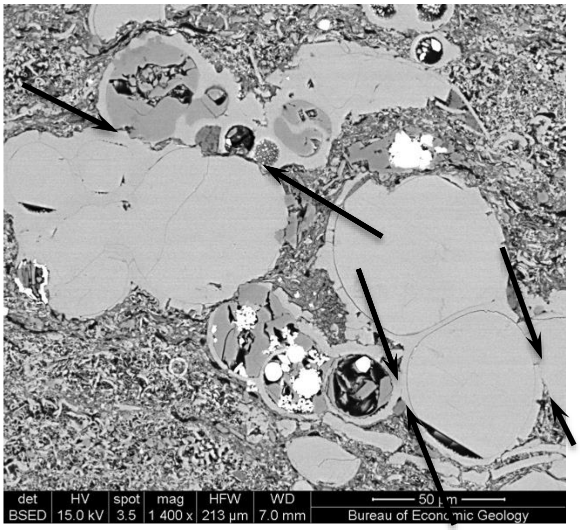

Figure 60: Suture-like zones along the contacts of the foraminifer grains (possible pressure dissolution) formed due to the compaction is shown in the BSED image of the low-maturity outcrop Well 1 sample 11 (115.48m). Note that black arrows indicate the grain contacts between foraminifer grains.

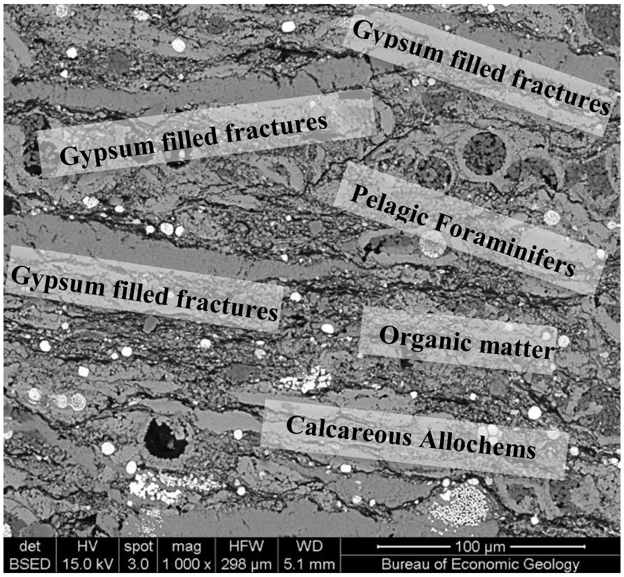

Figure 61: Preferred orientation of fabric including calcareous allochems, pelagic foraminifer and organic matter and gypsum-filled fractures is shown in the BSED image of outcrop Lozier Canyon LZ-2 sample. Note that alignment is disrupted by the broken gypsum filled fractures at the top of the sample. These gypsum-filled fractures are interpreted as an outcrop-weathering phenomenon (below).

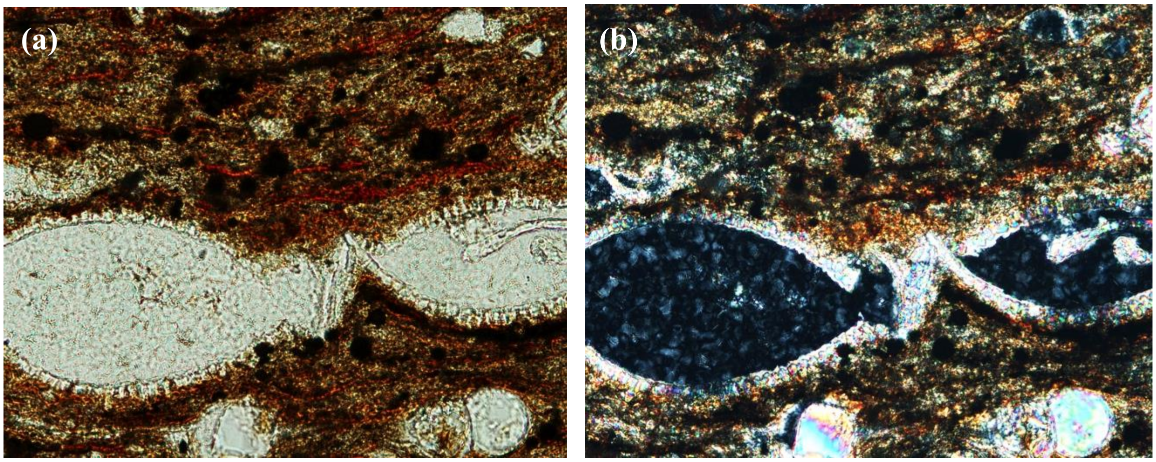

Figure 62: Partly collapsed chambers of pelagic foraminifers filled with kaolinite, shown in transmitted (a) plane-polarized light image (b) cross-polarized light image of low-maturity outcrop Well 1 sample 1 (151.88-151.85)

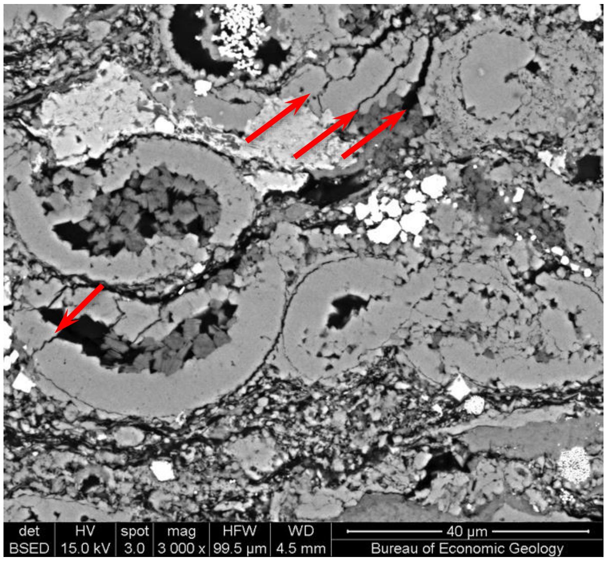

Figure 63: Broken and collapsed tests of the foraminifers shown in a backscattered image (BSED image) of the Lozier Canyon outcrop sample LZ-2. Note that red arrows show open microfractures generated due to compaction and their alignments are similar in direction.

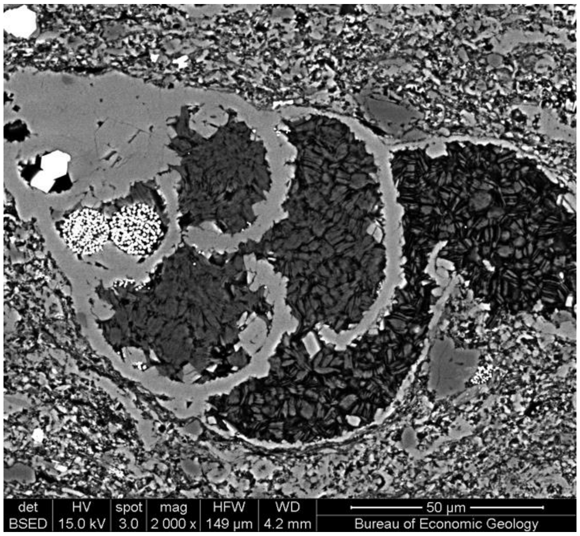

Figure 64: The open chamber of pelagic foraminifer, which is filled with early diagenetic kaolinite cement, is shown in the backscattered image (BSED image) of the high-maturity Well 4 sample 1-90 (2800.9m)

Table 14: Calculation of compactional porosity loss with different initial porosity values and different cement amounts for the medium-maturity well.

Sample NO	Depth (ft)	Depth (m)	Dry Helium Porosity % of BV	IGV (cement=0)	IGV (cement=10%)	IGV (cement=20%)	COPL(Pi=80%) (cement=0)	COPL(Pi=80%) (cement=10%)	COPL(Pi=80%) (cement=20%)	COPL(Pi=60%) (cement=0)	COPL(Pi=60%) (cement=10%)	COPL(Pi=60%) (cement=20%)
CH1	2989.55	911.21	7.7	7.7	17.7	27.7	78.3	75.7	72.3	56.7	51.4	44.7
CH2	3004.45	915.76	8.0	8.0	18.0	28.0	78.3	75.6	72.2	56.5	51.2	44.4
CH3	3117.3	950.15	8.6	8.6	18.6	28.6	78.1	75.4	72.0	56.2	50.9	44.0
CH4	3127.6	953.29	3.1	3.1	13.1	23.1	79.4	77.0	74.0	58.7	54.0	48.0
CH5	3162.3	963.87	12.6	12.6	22.6	32.6	77.1	74.2	70.3	54.2	48.3	40.7
CH6	3182.4	970.00	13.0	13.0	23.0	33.0	77.0	74.0	70.1	54.0	48.1	40.3
CH7	3192.55	973.09	5.3	5.3	15.3	25.3	78.9	76.4	73.2	57.8	52.8	46.5

Table 15: Calculation of compactional porosity loss with different initial porosity values and different cement amounts for the high-maturity well.

Sample NO	Depth(ft)	Depth(m)	Dry Helium Porosity % of BV	IGV (cement=0)	IGV (cement=10%)	IGV (cement=20%)	COPL(Pi=80%) (cement=0)	COPL (Pi=80%) (cement=10%)	COPL (Pi=80%) (cement=20%)	COPL (Pi=60%) (cement=0)	COPL (Pi=60%) (cement=10%)	COPL (Pi=60%) (cement=20%)
EF3 1-31	8283.45	2524.80	6.4	6.4	16.4	26.4	78.6	76.1	72.8	57.3	52.2	45.7
EF3 1-61	8313.25	2533.88	6	6	16	26	78.7	76.2	73.0	57.4	52.4	45.9
EF3 1-66	8318.55	2535.49	5.1	5.1	15.1	25.1	78.9	76.4	73.3	57.9	52.9	46.6
EF3 1-136	8388	2556.66	9.3	9.3	19.3	29.3	77.9	75.2	71.7	55.9	50.4	43.4

Table 16: Calculation of compactional porosity loss with different initial porosity values and different cement amounts for the high-maturity well.

Sample NO	Depth(ft)	Depth(m)	Dry Helium Porosity % of BV	IGV (cement=0)	IGV (cement=10%)	IGV (cement=20%)	COPL (Pi=80%) (cement=0)	COPL (Pi=80%) (cement=10%)	COPL (Pi=80%) (cement=20%)	COPL (Pi=60%) (cement=0)	COPL (Pi=60%) (cement=10%)	COPL (Pi=60%) (cement=20%)
EF4 1-5	9104.50	2775.05	6.4	6.4	16.4	26.4	78.6	76.1	72.8	57.3	52.2	45.7
EF4 1-10	9109.30	2776.51	4.5	4.5	14.5	24.5	79.1	76.6	73.5	58.1	53.2	47.0
EF4 1-25	9124.30	2781.09	6.6	6.6	16.6	26.6	78.6	76.0	72.7	57.2	52.0	45.5
EF4 1-35	9134.10	2784.07	3.6	3.6	13.6	23.6	79.3	76.9	73.8	58.5	53.7	47.7
EF4 1-75	9174.10	2796.27	7.1	7.1	17.1	27.1	78.5	75.9	72.6	56.9	51.7	45.1
EF4 1-80	9179.00	2797.76	6.4	6.4	16.4	26.4	78.6	76.1	72.8	57.3	52.1	45.6
EF4 1-90	9189.25	2800.88	6.9	6.9	16.9	26.9	78.5	75.9	72.6	57.0	51.8	45.3
EF4 1-100	9199.00	2803.86	4.9	4.9	14.9	24.9	79.0	76.5	73.4	57.9	53.0	46.8

CEMENTATION

Cementation is a significant diagenetic process in sandstones (Blatt, 1979; Hayes, 1979) and limestones (Scholle and Halley, 1985; Pettijohn et. al., 1987; Milliken and Day-Stirrat, 2013). Cement is most simply defined as the mineral matter precipitated from aqueous solution into primary void space (Milliken and Day-Stirrat, 2013). The cement definition requires minor modifications for sandstones versus limestones and also in terms of drawing distinctions with replacement. The term is mostly used for any pore filling mineral including both primary intragranular pores and dissolved grains for limestones (Scholle and Ulmer-Scholle, 2003). For mudrocks the definition of cement applied for limestones is preferred in because of the generally significant biogenic content and the strong effects of early diagenesis in generating intragranular pores (Milliken and Day-Stirrat, 2013). Intragranular cements, intergranular cements, and fracture filling cements filling both primary and secondary pores are all observed cement types in mudrocks. In the Eagle Ford, various minerals are identified as intragranular cement, which is more abundantly observed compared to intergranular cement. Calcite, dolomite, kaolinite, framboidal pyrite, euhedral pyrite, and quartz are intragranular cement types observed in the Eagle Ford. Calcite, dolomite, quartz, phosphate and euhedral and framboidal pyrite are also identified in the matrix as intergranular cement.

Calcite cement is observed in all samples and in variety of forms. However, it is problematic to discriminate authigenic calcite inside the carbonate aggregates because of the aforementioned issue related to crystal size. Calcite cement is most easily observed in the pore spaces within foraminifers (Figure 65).

Figure 66 displays other types of calcareous and non-calcareous fossils that contain cement. Calcite cement is mostly interpreted as the product of early diagenesis, and can be precipitated together with kaolinite, which is also formed during early diagenesis (Figure 65). The existence of calcite and kaolinite within intraparticle pore space within the delicate shells that have not collapsed can be considered as evidence for the early diagenetic cement in the Eagle Ford. Early diagenesis occurs within the first few meters of burial where redox processes are dominant (Berner, 1980; Aplin and Macquaker, 2011). Calcite, dolomite, kaolinite, and pyrite, which are early diagenetic products, are precipitated prior to the significant compaction in the Eagle Ford as evidence by the uncollapsed foraminifer shells filled by their cements. The crystal size of the early calcite cement is variable and mostly depends on the size of the foraminifer chambers as they frequently fill pore space within the tests. Although calcite cement is observed in some cases as a single crystal (Figure 65) filling the entire intraparticle pore space of the foraminifer, the cement in other cases is composed of more than one crystal. Another form of calcite cement is fracture filling. Calcite is observed as cement within the microfractures between the inoceramid plates (Figure 67) and natural fractures at different scales in the matrix (Figure 68). Some microfractures are still open whereas some of them are completely filled with calcite.

Another major cement type, which is only identified as pore filling, is kaolinite. It is mostly observed as intragranular pore filling cement within the coarse-grained framework of the Eagle Ford (Figure 69). Fine-grained intragranular to intergranular pore-filling kaolinite is identified rarely in the matrix due to challenges caused by fine-grained nature of grains and authigenics and size of the pores in the matrix (Figure 70). Kaolinite precipitation of similar form is also widespread in other mudrocks (Milliken et.

al., 2012(c)). Kaolinite is not observed as replacement in contrast to several other cements in the Eagle Ford (below) although kaolinite can infill both primary and secondary porosity and occur as replacement of both silicate and carbonate grains in marine mudrocks in the study of Milliken et. al. (2012(c)). Another type of kaolinite cement precipitation observed rarely is grain coating around some lithic fragments and feldspars in the low-maturity outcrop Well 1 (Figure 71).

Dolomite cement is only observed in samples from the low-maturity Well 1 samples and few medium-maturity Well 2 samples. Dolomite is observed in more cases as a replacement. Discrimination of *in situ* displacive dolomite versus reworked detrital dolomite is problematic. Dolomite cement is mostly observed as matrix-dispersed euhedral crystals. Sizes of crystals observed in the matrix are smaller compared to replacement type of dolomite, a few microns and dominantly clay-size. Such fine-grained dolomite is not abundant. In the EDS X-ray maps, zoning within dolomite crystals, which is associated with the growth of the crystals, can be seen. Also, similar to other intragranular pore-space-filling authigenic phases, larger euhedral dolomite crystals are observed within the foraminifer tests (Figure 72).

Framboidal pyrite formation is commonly observed in many organic-rich mudrocks and in all the samples of the Eagle Ford reported here. Sizes of framboids are variable however; the most common size is around 5-10 microns. The size of euhedral crystals within framboids is also variable. Framboids grow within intragranular pore spaces of the fossil fragments, dominantly foraminifers, as intragranular cement, and in the matrix as cement or displacive authigenic crystals (Figure 73 and Figure 74). There is no systematic change in the distribution and size of the framboidal pyrite with the variable maturity levels and depths (Figure 75). Euhedral pyrite can be both observed as replacements (following section) and as cement. Euhedral pyrite is also observed in the Eagle Ford as an intraparticle pore filling, interparticle pore filling and fracture pore filling. All samples have euhedral pyrite cement similar to framboidal pyrite. Size of the individual euhedral pyrite is mostly clay-sized.

Quartz is another major cement type in the Eagle Ford (~on the average of 12%BV authigenic quartz precipitation depend on the medium maturity and high maturity wells' results and majority of them is cement). Euhedral crystals of microquartz are identified in some samples of low-maturity outcrop Well 1 mostly in the Lower Eagle Ford. In the medium-maturity and high-maturity wells, quartz cement, which is widely dispersed in the matrix, is a common constituent although the clay and calcite are volumetrically more abundant. As explained previously, detrital versus authigenic quartz is discriminated firstly with the observation of crystal shape and color intensities in cathodoluminescence, which is the most reliable petrographic method for discrimination of detrital vs. authigenic quartz. Authigenic quartz takes on a variety of forms: matrix-dispersed euhedral clay-sized microquartz (Figure 79), euhedral to subhedral silt-size quartz crystals inside foraminifers (Figure 77) and organic particles (Figure 76), and as a blob- shaped aggregates (Figure 78), which are possibly related to biosiliceous debris (Figure 80). Among them, the majority of authigenic quartz in the Eagle Ford is microquartz, which is widely dispersed in the clay-size matrix. Bulk data analysis including both detrital and authigenic quartz percentages (XRD results) and point count results (which reference only detrital quartz content) are compared to how the authigenic quartz content differs with depth and maturity. Bulk data analysis reveals that total quartz percentages are approximately same in the medium-maturity Well 2 and high-maturity

Well 3 and Well 4 samples. As mentioned earlier in the detrital quartz section, among the components of bulk quartz data, authigenic quartz is the dominant form of quartz in the Eagle Ford by percentage although detrital quartz amount differ in the medium-maturity and high-maturity samples.

Ca-phosphatic cement is widespread but volumetrically small (<2% with some exceptions). It occurs primarily as matrix-dispersed smaller crystals (Figure 81), and rarely, in some of the low-maturity well samples; however, almost all samples from the high-maturity well contain phosphate cement, which can be mostly considered as a product of later diagenesis. Nature of the Ca-phosphate cement is similar to blob-shaped authigenic microquartz cement in terms of crystal size and distribution; however it is less abundant.

Mg-chlorite is also observed as cement within the pore space of the intrabasinal grains (mostly foraminifers and radiolaria) (Figure 84) and in the matrix together with or without kaolinite. Mg-chlorite is both primary pore space filling (Figure 82) and secondary pore space filling (Figure 83). Although it is mostly identified in the high-maturity Well 3 and 4 samples, one of the UEF sample of the low-maturity outcrop Well 1 sample as an exception (Figure 82). Because the habit of Mg-chlorite cement is similar to that of kaolinite and in some of the high-maturity samples they fill the pore space together, it seems to have an association with kaolinite. Volumetrically small amount of Mg-chlorite cement is also observed in the matrix similar to kaolinite.

Minor amounts of bitumen are also identified in the intraparticle pore space of calcareous foraminifer tests of the LEF section of the Well 1 samples (Figure 86). A second type of bitumen, which is associated with the organic-hosted pores in medium-maturity and high-maturity wells are identified in the Eagle Ford. The bitumen identified in the low-maturity well samples is more isolated compared to high-maturity well samples. It is extremely difficult to differentiate intraparticle pore filling bitumen and epoxy using X-ray maps hence light microscopy images are used to discriminate intraparticle pore filling bitumen in the low-maturity outcrop well samples.

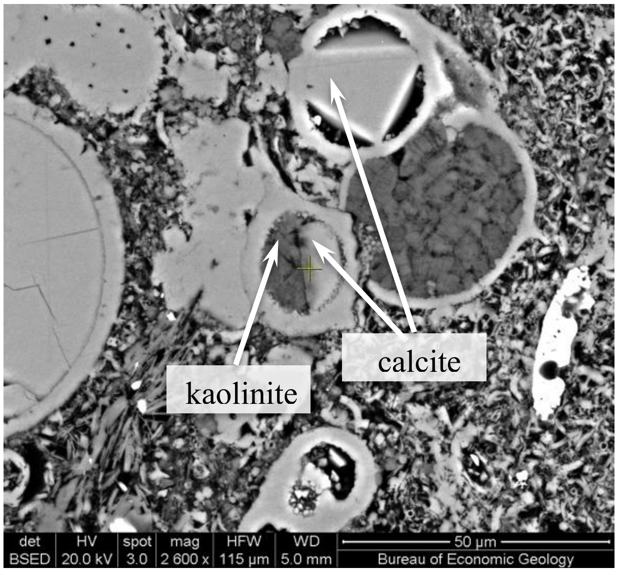

Figure 65: Precipitation of kaolinite and calcite within the foraminifer test is shown in the BSED image of the low-maturity outcrop Well 1 sample 8 (128.91m).

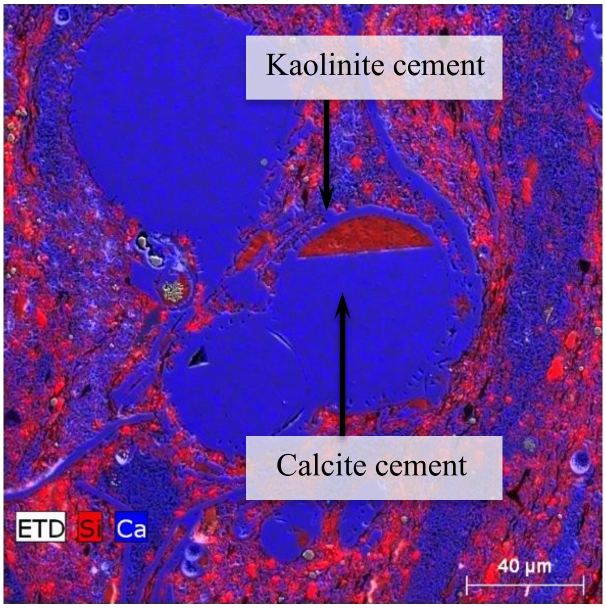

Figure 66: Calcite cement (blue) and kaolinite cement (red due to absence of Al map) filling the pore space inside the foraminifer is shown in the EDS X-ray map of the low-maturity outcrop Well 1 sample 10 (122.94-122.91m).

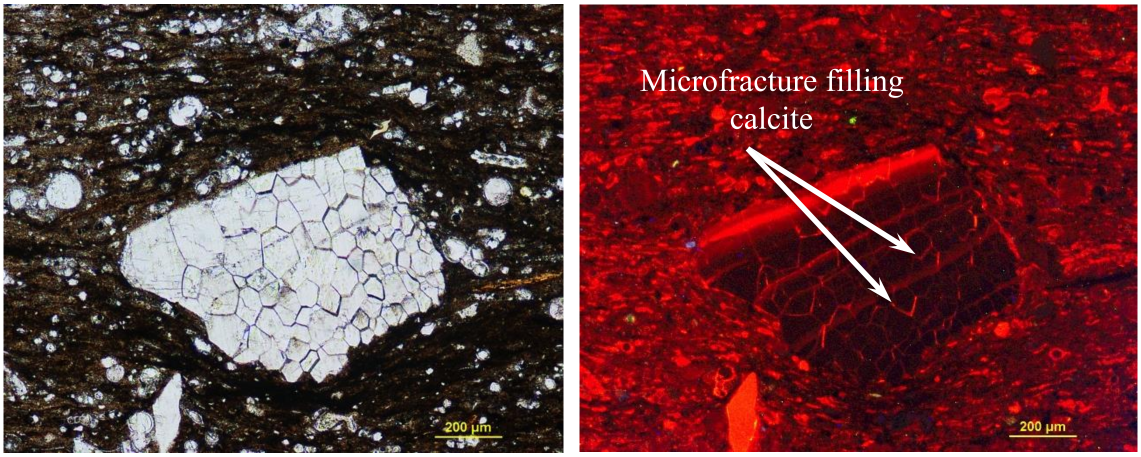

Figure 67: Microfracture filling calcite within an inoceramid plate is shown in the (a) transmitted plane-polarized light image (b) light microscopy based cold-cathode cathodoluminescence image of the low-maturity outcrop Well 1 sample 23. Note that bright orange color shows fracture filling calcite cement in the CL image.

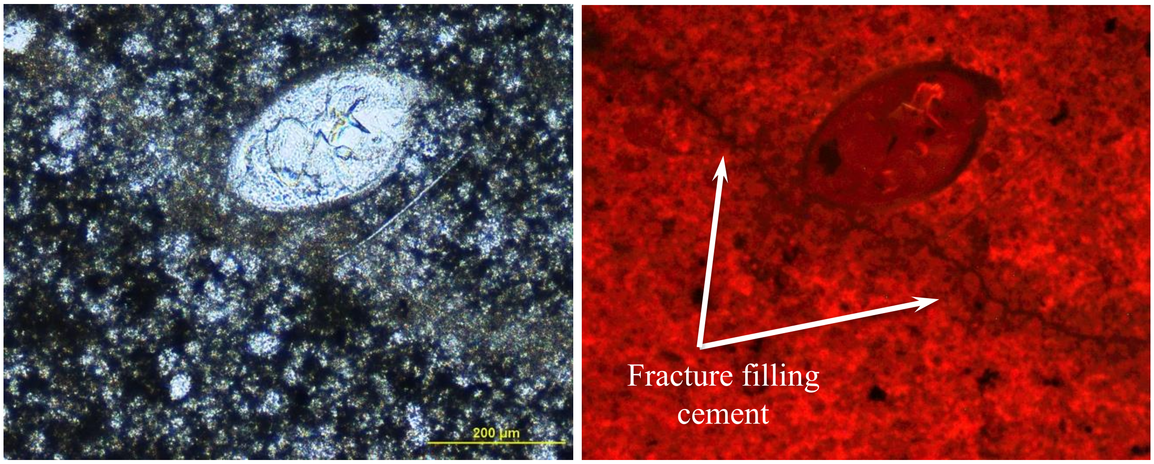

Figure 68: Microfracture filling cement shown in the (a) transmitted plane-polarized light image (b) light microscopy based cold- cathode cathodoluminescence image of the low-maturity outcrop Well 1 sample 18. Note that fracture is partly filled and dark color indicates open part of the fracture.

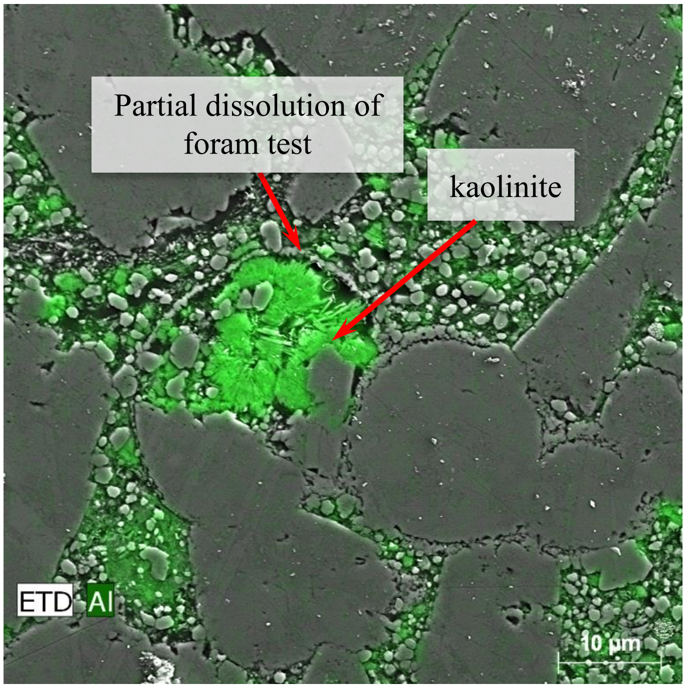

Figure 69: Partial dissolution of foraminifer test and primary intraparticle pore filling kaolinite is shown in the EDS X-ray map of the outcrop Lozier Canyon LZ-1 sample

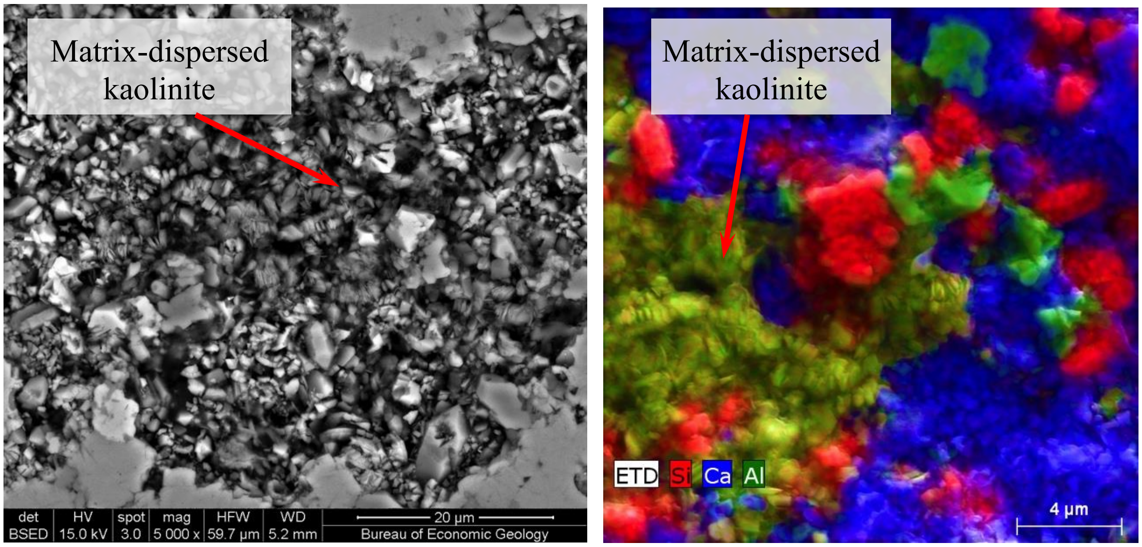

Figure 70: Matrix-dispersed kaolinite is shown in the (a) BSED image (b) EDS X-ray map of the outcrop Lozier Canyon LZ-3 sample

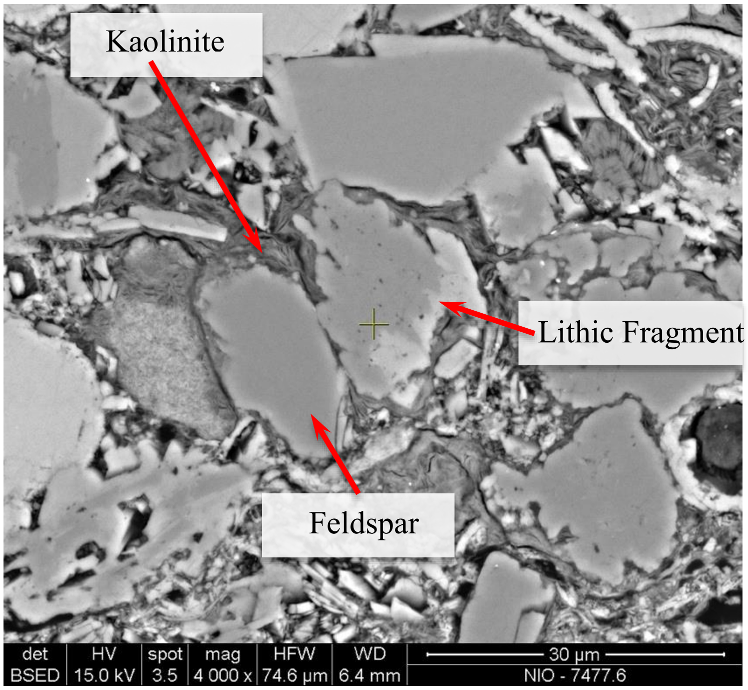

Figure 71: Kaolinite cement as a grain coating is observed in the backscattered image (BSED) of the low-maturity outcrop Well 1 sample 12 (110. 04m)

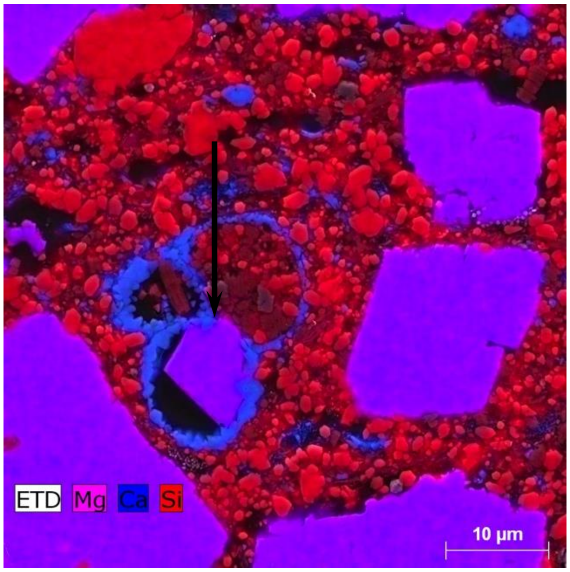

Figure 72: Dolomite cement (purple) filling the pore space inside the foraminifer early diagenesis is shown in the EDS X-ray map of the outcrop Lozier Canyon LZ-1 sample. Microquartz is red; calcite is blue.

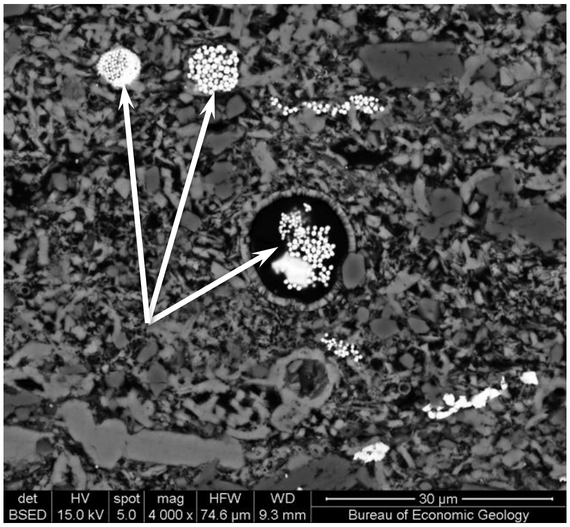

Figure 73: Framboidal pyrite precipitation within the foraminifer test and pore space in the matrix are shown in the BSED image of the medium-maturity Well 2 sample CH5 (963.78m). Note that some of the framboids have loosely packed subcrystals whereas some of them are densely packed.

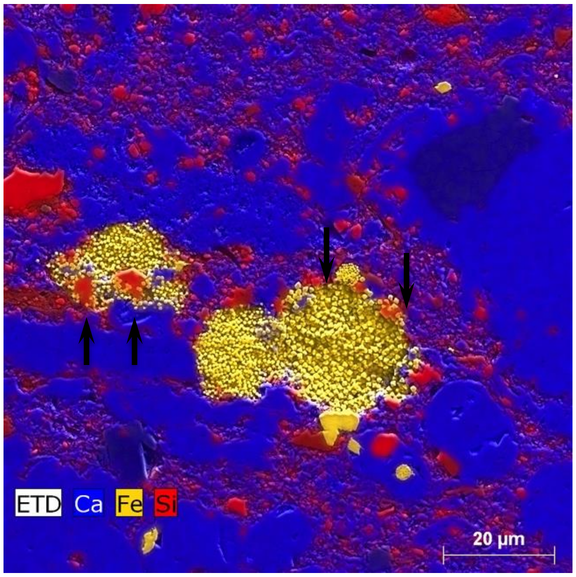

Figure 74: Framboidal pyrite precipitation in the pore space of possible fossil fragment (due to circular shape of the pore) is shown in EDS X-ray maps of medium Well 2 CH1 sample (911.28m). Note that authigenic quartz is intergrown with framboidal pyrite (shown with black arrows) (similar to poikilotopic texture).

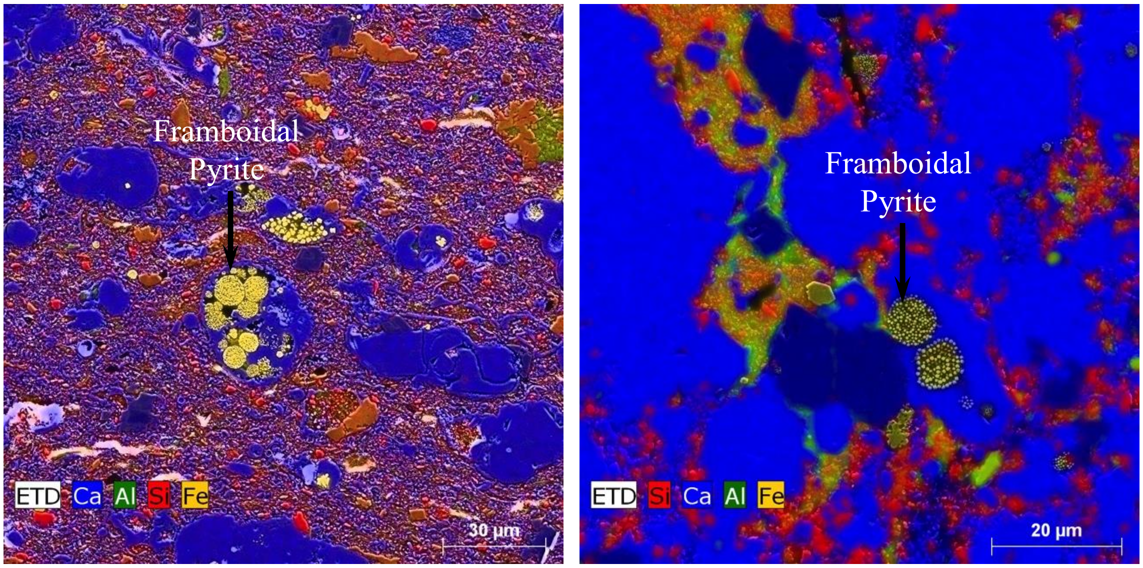

Figure 75: Framboidal pyrite is shown in the EDS X-ray maps of the (a) low-maturity outcrop Well 1 sample 14 as a pore filling cement (b) high-maturity Well 4 sample 1-80 as a pore filling cement. Note that crystal sizes are similar in both samples.

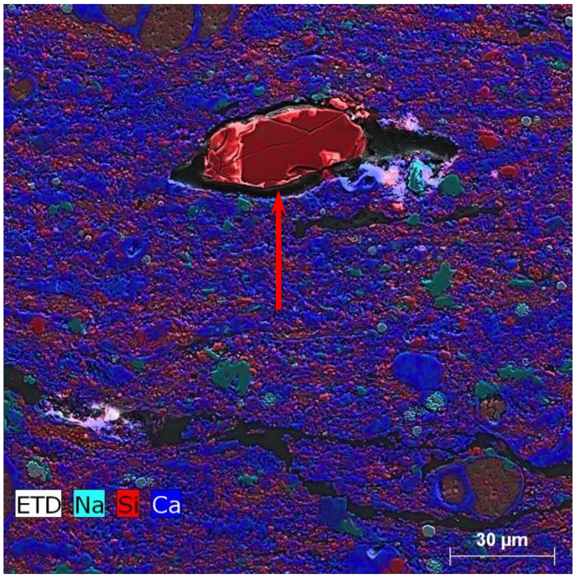

Figure 76: Pore filling authigenic quartz (red) is shown in the EDS X-ray maps of medium-maturity Well 2 sample CH5 (963.78m). The quartz fills the internal space within an organic particle, possibly an algal spore.

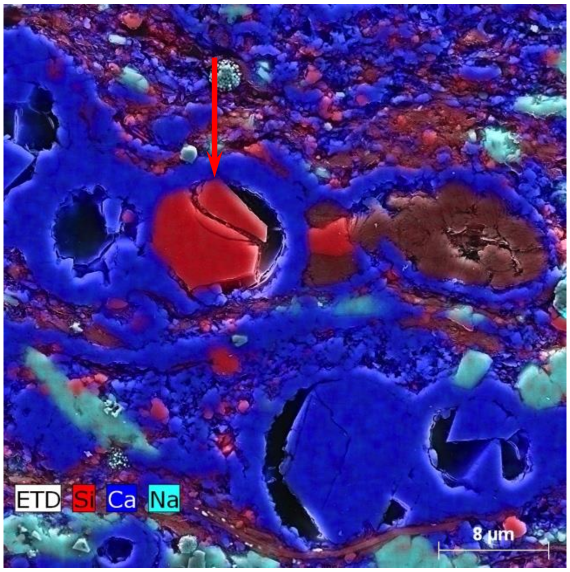

Figure 77: Silt-sized euhedral authigenic quartz (red) growing in the pore space of foraminifer test is shown in the EDS X-ray maps of medium-maturity Well 2 sample CH7 (973.26m)

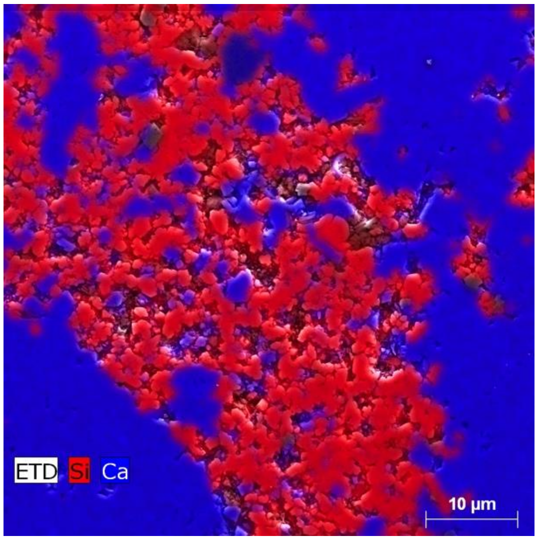

Figure 78: Blob- shaped authigenic microquartz (red) widely dispersed in the matrix is shown in the EDS X-ray maps of the outcrop Lozier Canyon LZ-3 sample. Calcite is blue.

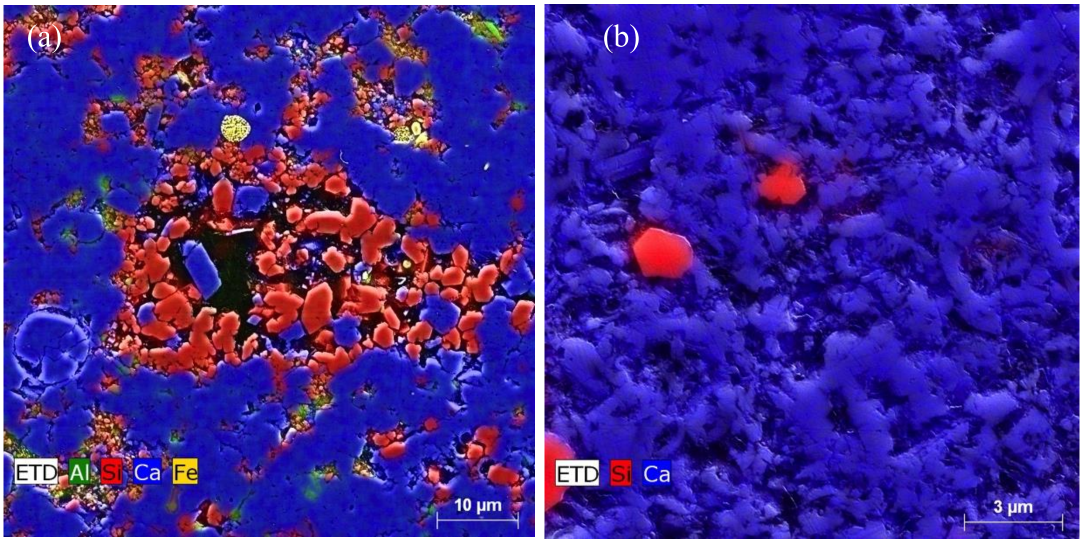

Figure 79: Clay-size euhedral authigenic microquartz (red) growing (a) in the interparticle pore space (b) within the carbonate aggregates including pellets and coccolith fragments are shown in the EDS X-ray maps of the high-maturity Well 4 sample 1-35 (2784.09m) and medium-maturity Well 2 sample CH3 (950.24m), respectively. Calcite is blue. Pyrite is yellow.

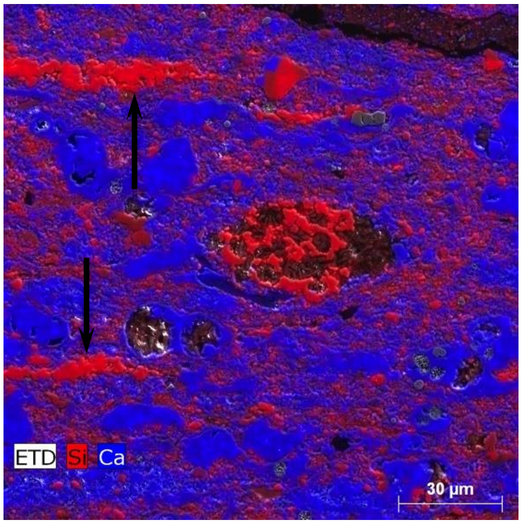

Figure 80: Blob- shaped biosiliceous aggregates (possible agglutinated foraminifers; arrows) are shown in the EDS X-ray maps of the high-maturity Well 4 sample 1-75. (2796.24m). Central grain is partially quartz-replaced radiolarian with kaolinite infilling. Quartz is red. Calcite is blue.

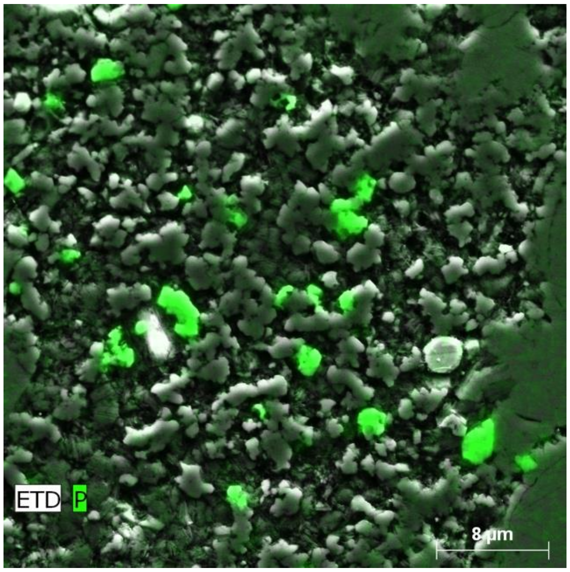

Figure 81: Matrix-dispersed clay-size Ca-phosphate cement is shown in the ETD secondary image with X-ray map overlay; Lozier Canyon outcrop sample LZ-3.

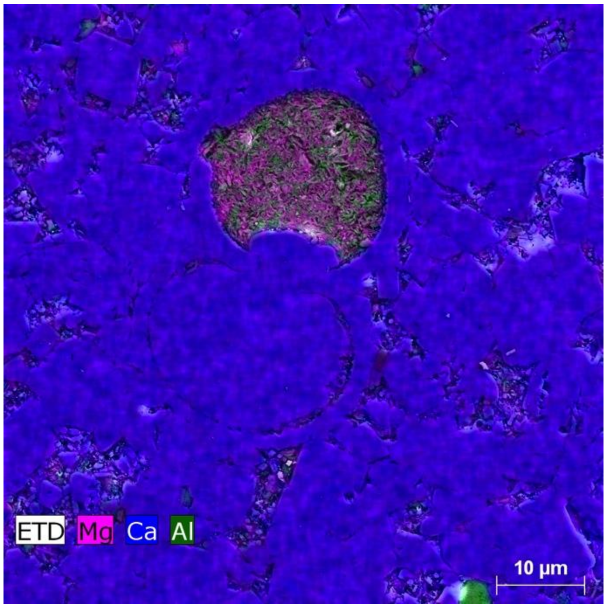

Figure 82: Mg-clay (possible chlorite) mixed with kaolinite inside the chamber of foraminifer is shown in the EDS X-ray map of the low-maturity outcrop Well 1 sample 18 (88.93-88.8m)

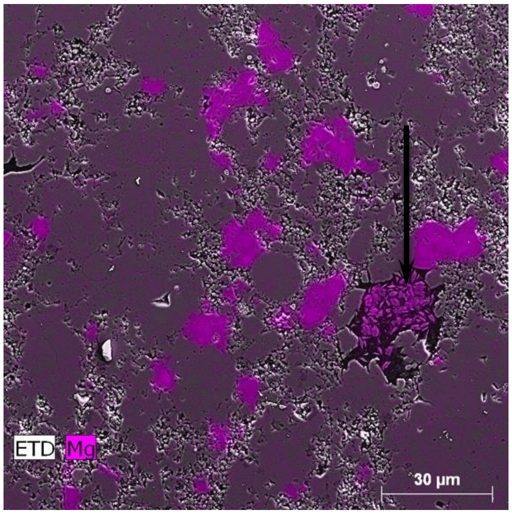

Figure 83: Precipitation of Mg-chlorite within the secondary pore? is shown in the EDS X-ray map of the high-maturity Well 4 sample CH4 1-80 (2797.93m).

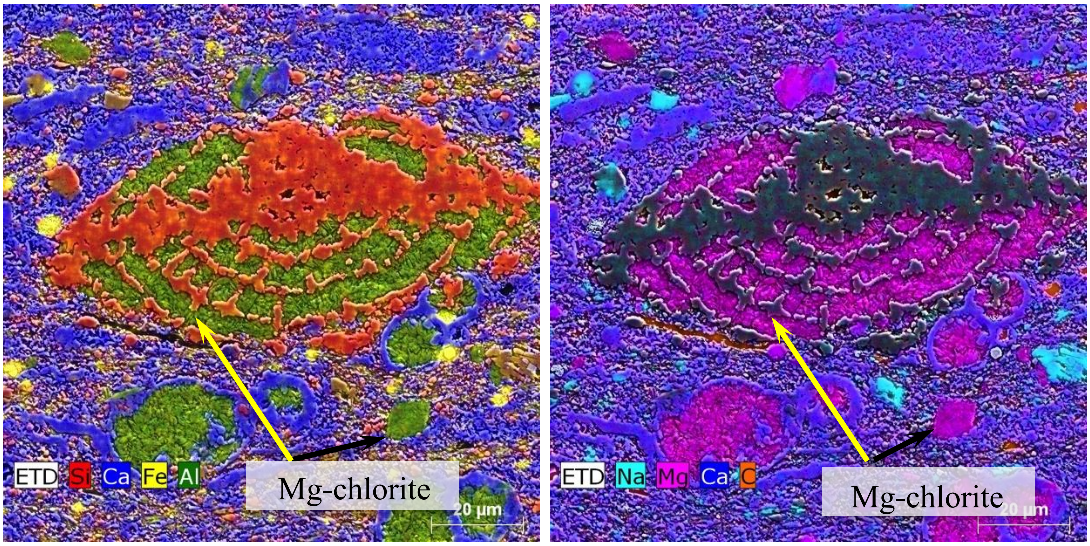

Figure 84: Mg-chlorite precipitates as cement within the silicified radiolarian shell (indicated with yellow arrow) and replaces dolomite in the matrix (indicated with black arrow) and in the EDS X-ray map of the high-maturity Well 4 sample 1-100 (2803.99m). The nature of Mg-chlorite seems pore filling within the radiolarian shell. Note that rhombohedral shape of dolomite is preserved which supports the idea of replacement (below).

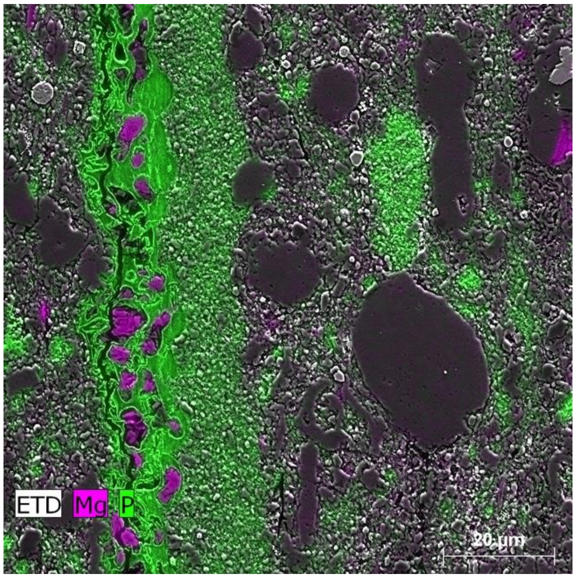

Figure 85: Mg-chlorite (purple) cement as an intragranular pore filling (primary or secondary?) is shown in the EDS X-ray map of the high-maturity Well 3 sample 1-136 (2556.66m).

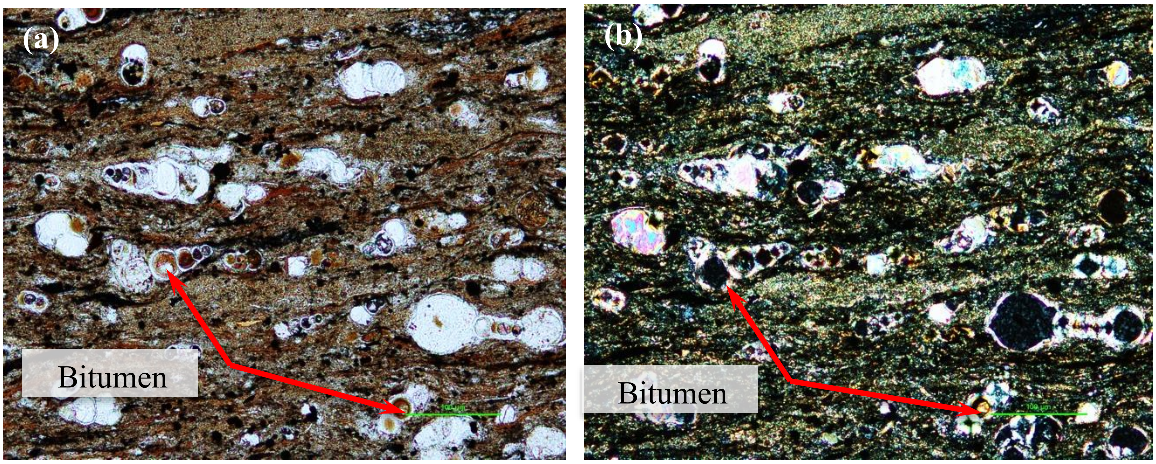

Figure 86: Intraparticle pore filling bitumen is shown in transmitted (a) plane-polarized light microscopy (b) cross-polarized light microscopy images of the low-maturity outcrop Well 1 sample 4 (139.88m). Note that brown colored organic matter indicated by red arrow is bitumen.

Table 17: Cement type authigenic minerals in low-maturity outcrop well samples (Ro: 0.35-0.6%)

Sample NO	Depth (m)	Cement									
		Calcite		Dolomite	Quartz	Phosphate	Clay		Bitumen	Pyrite	
		Fracture Filling	Pore filling				Kaolinite	Mg-chlorite		Framboidal Pyrite	Euhedral Pyrite
23	56.63-56.6	🟧	🟧	🟧		🟧				🟧	🟧
22	57.11-57.08	🟧	🟧	🟧		🟧				🟧	🟧
21	69.88-69.85		🟧	🟧		🟧	🟧			🟧	🟧
20	79.68-79.65	🟧	🟧	🟧						🟧	🟧
19	81.28-81.25		🟧	🟧						🟧	🟧
18	88.93-88.8	🟧	🟧	🟧			🟧	🟧		🟧	🟧
17	92.84-92.81		🟧	🟧			🟧			🟧	🟧
16	98.11-98.08		🟧	🟧		🟧	🟧			🟧	🟧
15	99.85-99.82		🟧	🟧	🟧		🟧			🟧	🟧
14	104.86-104.83		🟧	🟧			🟧			🟧	🟧
13	106.47-106.44		🟧	🟧			🟧			🟧	🟧
12	110.04-110.01		🟧	🟧						🟧	🟧
11	115.48-115.45		🟧	🟧	🟧		🟧			🟧	🟧
10	122.94-122.91		🟧	🟧	🟧	🟧	🟧			🟧	🟧
8	128.91-128.88		🟧	🟧	🟧		🟧		🟧	🟧	🟧
7	133.71-133.68		🟧	🟧	🟧		🟧			🟧	🟧
4	139.88-139.85		🟧	🟧	🟧		🟧		🟧	🟧	🟧
2	149.52-149.49		🟧		🟧					🟧	🟧
1	151.88-151.85		🟧	🟧			🟧		🟧	🟧	🟧

Table 18: Cement type authigenic minerals in medium-maturity well samples (Ro: 0.65-0.75%)

Sample NO	Depth (m)	Depth (ft)	Cement								
			Calcite		Dolomite	Silica	Phosphate	Clay		Pyrite	
			Fracture Filling	Pore Filling				Kaolinite	Mg-chlorite	Framboidal Pyrite	Euhedral Pyrite
CH1	911.28	2989.75		🟧	🟧	🟧				🟧	🟧
CH2	915.79	3004.55		🟧	🟧	🟧				🟧	🟧
CH3	950.24	3117.6	🟧	🟧		🟧		🟧		🟧	🟧
CH4	953.22	3127.35		🟧		🟧		🟧		🟧	🟧
CH5	963.78	3162		🟧		🟧	🟧	🟧		🟧	🟧
CH6	969.95	3182.25		🟧		🟧	🟧	🟧		🟧	🟧
CH7	973.26	3193.1	🟧	🟧		🟧		🟧		🟧	🟧

Table 19: Cement type authigenic minerals in high-maturity well samples (Ro: 1.15-1.32%).

Sample NO	Depth (m)	Depth (ft)	Cement								
			Calcite		Dolomite	Silica	Phosphate	Clay		Framboidal Pyrite	
			Fracture Filling	Pore Filling				Kaolinite	Mg-chlorite	Framboidal Pyrite	Euhedral Pyrite
A3H 1-31	2524.77	8283.35		🟧			🟧			🟧	🟧
A3H 1-61	2533.88	8313.25	🟧	🟧		🟧	🟧	🟧	🟧	🟧	🟧
A3H 1-66	2535.49	8318.55		🟧		🟧	🟧			🟧	🟧
A3H 1-136	2556.66	8388	🟧	🟧			🟧	🟧	🟧	🟧	🟧

Table 20: Cement type authigenic minerals in high-maturity well samples (Ro: 1.16-1.31%)

Sample NO	Depth (m)	Depth (ft)	Cement								
			Calcite		Dolomite	Silica	Phosphate	Clay		Pyrite	
			Fracture Filling	Pore Filling				Kaolinite	Mg-chlorite	Framboidal Pyrite	Euhedral Pyrite
C4H 1-5	2775.04	9104.45	🟧	🟧		🟧	🟧	🟧	🟧	🟧	🟧
C4H 1-10	2776.62	9109.65		🟧		🟧				🟧	🟧
C4H 1-25	2781.10	9124.35		🟧		🟧	🟧			🟧	🟧
C4H 1-35	2784.09	9134.15		🟧		🟧				🟧	🟧
C4H	2787.70	9146	🟧	🟧		🟧	🟧			🟧	🟧
C4H	2790.75	9156		🟧		🟧	🟧		🟧	🟧	🟧
C4H 1-75	2796.24	9174		🟧		🟧	🟧		🟧	🟧	🟧
C4H 1-80	2797.93	9179.55		🟧		🟧	🟧		🟧	🟧	🟧
C4H 1-90	2800.90	9189.3	🟧	🟧		🟧	🟧	🟧	🟧	🟧	🟧
C4H 1-100	2803.99	9199.45		🟧		🟧	🟧		🟧	🟧	🟧
C4H 1-123	2811.06	9222.65		🟧		🟧	🟧	🟧	🟧	🟧	🟧

GRAIN REPLACEMENT

Grain replacement is also common in the Eagle Ford. Major replacive minerals in the Eagle Ford, are carbonates (calcite and dolomite), sulfides (euhedral pyrite, sphalerite (rare)), Ca-phosphate, silicates (quartz and feldspars (mostly albite), Mg-chlorite, and titanium oxide (TiO_2).

Calcite replacement is mostly observed in the Upper Eagle Ford samples in low-maturity outcrop Well 1. Calcite is commonly identified as cement but even in light microscopy images calcite replacement is noted (Figure 87). As explained earlier, biosiliceous grains are mostly replaced by calcite in the Eagle Ford. In each maturity level reported here, highly replaced samples are identified. These carbonate-rich samples are analyzed using a light-microscopy-based CL technique (cold-cathode) to identify diagenetic calcite with variable luminescence properties. Individual crystals of calcite replacing the radiolaria show compositional variation that highlights the ghost-like outlines of former radialaria (Figure 88) in CL. Zoning of individual crystals showing growing texture of calcite replacement is identifiable in the CL.

Dolomite replacement is more pervasive than dolomite cement, as previously mentioned. Also, as explained above whereas size of cement type dolomite crystals are clay-sized, size of the replacement type dolomites reach up to fine silt- (8 μm) to very fine sand-size (100 μm) in the some medium-maturity and high-maturity well samples (Figure 89, and Figure 90). It can be inferred that because replacement type dolomite crystals are bigger in size compared to crystals of dolomite cement, dolomite precipitation can be volumetrically more significant in the samples which replacement type of dolomite is more dominant. Dolomite commonly tends to replace calcite within the foraminifer tests and where the samples are dominated with recrystallized calcite, dolomite replacement is widespread. Also, some lithic fragments are replaced by dolomite.

Quartz replacement, which can be derived from biosiliceous grains in a manner similar to quartz cement, from diagenetic reactions of clay minerals, or from alteration of volcaniclastics is abundant in the Eagle Ford. In order to know whether there is role of diagenesis of clay minerals on the majority of authigenic quartz precipitation, total clay amount obtained from bulk data analysis and detrital clay amount obtained from point counts and authigenic quartz amounts are plotted on the graph (Figure 125). Since no obvious systematic change is observed with the diagenetic clay precipitation and quartz precipitation, the idea that majority of the authegenic quartz is derived from biosiliceous debris in the Eagle Ford is supported. Authigenic quartz precipitation is identified dominantly in the medium-maturity and high-maturity well samples however; this phenomenon is noted in most of Lower Eagle Ford samples of the low-maturity outcrop Well 1. The main forms of quartz replacement is defined as (1) silt-sized subhedral to anhedral quartz (Figure 91) (2) clay-sized euhedral to subhedral microquartz (Figure 93) (3) shell fragment replacement of quartz (Figure 92). Matrix-dispersed authigenic microquartz is considered as cement as explained in the cementation section. Clay-sized euhedral to subhedral microquartz emplaced within carbonate allochems is interpreted as grain replacement; however, there is still a possibility that some portion of this material is secondary pore filling cement (Figure 93). If the pore space between the nucleation surface and the authigenic mineral can be seen, it can be interpreted as cement easily, yet, if they are in contact it is difficult to determine whether it is cement or grain replacement or even displacive.

Another authigenic component observed as a grain replacement is feldspar (Kastner, 1971; Milliken, 1992). Euhedral K-feldspar within a calcareous allochem is identified in the shallower depths and low temperature conditions (Figure 96). In the study of Kastner (1971), the existence of low temperature feldspars in sedimentary rocks is mentioned. Kastner (1971) stated that low temperature authigenic feldspars have euhedral overgrowths with pinocoidal faces in the carbonate rich rocks and mostly replace fossils. Also, another criterion to identify authigenic feldspars is defined as chemical purity in terms of Ca and Na absence for the K-feldspars. These criteria support the idea that low temperature authigenic feldspars can also exist in the Eagle Ford. Aluminium, silica, and potassium are detected in this crystal, but no Na, ruling out the possibility of a detrital volcanic phenocryst. However, there is not enough evidence to prove absolutely the precipitation of authigenic feldspar at the uppermost part of the low-maturity outcrop samples as microprobe analysis was beyond the scope of this study. Albite replacement is more common than K-feldspar replacement in the Eagle Ford and more obvious in the high-maturity well samples. Albite replacement is also identified in the some low-maturity outcrop Well 1 samples, which is recognizable with its euhedral shape (Figure 94). In some high-maturity Well 3 and 4 samples, silt to fine sand size albite crystals are observed rarely as replacement (Figure 95)

Euhedral pyrite in mudrocks is related to conditions of lower sulfide production and lower organic matter content (Taylor and Macquaker, 2000). Euhedral pyrite replacement is observed in all samples and it tends to replace carbonate allochems, dolomite, and albite (Figure 89). Replacement-type euhedral pyrite is observed in almost all LEF samples of the low-maturity outcrop Well 1 and some UEF samples of the same well. Replacement-type euhedral pyrite is bigger in size compared to cement type euhedral pyrite. Abundance of replacement-type euhedral pyrite is more in the high-maturity well compared to low-maturity and medium-maturity well samples. Point counting method has not been applied to pyrite abundances, yet as a visual observation euhedral pyrites including both replacement and cement type are more abundant in high-maturity well samples compared to framboidal pyrites. It can be explained by the particular abundance of replacement type euhedral pyrite in the high-maturity Well 4. Also, pyrite is identified as the partial (Figure 92) to complete replacement of shells with the preservation of shape of the shell (Figure 97 and Figure 98), in the medium-maturity Well 2 and high-maturity wells Well 3 and Well 4.

Authigenesis of kaolinite and chlorite is a common phonemenon in Texas Gulf Coast sediments including mudrocks and adjacent sandstones (Burton et. al., 1987) and it is stated that kaolinite is formed prior to Mg-chlorite in their studies. The chlorite in the Burton et al study (1987) is notably Fe-rich, however, the EDS spectrum reveals Fe-poor Mg-chlorite (the possible forms are identified as sudoite or clinochlore) precipitation in the Eagle Ford samples reported here. Mg-chlorite precipitation is dominantly identified in the high-maturity samples and rarely in others. This observation has parallels with the study of Burton et. al. (1987), who observed conversion of kaolinite to chlorite within foraminiferal tests with increasing depth (Figure 100). Also, in some samples of high-maturity Well 4, it is identified that Mg-chlorite replaces dolomite, which is inferred from the unexpected rhombohedral shape of the Mg-chlorite (Figure 99).

Phosphate replacement, which is also commonly observed in chalk deposition (Hancock, 1975), is another significant phenomenon in the Eagle Ford diagenesis. Phosphate replacement is commonly identified as the replacement of calcite (Figure 101). It is found together with the anhedral to euhedral pyrite replacement, which can suggest that they are associated and their precipitation mechanisms are similar. Our observations suggest late phosphate diagenesis due to dominantly identified authigenic apatite mineral in the medium-maturity and high-maturity well samples with one exception in low-maturity outcrop Well 1 sample 23. It has complicated grain assemblage (micas, feldspars, quartz and lithics) and authigenic minerals (sphalerite and apatite as a replacement and foraminifer filling and fracture filling gypsum).

Authigenic titanium oxide (TiO_2) is identified in some samples of the Eagle Ford (Figure 102 and Figure 103). The unstable nature of detrital TiO_2 increases the possibility to have authigenic TiO_2 in the samples, which is observed almost half of the samples reported here. On the other hand, authigenic TiO_2 is very stable. The reason of expecting to see authigenic TiO_2 commonly is its very stable nature on the contrary to detrital TiO_2.

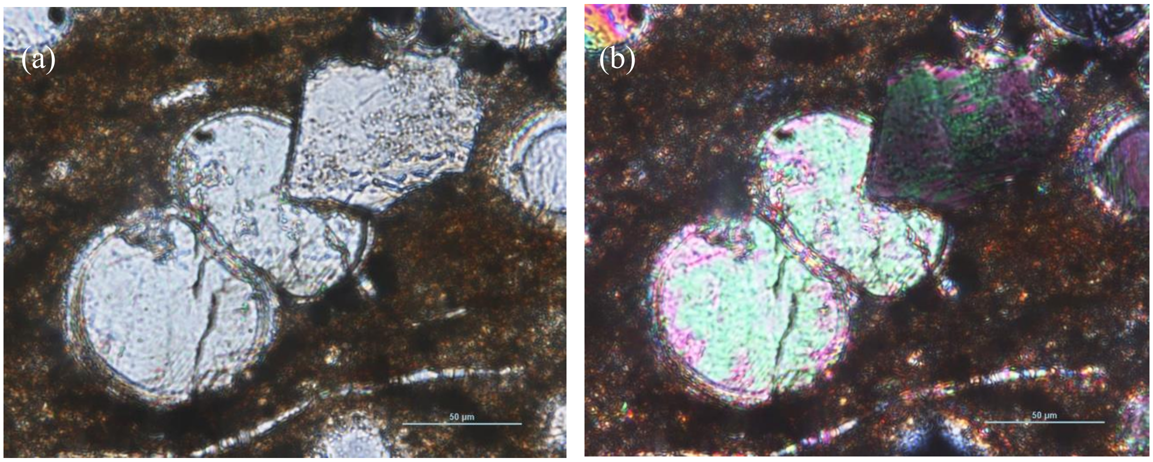

Figure 87: Calcite replacement is shown in transmitted (a) plane-polarized light microscopy image (b) cross-polarized light microscopy image of the low-maturity outcrop Well 1 sample 15 (99.85 m).

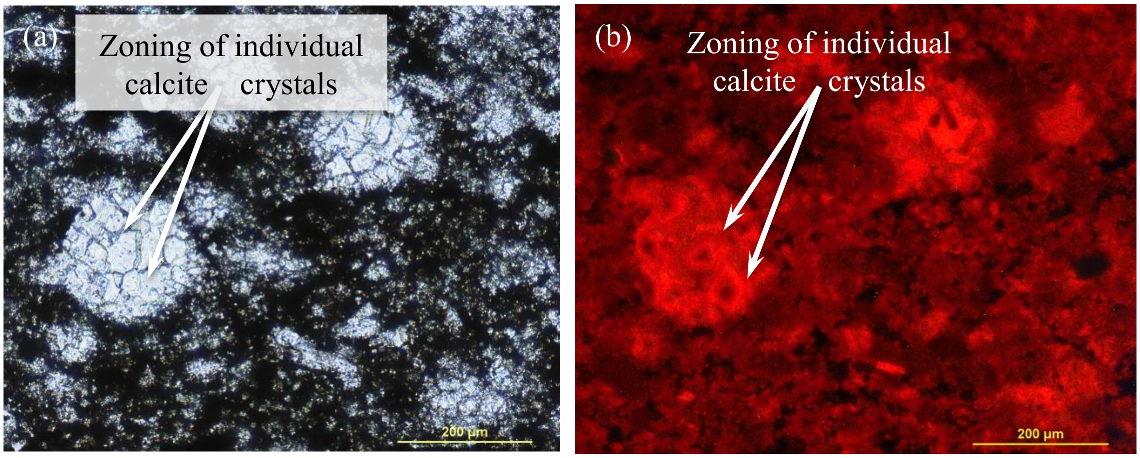

Figure 88: Calcite replacement of biosiliceous grains (radiolaria) and zoning of individual crystals are shown in the (a) transmitted plane-polarized light microscopy image (b) CL image of the sample high-maturity Well 4 sample 1-35 (2784.39m).

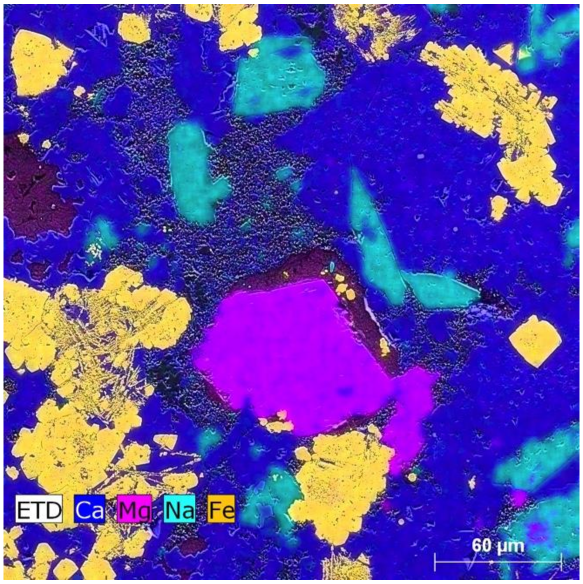

Figure 89: Subhedral dolomite replacement (bright pink) and euhedral pyrite replacement (yellow) are shown in the EDS X-ray map of the high-maturity Well 3 sample 1-66 (2535.49m). Na-feldspar is aqua; calcite is blue.

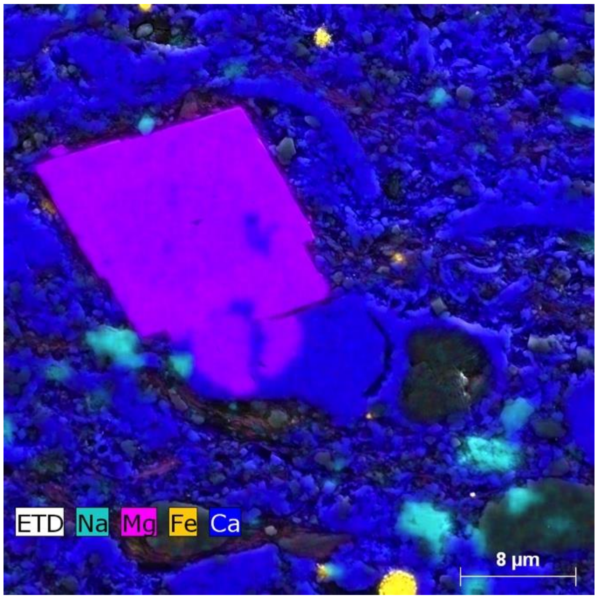

Figure 90: Rhombohedral dolomite (pink) replacing and filling a foraminifer test are shown in the EDS X-ray map of the medium-maturity Well 2 sample CH5 (963.78m). Calcite is blue; Na-feldspar is aqua.

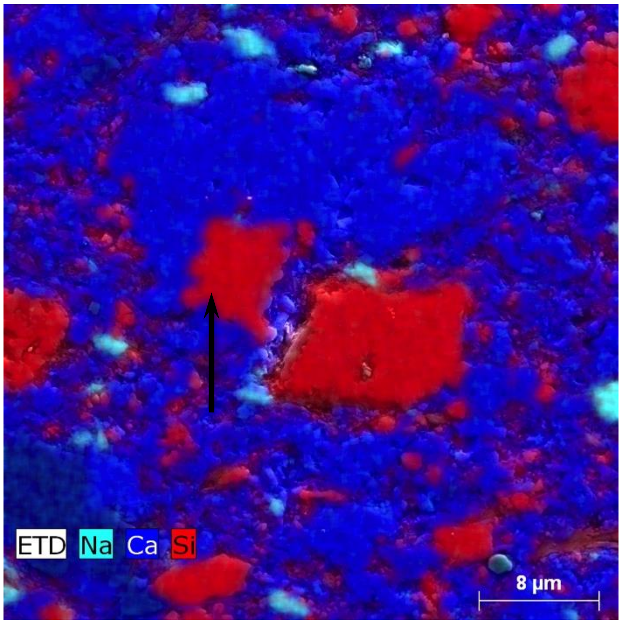

Figure 91: Silt-sized quartz replacement of calcareous allochems is shown in EDS X-ray maps of medium-maturity well CH1 sample (911.28m)

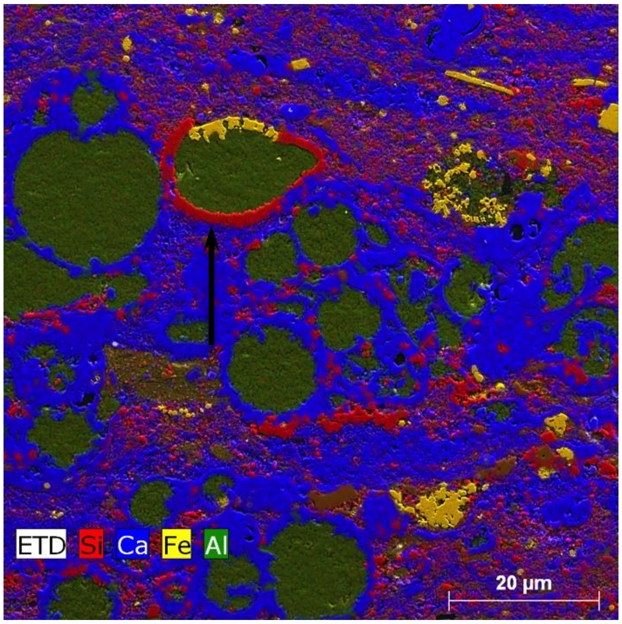

Figure 92: Quartz and pyrite replacement of foraminifer test which is filled with Mg-chlorite is shown in the EDS X-ray maps of high-maturity Well 4 sample 1-90 (2800.9m)

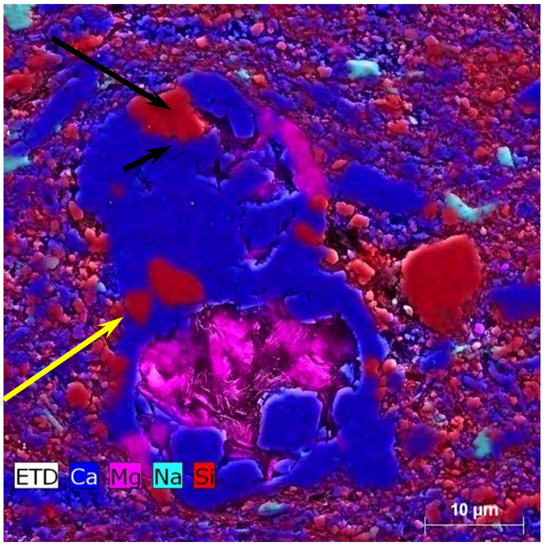

Figure 93: Authigenic microquartz (red) growing within a foraminifer shell is shown in the EDS X-ray map of the medium-maturity Well 3 sample 1-61 (2533.88m). Note that authigenic quartz indicated by black arrow is more likely to be secondary pore filling cement while the one indicated by yellow arrow may be a grain replacement.Small black arrow shows the pore space between nucleation surface and authigenic quartz.

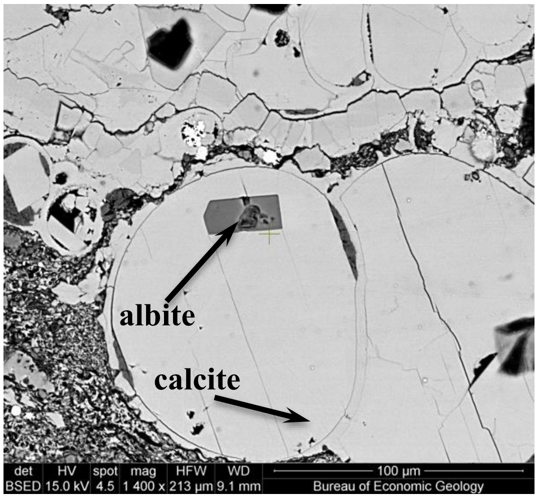

Figure 94: Albite replacement of calcite inside the foraminifer test is shown in the BSED of the low-maturity outcrop Well 1 sample 7 (133.71-133.68 m). Note that albite replacement is mostly observed in greater depths except for some low-maturity shallower Well 1 sample.

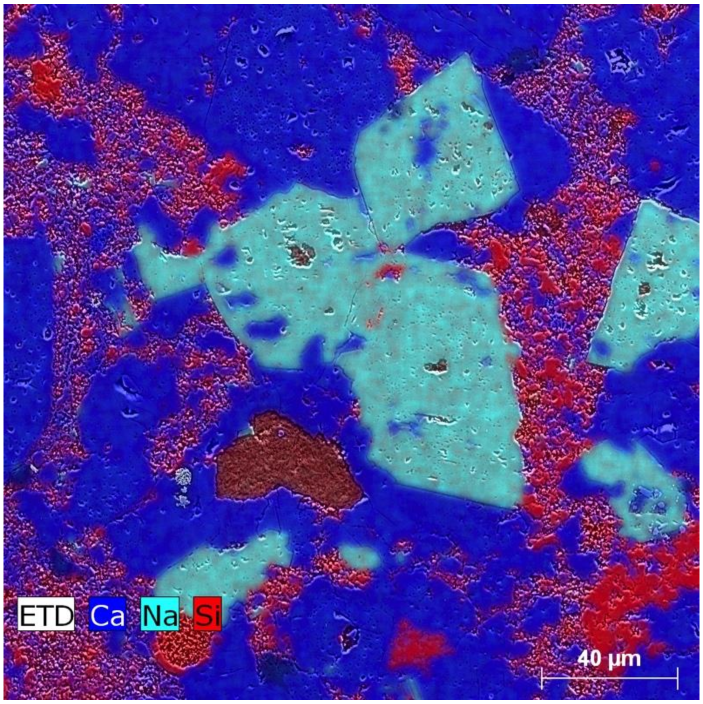

Figure 95: Albite replacement (aqua) of recrystallized calcite crystals (blue) during late diagenesis is shown EDS X-ray map of the high-maturity Well 3 sample 1-66 (2535.49m)

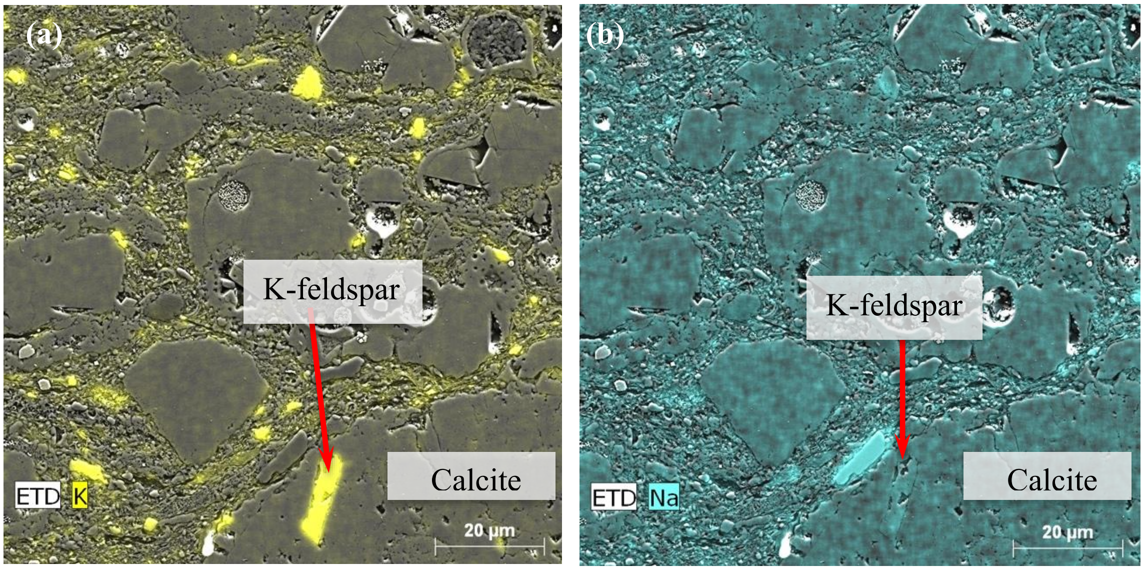

Figure 96: K-feldspar replacement? (a) is shown in the EDS X-ray map of the low-maturity outcrop Well 1 sample 23 (56.63-56.6m). Note that there is no albite identified in the crystal (b).

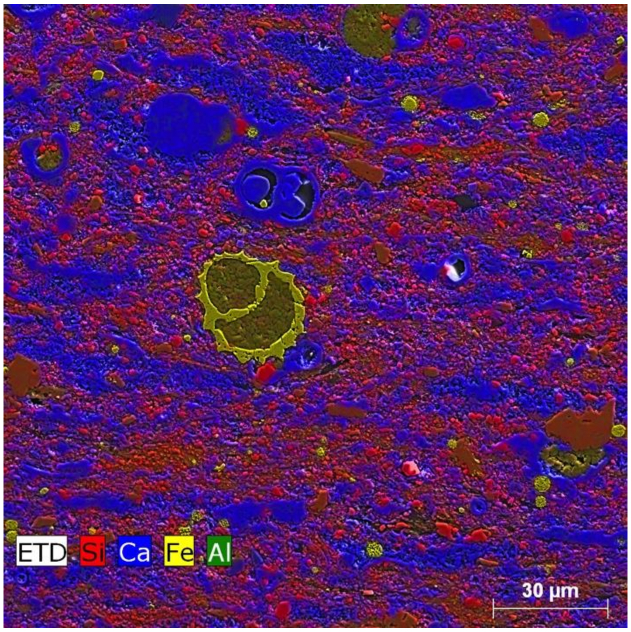

Figure 97: Complete pyritization of foraminifer shell (yellow) is shown in the EDS X-ray map of medium-maturity Well 2 CH5 sample (963.78m).

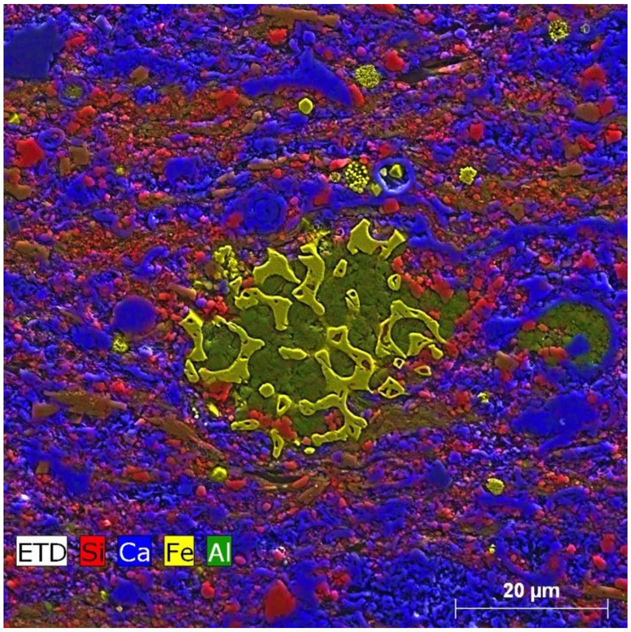

Figure 98: Complete pyritization (yellow) of partly preserved radiolaria is shown in the EDS X-ray map of medium-maturity Well 2 CH5 sample (963.78m). Quartz is red, calcite is blue; kaolinite is dark green.

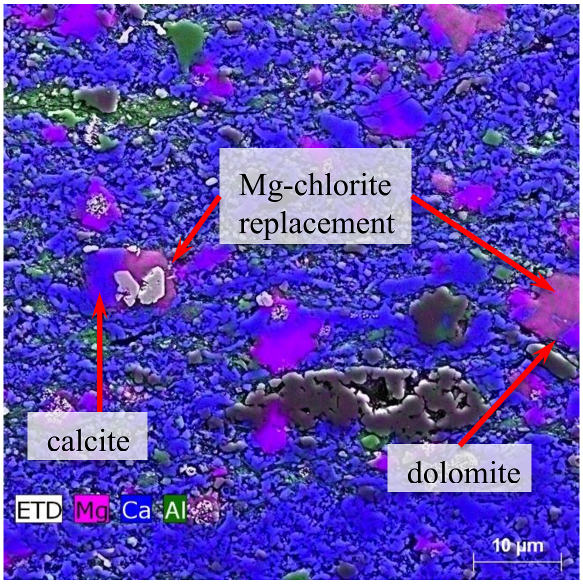

Figure 99: Mg-chlorite replacement of calcite/dolomite is shown in the EDS X-ray map of the high maturity Well 4 sample 1-100 (2803.99m). Note that dolomite is darker purple and Mg-chlorite is lighter purple.

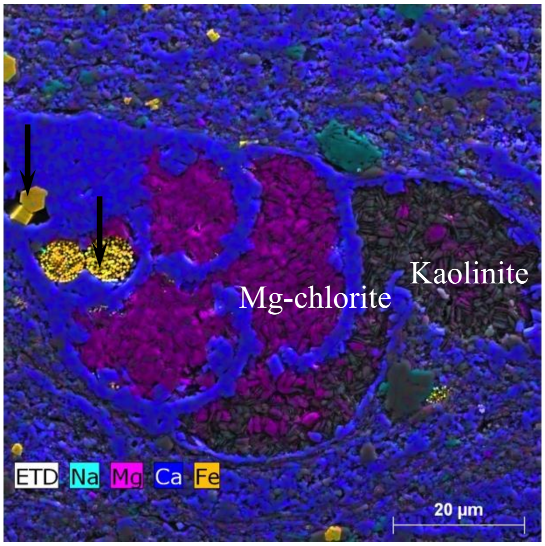

Figure 100: Mg-chlorite intergrowth or possible replacement (purple) kaolinite (gray) inside the chamber of foraminifer is shown in the EDS X-ray map of the high-maturity Well 4 sample 1-90 (2800.9m). Note that euhedral pyrite and framboidal pyrite are observed as cement (black arrows).

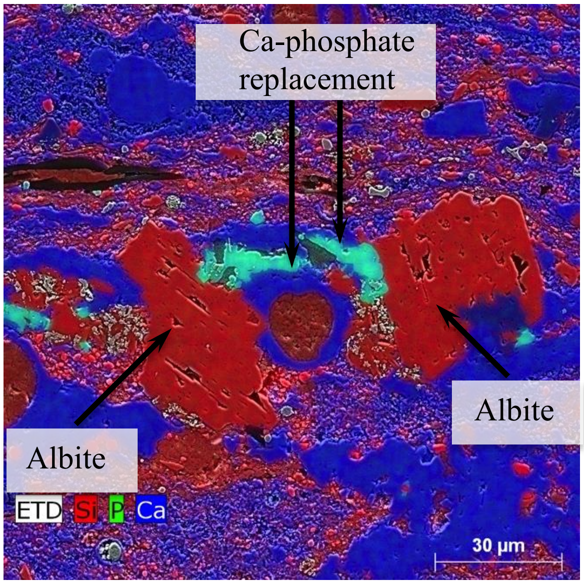

Figure 101: Ca-phosphate replacement (aqua) of both albite and calcareous allochem is shown in the EDS X-ray map of the medium-maturity well sample (973.26m). Note that it is not a Na map and albite is reddish because of its Si content, similar to the same quartz. Calcite is blue.

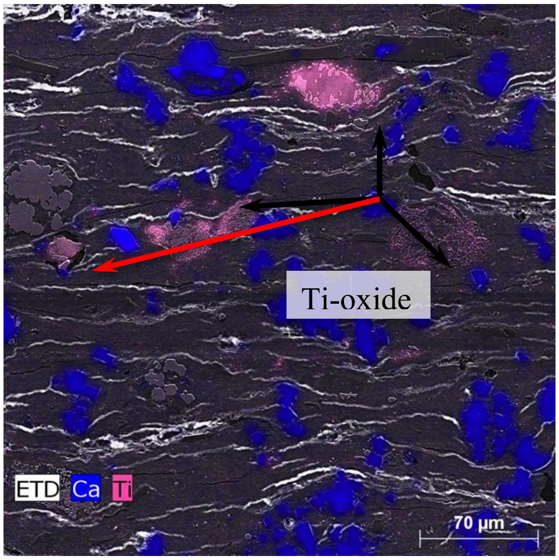

Figure 102: Titanium oxide, which is likely of detrital volcanic origin (black arrows), is shown in the EDS X-ray map of the medium-maturity Well 2 sample CH7 (973.26m). Note that the one indicated by red arrow is possibly authigenic origin.

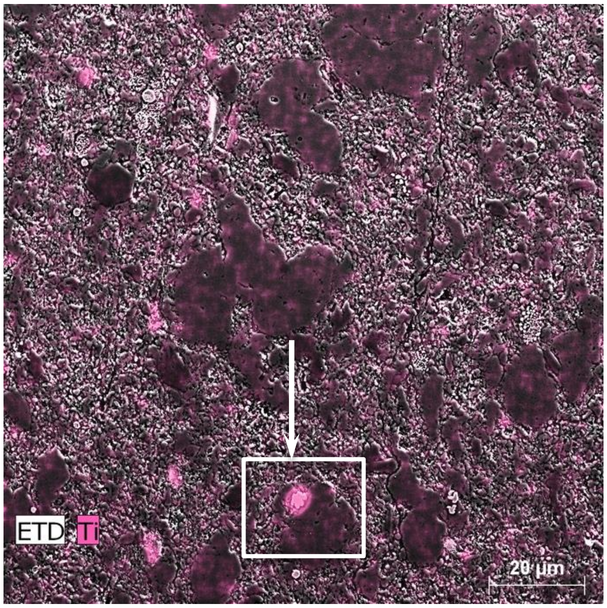

Figure 103: Replacement type authigenic titanium oxide, is shown in the EDS X-ray map of the high-maturity Well 4 sample 1-5 (2775.04 m).

Table 21: Grain replacement type authigenic minerals in the low-maturity outcrop well samples (Ro: 0.35-0.6%)

Sample NO	Depth (m)	Sulfides			Carbonates		Phosphate	Mg-chlorite	Authigenic Quartz	Feldspar		TiO2
		Pyrite		Sphalerite	Calcite	Dolomite				K-feldspar	Albite	
		Anhedral Pyrite (Mold)	Euhedral Pyrite									
23	56.63-56.6			🟥	🟥	🟥	🟥		🟥	🟥		
22	57.11-57.08		🟥									🟥
21	69.88-69.85				🟥	🟥	🟥					
20	79.68-79.65		🟥		🟥	🟥						
19	81.28-81.25											
18	88.93-88.8				🟥	🟥			🟥	🟥		
17	92.84-92.81				🟥	🟥						
16	98.11-98.08		🟥		🟥						🟥	
15	99.85-99.82		🟥		🟥	🟥				🟥		🟥
14	104.86-104.83					🟥						🟥
13	106.47-106.44		🟥			🟥						🟥
12	110.04-110.01	🟥										🟥
11	115.48-115.45	🟥				🟥			🟥			
10	122.94-122.91		🟥									🟥
8	128.91-128.88		🟥			🟥			🟥			
7	133.71-133.68		🟥			🟥			🟥		🟥	🟥
4	139.88-139.85		🟥			🟥			🟥			
2	149.52-149.49				🟥	🟥			🟥			
1	151.88-151.85		🟥						🟥			

Table 22: Grain replacement type authigenic minerals in medium-maturity well samples (Ro: 0.65-0.75 %)

Sample NO	Depth (m)	Depth (ft)	Sulfides		Carbonates		Phosphate	Mg-chlorite	Authigenic Quartz	Feldspar		TiO2
			Pyrite									
			Anhedral Pyrite (Mold)	Euhedral Pyrite	Calcite	Dolomite				K-feldspar	Albite	
CH1	911.28	2989.75		🟥	🟥	🟥			🟥		🟥	🟥
CH2	915.79	3004.55			🟥	🟥			🟥		🟥	🟥
CH3	950.24	3117.6		🟥		🟥	🟥		🟥		🟥	
CH4	953.22	3127.35			🟥	🟥			🟥		🟥	
CH5	963.78	3162	🟥	🟥		🟥	🟥		🟥		🟥	
CH6	969.95	3182.25		🟥		🟥	🟥		🟥		🟥	
CH7	973.26	3193.1	🟥	🟥	🟥	🟥	🟥		🟥		🟥	🟥

Table 23: Grain replacement type authigenic minerals in high-maturity well samples (Ro: 1.15-1.32%)

Sample NO	Depth (m)	Depth (ft)	Sulfides		Carbonates		Phosphate	Mg-chlorite	Authigenic Quartz	Feldspar		TiO2
			Pyrite									
			Anhedral Pyrite (Mold)	Euhedral Pyrite	Calcite	Dolomite				K-feldspar	Albite	
EF3 1-31	2524.77	8283.35				🟥					🟥	
EF3 1-61	2533.88	8313.25		🟥		🟥	🟥	🟥	🟥		🟥	🟥
EF3 1-66	2535.49	8318.55		🟥	🟥	🟥	🟥		🟥		🟥	🟥
EF3 1-136	2556.66	8388		🟥			🟥	🟥	🟥		🟥	

Table 24: Grain Replacement type authigenic minerals in high-maturity well samples (Ro: 1.16-1.31%)

Sample NO	Depth (m)	Depth (ft)	Sulfides		Carbonates		Phosphate	Mg-chlorite	Authigenic Quartz	Feldspar		TiO2
			Pyrite		Calcite	Dolomite						
			Anhedral Pyrite (Mold)	Euhedral Pyrite						K-feldspar	Albite	
EF4 1-5	2775.04	9104.45	🟥	🟥	🟥	🟥	🟥	🟥	🟥		🟥	🟥
EF4 1-10	2776.62	9109.65			🟥	🟥	🟥		🟥		🟥	
EF4 1-25	2781.10	9124.35		🟥	🟥	🟥	🟥		🟥		🟥	
EF4 1-35	2784.09	9134.15		🟥	🟥	🟥			🟥		🟥	
EF4	2787.70	9146		🟥	🟥	🟥	🟥		🟥		🟥	
EF4	2790.75	9156		🟥	🟥	🟥	🟥		🟥		🟥	🟥
EF4 1-75	2796.24	9174		🟥			🟥		🟥		🟥	🟥
EF4 1-80	2797.93	9179.55		🟥	🟥	🟥	🟥		🟥		🟥	🟥
EF4 1-90	2800.90	9189.3	🟥	🟥	🟥		🟥	🟥	🟥		🟥	
EF4 1-100	2803.99	9199.45		🟥	🟥	🟥	🟥	🟥	🟥		🟥	
EF4 1-123	2811.06	9222.65	🟥	🟥			🟥	🟥	🟥		🟥	🟥

OTHERS

In this study, most authigenic minerals fall clearly into the categories of cement or grain replacement. A few occurrences of obviously authigenic minerals cannot be clearly assigned to one of these categories: displacive cement (cone-in-cone fabric) and fracture filling are special cases of authigenic minerals reported in this section.

Precipitation of authigenic gypsum is widespread on the surfaces of organic-rich black shales where sulfides are oxidized in the presence of carbonate rich rocks (Bain, 1990). In the study of Bain (1990), growth of gypsum is mostly considered as displacive and it is stated that, soft and water-rich muds are displaced during growth of gypsum, which is the explanation for the gypsum precipitation mostly observed in the outcrops of the Eagle Ford. Gypsum is the most common fracture filling authigenic component in the Eagle Ford (Figure 104). It is also identified in the Eagle Ford in previous studies (Dawson, 2000; Fairbanks, 2012; Jennings and Antia, 2013). Fracture filling gypsum is identified in the Lozier Canyon and Comstock outcrop samples and in the uppermost part of the UEF samples of the low-maturity outcrop Well 1 samples. Gypsum is also observed as a pore filling in a few samples of the Eagle Ford. In pyrite-rich mudstones the reactions of oxidation of framboidal pyrite, leaching of carbonates by sulphuric acid and authigenic gypsum generation is widespread (Bain, 1990; Blowes and Jambor, 1990; Pye and Miller, 1990; McGregor and Blowes, 2002). Gypsum precipitation in the mudrocks can cause serious fabric disruption in cores because of displacive growth (Pye and Miller, 1990).

Displacive calcite/dolomite also cannot be included in either grain replacement or cement type authigenics. Diagenetic fibrous calcite veins are firstly recognized by Sorby (1860) and named as cone-in-cone structure (Marshall, 1982, Cobbold et. al., 2013). The radiating displacive nature from a central vertical zone, tree-like appearance, fibrous dolomite growing perpendicular to bedding and orientation in one direction (Marshall, 1982; Lu et. al., 2011; Cobbold et. al., 2013) are used to describe the fabric as cone-in cone in the medium-maturity Well 3 sample 7 of the Eagle Ford. Displacive dolomite growth in this sample, which is similar to calcite identified in the previous studies, causes the generation of some microfractures perpendicular to the growing direction of displacive calcite within the authigenic clay (Figure 107). Interpreted image based on photomicrograph shows the abundance of displacive dolomites growing within the very fine-grained clay matrix and some other components including quartz, albite, pyrite and rarely calcite (Figure 108). Displaced background clay is different from the general view of clay-rich dark colored foraminifer-bearing layer of the sample and the boundary between them can be seen easily (Figure 105, Figure 106). There are both early (Martill, 1987) and late interpretations (Marshall, 1982) about origin of cone-in-cone fabric; however, it is mainly associated with OM-rich mudrocks no matter what the timing (Cobbold et. al., 2013).

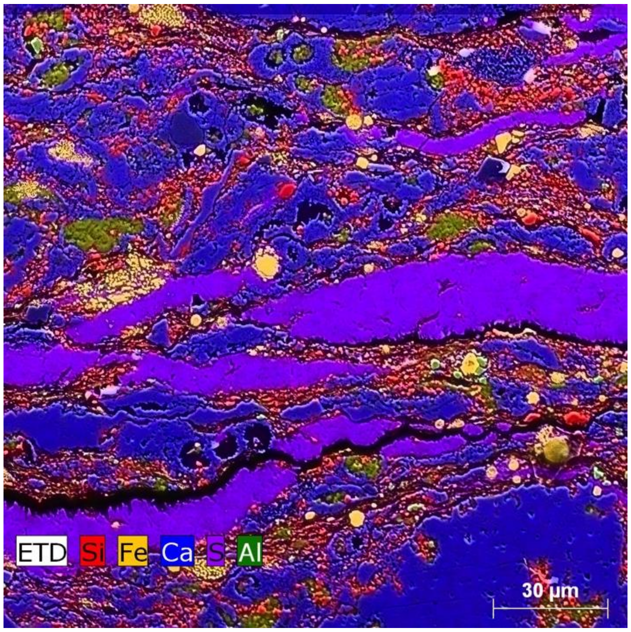

Figure 104: Gypsum vein (purple) as a fracture filling authigenic component is shown in the EDS X-ray map of the outcrop Lozier Canyon LZ-3 sample

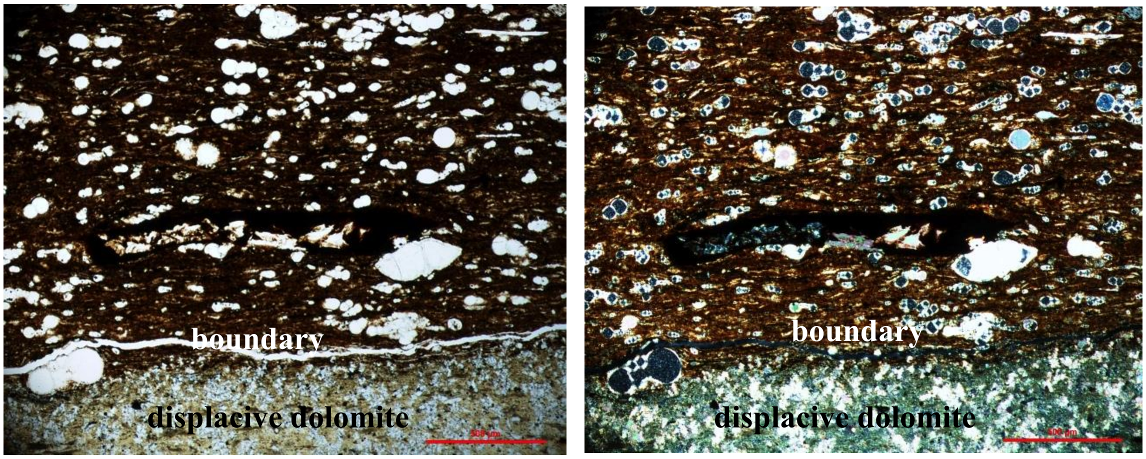

Figure 105: Boundary between general view of clay-rich foraminifer bearing mudrock (named as marl in the classification) and volcanic ash related authigenic clay and displacive dolomite precipitation is shown in transmitted (a) plane-polarized (b) cross-polarized light image of the medium-maturity Well 2 sample 7 (973.26m).

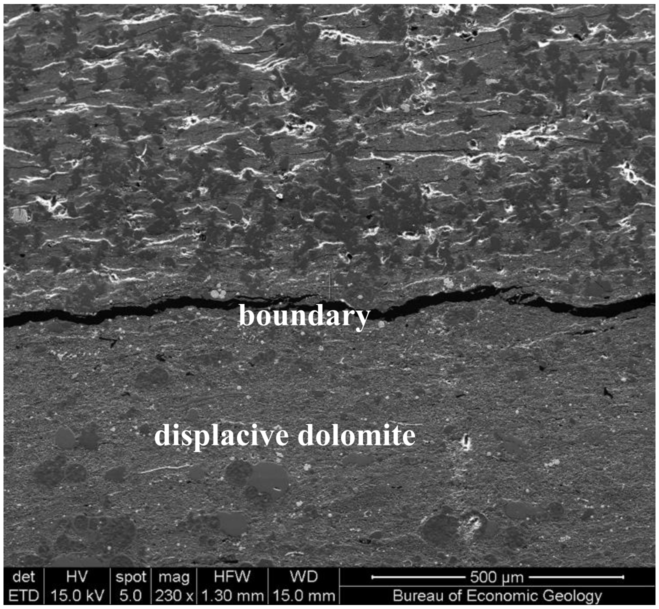

Figure 106: Boundary between general view of clay-rich foraminifer bearing mudrock (named as marl in the classification) and volcanic ash related authigenic clay and displacive dolomite precipitation is shown in the SEM image of the medium-maturity Well 2 sample 7 (973.26 m).

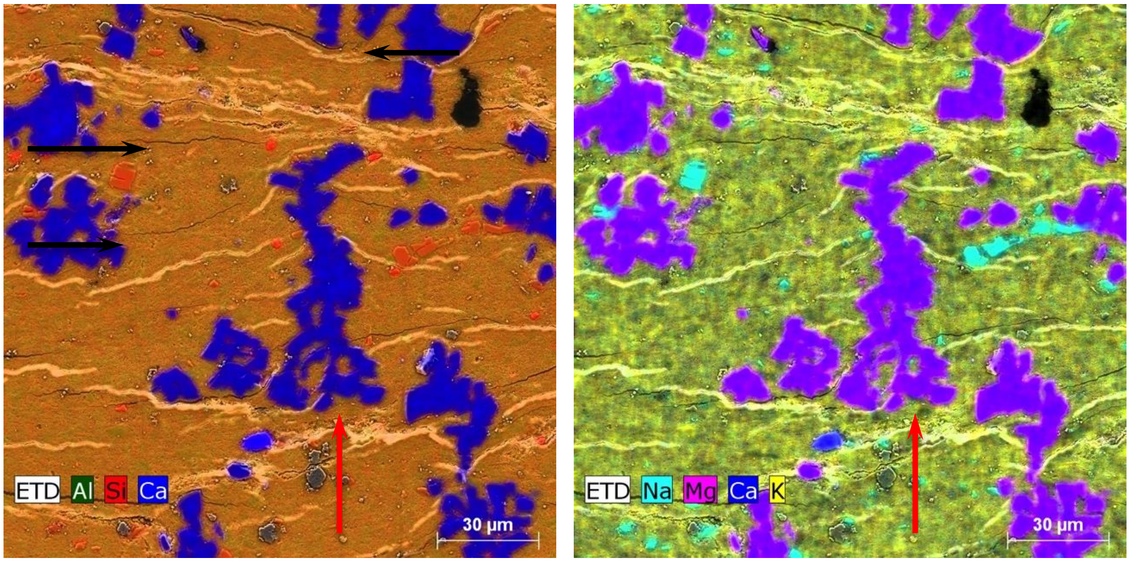

Figure 107: Cone-in-cone fabric is shown as displacive fibrous dolomite veins and very fine-grained clay matrix are shown in the different composional EDS X-ray maps of the medium-maturity Well 3 sample 7 (973.26 m). Note that black arrows show the microfractures generated due to cone-in-cone fabric and red arrow is the growing direction of cone-in-cone.

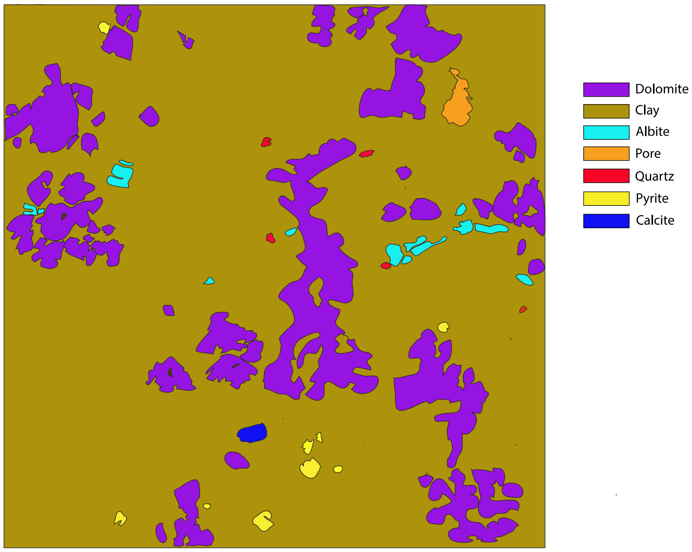

Figure 108: Interpreted image based on photomicrograph shows cone-in-cone fabric. Dolomite (purple) is growing through mainly one direction in very fine-grained clay matrix (light brown) (potentially volcanic ash).

Table 25: Other type of authigenic components in the low-maturity outcrop well samples (Ro: 0.35-0.6%)

Sample NO	Depth (m)	Displacive Authigenics	
		Calcite	Gypsum
23	56.63-56.6	🟨	🟨
22	57.11-57.08	🟨	🟨
21	69.88-69.85		
20	79.68-79.65	🟨	🟨
19	81.28-81.25		
18	88.93-88.8	🟨	
17	92.84-92.81		
16	98.11-98.08		🟨
15	99.85-99.82		
14	104.86-104.83		
13	106.47-106.44		
12	110.04-110.01		
11	115.48-115.45		
10	122.94-122.91		
8	128.91-128.88		
7	133.71-133.68		
4	139.88-139.85		
2	149.52-149.49		
1	151.88-151.85		

Table 26: Other type of authigenic components in the medium-maturity well samples (Ro: 0.65-0.75 %).

Sample NO	Depth (m)	Depth (ft)	Displacive Authigenics	
			Calcite	Gypsum
CH1	911.28	2989.75		
CH2	915.79	3004.55		
CH3	950.24	3117.6	🟨	
CH4	953.22	3127.35		
CH5	963.78	3162		
CH6	969.95	3182.25		
CH7	973.26	3193.1	🟨	🟨

Table 27: Other type of authigenic components in the high-maturity well samples (Ro: 1.15-1.32%)

Sample NO	Depth (m)	Depth (ft)	Displacive Authigenics	
			Calcite	Gypsum
EF3 1-31	2524.77	8283.35		
EF3 1-61	2533.88	8313.25	🟨	
EF3 1-66	2535.49	8318.55		
EF3 1-136	2556.66	8388	🟨	

Table 28: Other type of authigenic components in the high-maturity well samples (Ro: 1.16-1.31%)

Sample NO	Depth (m)	Depth (ft)	Displacive Authigenics	
			Calcite	Gypsum
EF4 1-5	2775.04	9104.45	🟨	
EF4 1-10	2776.62	9109.65		
EF4 1-25	2781.10	9124.35		
EF4 1-35	2784.09	9134.15		
EF4	2787.70	9146	🟨	
EF4	2790.75	9156		
EF4 1-75	2796.24	9174		
EF4 1-80	2797.93	9179.55		
EF4 1-90	2800.90	9189.3	🟨	
EF4 1-100	2803.99	9199.45		
EF4 1-123	2811.06	9222.65		

Paragenesis

Based on petrographic observations including conventional light microscope, FE-SEM, EDS X-ray mapping, and cathodoluminescence imaging, authigenic components are interpreted to have formed across a range thermal maturity (Figure 110). There is no pronounced contrast between the diagenetic features and paragenetic sequences observed in the UEF and LEF. Open chambers of calcareous foraminifer tests show that these intraparticle pore space filling cement type authigenic minerals are considered as product of early diagenesis before they undergo to compaction (Fishman et. al., 2013) and they prevent compaction. If some pores survived this early process, they can be filled later and potentially become host for later cements. In order to have an idea about the relative timing of diagenetic features, foraminifer tests, where authigenic phases are seen together, are good place to begin. The relative timing of authigenic minerals is mostly determined from observations of the crystals within the anomalously large pores within calcareous foraminifer tests. The problem with the grain replacements is that telling the timing is inherently difficult because of the absence of cross-cutting relationships or cement stratigraphy, which are used as clues for the paragenesis. The next evidence is the occurrence across thermal maturity where some authigenic components and other diagenetic features are more abundant at higher temperature and mineral transformations are more easily observed. Most of the authigenic phases start to precipitate early; however, they become more abundant during later diagenesis. Paragenesis section is going to be assessed in two separate sections including early and late diagenesis depend on the observations of diagenetic features and processes at different maturity levels. Generally speaking, diagenetic features and processes observed in the low maturity are mostly considered as early and the ones, which become more abundant in the medium maturity and high maturities, are evaluated as late diagenesis.

EARLY DIAGENESIS

The most common early diagenetic components are calcite, pyrite, kaolinite, bitumen, and dolomite in the Eagle Ford. Assessment of petrographic studies reveals that euhedral nature of calcite and growth of replacive patchy kaolinite through it (Figure 112) argues that calcite came first. In some of the chambers however, no kaolinite is detected which supports the idea that kaolinite came first with a patchy distribution and the calcite came later and filled whatever space was left. Although there is not enough evidence to fully document the relative timing of calcite and kaolinite, calcite is assessed as slightly earlier than kaolinite in the paragenetic sequence. Another early diagenetic product, pyrite is syndepositional with precipitation starting at the time of deposition and continuing (Figure 110). Dolomite is also early but relatively later than calcite and kaolinite in the diagenetic history (Figure 113 and Figure 114), which is observed as direct precipitation from the solution and mostly a replacement of calcite.

LATE DIAGENESIS

Following the early-formed diagenetic minerals, quartz, apatite (phosphate), albite and Mg-chlorite precipitation and K-feldspar dissolution are observed during the later diagenesis (Figure 110). Authigenic quartz formation is first observed in the low-maturity outcrop Well 1 samples whereas it becomes more pervasive through the samples in the medium-maturity and high-maturity wells (especially as a cement) (Figure 79). Although it is known that precipitation of quartz begins early, crosscutting relationship with Mg-chlorite (a late-diagenesis product) (Figure 115) reveals that it continues and become more abundant during late diagenesis. Phosphate precipitation is dominantly observed in the high-maturity samples however; in some UEF samples of Well 1, replacement type apatite is also observed.

Feldspar behavior in the Eagle Ford mudrock during burial is similar to sandstones. In the low maturity outcrop Well 1 samples, K-feldspar is identified using petrographic analysis, which is also supported with the XRD results (Table 2). Absence of K-feldspar in the medium and high-maturity well samples with the increasing depth and increase in the abundance of the albite are expected trends in higher temperature diagenesis. It can be explained with the K-feldspar dissolution and albite and calcite replacement in the low-maturity outcrop Well 1 samples during later burial diagenesis, which is commonly observed in mudrocks (Milliken, 1992). In the study of Milliken (1992), it is stated that the dissolved K-feldspar is dominantly Na-rich feldspars, which are unstable compared to K-rich K-feldspars. It allows having abundant albite precipitation subsequently to the Na-rich K-feldspar dissolution. Mg-chlorite is mostly observed intergrown with kaolinite, which can be interpreted as simultaneous precipitation; however, since it is known that kaolinite precipitates in very early diagenesis whereas Mg-chlorite is coming late (starts to be seen in high-maturity samples), it is possible that the Mg-chlorite is a partial or complete replacement of kaolinite. It is easier to determine if Mg-chlorite replaces dolomite/calcite whereas identification within the pore space whether it is cement or replacement is more controversial.

The early-formed authigenic minerals including calcite, dolomite, and pyrite are also observed as a second phase during the late-diagenesis (Figure 110). Late calcite precipitation is observed as a recrystallization of the calcareous allochems including pellets and foraminifers. Dolomite is also precipitated during late diagenesis (Figure 113(b)) as a replacement of a second phase of recrystallized calcite or it can still be early replacement of early calcite (Figure 113(a)). Pyrite precipitation occurs in two distinct morphologies in mudrocks including framboidal pyrite and euhedral pyrite (Taylor and Macquaker, 2000). These different morphologies are formed during early diagenesis and related to sulfide production rates and amount and reactivity of organic matter (Taylor and Macquaker, 2000). Pyrite precipitation of late diagenetic origin is, observed in the Eagle Ford as replacement of foraminifer tests and cortical shell of the radiolarian, and is only found in the medium-maturity and high-maturity wells.

Organic matter evolution starts early in the diagenesis, continues in catagenesis and ends in metagenesis (Dow, 1977; Vandenbroucke and Largeau, 2007; Jennings and Antia, 2013). During diagenesis microbial activity is one of the significant processes of organic matter evolution (Tissot and Welte, 1984). Ro values of various samples at the different maturity levels (Ro 1.3 to 1.4) identified by Zhang (2014) can mostly be considered as catagenesis as defined by Tissot and Welte (1984) (Figure 109). These terms such as catagenesis is not used in this study since they are poorly defined and impossible to assign with certainty. These processes are extremely significant for the final composition and changes in the sulfur and oxygen contents of kerogen (Vandenbroucke and Largeau, 2007). Definition of organic matter varies for the chemical purposes and petrographical purposes. In chemical point of view, kerogen is the insoluble in aqueous alkaline solvents and common organic solvents whereas bitumen is soluble (Tissot and Welte, 1984). On the other hand, kerogen has an aspect of detrital origin (extrabasinal to intrabasinal) associated with particulate type organic matter while bitumen is formed during kerogen maturation with the hydrocarbon release into pores (diagenetic) (Milliken et. al., 2013).

Diagenesis stage during the organic matter maturation includes the biochemical and chemical break down the organic matter (Jennings and Antia, 2013). Two different types of bitumen are identified in the Eagle Ford. The early-formed migrated bitumen precipitated within the intraparticle and interparticle pore spaces in the low-maturity Well 1 samples. The late-formed bitumen is associated with the organic-hosted pore development. As explained earlier, organic matter hosted pores can be primary or secondary which are formed during diagenesis (Milliken et. al, 2013). Secondary pores are identified even in the medium-maturity Well 2 (Pommer, 2014). The secondary pore generation coincides with the commencement of wet-gas generation and bitumen migration during catagenesis (Fishman et. al., 2013; Jennings and Antia, 2013). The boundary between oil and gas window can be considered where organic matter hosted pores start to develop with the bitumen migration. Metagenesis includes dry gas generation stage during late-burial diagenesis. Timing of organic pore development is defined as late catagenesis due to pore abundance and pore connectivity during this period (Jennings and Antia, 2013). Organic acid generation is resulted in pore water chemistry changes and it has significant impact on the stability of carbonates and silicates (dissolution and cementation) (Curtis, 1983; Wust et. al., 2013) and Al mobility for the kaolinite precipitation (Curtis, 1983) in terms of authigenic mineral precipitation during the burial diagenesis. Organic matter acid generation can have a contribution on the intraparticle pore development due to dissolution of kerogen during burial (Loucks et. al, 2012).

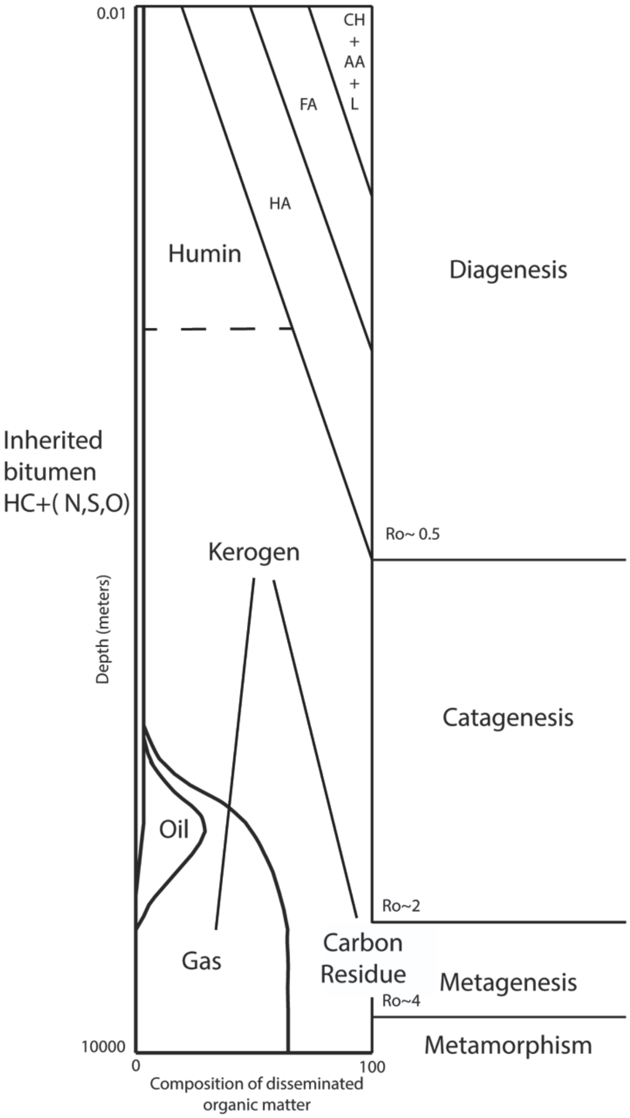

Figure 109: Evolution of organic matter starts from at the time of deposition and continues through metamorphism. CH: carbohydrates, AA: amino acids, FA: fulvic acids, HA: humic acids, L: lipids, HC: hydrocarbons, N, S, O compounds: non-hydrocarbons (Tissot and Welte, 1984). Note that approximate thermal maturity levels (Ro), oil and gas windows can be seen.

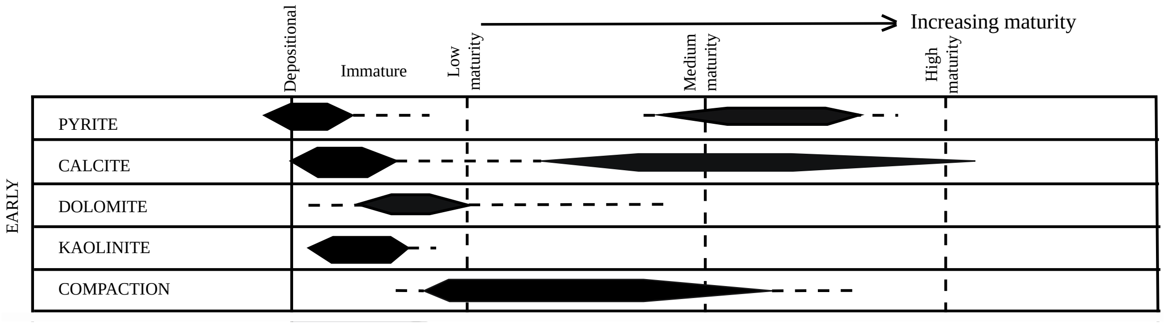

Figure 110: Early paragenetic sequence of diagenetic events and formation of authigenic minerals at different maturity levels

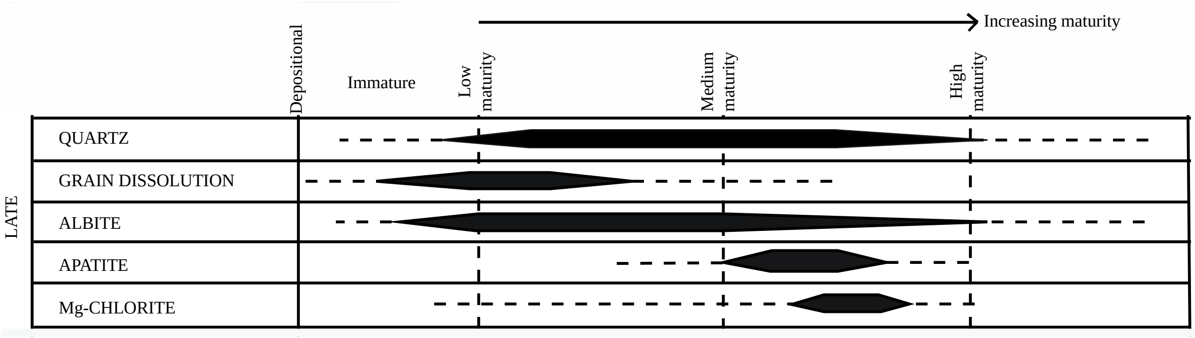

Figure 111: Late paragenetic sequence of diagenetic events and formation of authigenic minerals at different maturity levels

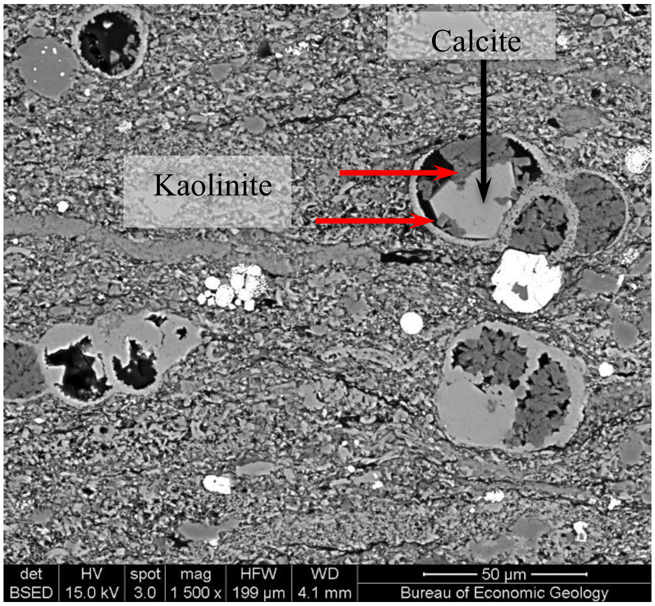

Figure 112: Kaolinite replacement (red arrows) of euhedral calcite crystal inside the foraminifer chamber is shown in the BSED image of the outcrop Lozier Canyon LZ-7 sample

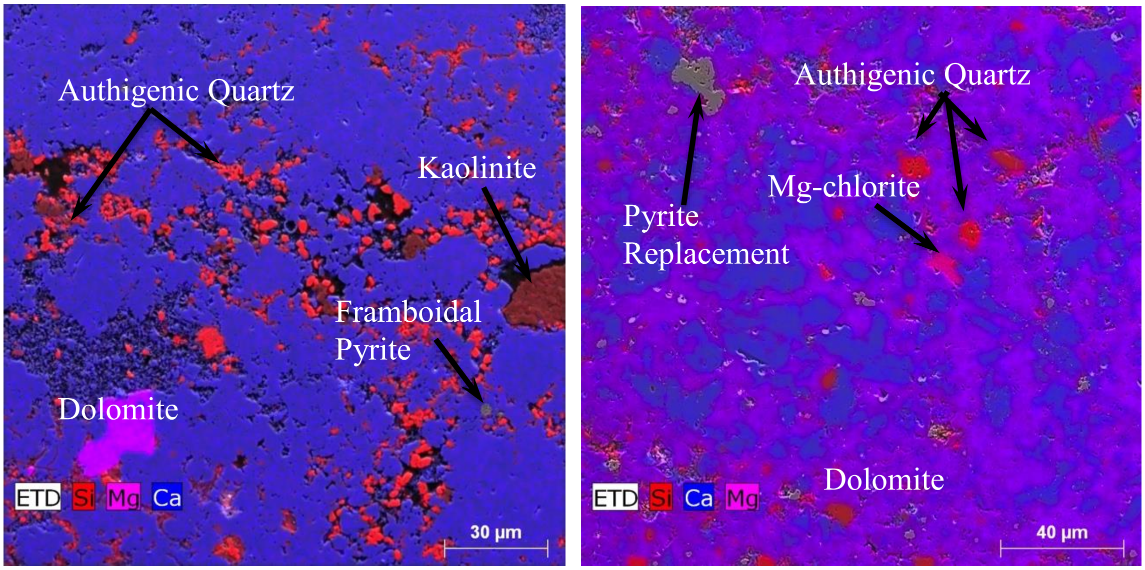

Figure 113: Dolomitization is shown in the EDS X-ray maps of the (a) low-maturity outcrop Well 1 sample (149.52-149.49m) (b) high-maturity B 1HB sample (deepest sample) (2966.01m). Note that some different authigenic minerals precipitated in low-maturity and high-maturity well samples are labeled.

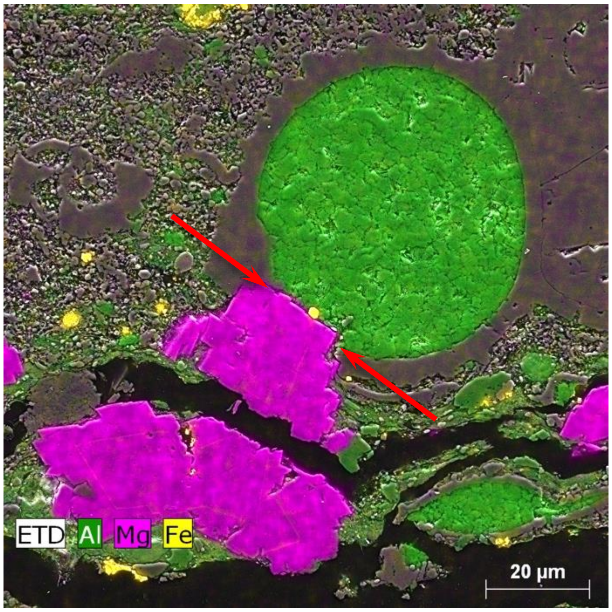

Figure 114: Dolomite replacement of kaolinite is shown in the EDS X-ray maps of the medium-maturity Well 2 sample CH7 (973.26m)

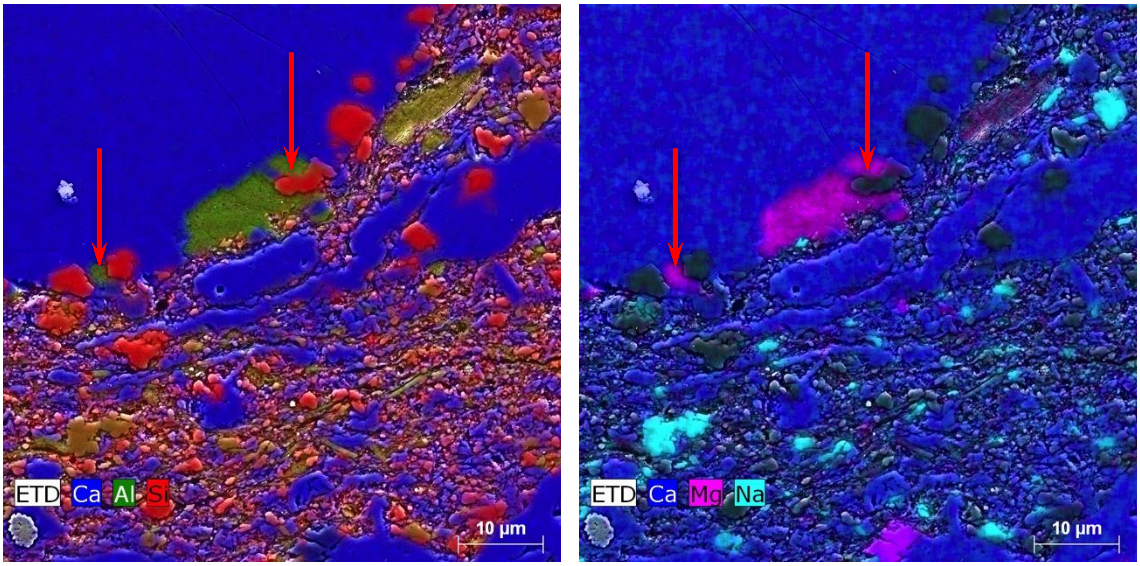

Figure 115: Quartz replacement (red arrows) of Mg-chlorite at the edge of the foraminifer shell is shown in the EDS X-ray maps of the high-maturity Well 3 sample 1-61 (2533.88m). Note that on left red arrow euhedral shape of quartz growing through Mg-chlorite and crosscutting relationship between quartz and Mg-chlorite are observed.

DISCUSSION

Diagenetic Trends Across Thermal Maturity and The Correlation Between Grain Composition and Diagenesis

Combination of dominantly qualitative analysis using various petrographic techniques and quantitative analysis by point counting reveals the general lithological character of the Eagle Ford. Classification based on the detrital assemblage and authigenic components formed as a result of various diagenetic processes across thermal maturity levels are assessed to make correlation (Table 10, Table 11, Table 12, and Table 13). Bulk data is plotted on the ternary diagram to see calcareous nature of the Eagle Ford samples (Figure 116). Relative percentages of authigenic components are calculated using point count results and bulk data analysis as explained earlier; however because point count results are the reflection of approximate percentages of detrital components, the method used for the calculation of relative percentages of authigenics do not work for each component. For instance, it worked well for the calculation of authigenic quartz and give an idea about the how abundant the authigenic quartz is in high-maturity wells compared to low-maturity well (further below), whereas it is difficult to apply to the percentages of authigenic feldspar including both K-feldspar and albite. It can be explained by the insensitivity of bulk data analysis to feldspar because since bulk data measures the total feldspar included in both feldspars and lithics, which makes feldspar amount measured in the bulk data analysis overestimated relative to monocrystalline feldspars observed petrographically.

One of the main point in this study is the ways in which alteration of the detrital assemblage including dissolution of volcanic glass, feldspars and radiolarian led to precipitation of authigenic phases such as kaolinite, quartz and feldspar. Grain dissolution is involved in late diagenesis part since it becomes more widespread with increasing maturity although it is believed to start earlier in the diagenetic history. Petrographic observations which can record the decrease in K-feldspar amount and increase in the albite amount with increasing depth and maturity and quartz amount which is also recorded in the point count results suggest these alterations. However, the mass balance between the detrital components and authigenic components are still uncertain due to the challenges to determine the portions of variable sources have a contribution on the precipitation of authigenic minerals. For instance; authigenic quartz can be precipitated as a result of the dissolution of other reactive silica bearing minerals as well as biosiliceous grains.

Quartz percentages obtained from point count results and XRD results are compared for both medium-maturity and high-maturity well samples (Figure 118, Figure 119, Figure 120). Because XRD results reflect the bulk composition of the samples including both detrital grain and authigenic components, and point count results are the only quantitative representation of detrital quartz percentages, the difference between them gives the authigenic quartz percentages in the samples. According to these observations and calculations, although authigenic quartz amount is similar in medium and high-maturity well samples, bulk quartz thereby detrital quartz percentages are abundant in high-maturity compared to medium-maturity. Majority of quartz is authigenic in medium-maturity Well 2 samples. Most mudstones are deposited along basin margins. Where there is a pronounced terrigenous siliciclastic deposition, the source of the quartz silt will not be biogenic silica. Proximity to the source area is related to the amount of terrigeneous and volcanic grains. Quartz silt abundance is a useful indicator of shoreline proximity (Blatt, 1985). Biogenic sedimentation is more important in distal mudstones due to their slow accumulation rate and biogenic silica can be considered as a source of in-situ quartz silt (Schieber et. al., 2000). Because siliciclastic influx is restricted during the Eagle Ford deposition in the South Texas area, it can be interpreted that majority of the quartz is derived from the biogenic sedimentation. Another explanation for quartz precipitation can be clay diagenesis, which is not the case in the Eagle Ford due to unsystematic changes in authigenic quartz and clay percentages (Figure 125). The discrete outline of the detrital quartz is one of the significant criteria to differentiate it from the blobby shape of authigenic quartz, which is mostly dispersed in the matrix. CL was applied to some samples in order to reveal the existence of authigenic quartz, however applying CL on each sample was not possible in Eagle Ford due to the abundance of massively calcitized samples.

According to Isaacs (1982) detrital composition and relative proportions of silica have a significant influence on the kinetics of silica phase changes. If the rocks are composed of abundant detrital minerals compared to silica, quartz formation is observed earlier than the rocks with minor detrital component. Carbonate composition does not have any direct effect on the kinetics of silica phase change except for the relative abundance of silica is much more than detrital components (Isaacs, 1982). Because silica is not especially abundant in the Eagle Ford, carbonate composition does not significantly affect the silica diagenesis in the Eagle Ford. Also, silica diagenesis can be considered as earlier in the Eagle Ford, which can be explained by the abundance of detrital components and minor silica content consistent with the model proposed by Isaacs

(1982). Authigenic quartz precipitation can be considered as a common phenomenon in all wells; however, in the upper part of the low maturity outcrop well (Figure 117) it is not as abundant as in the medium maturity and high maturity (Figure 118, Figure 119, and Figure 120). In LEF part of the shallower well (low maturity outcrop well), although detrital quartz percentage does not increase, total quartz and thereby authigenic quartz percentage increases (Figure 117). It can be inferred that abundance of authigenic quartz precipitation increases with stratigraphic depth; yet after this depth it does not vary with increasing stratigraphic depth. In both the argillaceous marl of the low maturity outcrop Well 1 (Figure 117) and marl in the medium maturity Well 2 (Figure 118) and high maturity Well 3&4 (Figure 119 and Figure 120), abundance of authigenic quartz suggest that silica diagenesis does not affected by the carbonate composition.

In the calcareous tarl and argillaceous marl, calcite is mostly observed as cement instead of grain replacement. Calcite is both cement and grain replacement in marls including all medium and high-maturity well samples and majority of UEF samples of Well 1 (Figure 131). Euhedral shape of calcite identified mostly in marls and recrystallization observed in the replaced facies (calcite replacement of radiolaria (above) are mostly considered as distinctive character of calcite replacement.

In order to provide parallel data with the point count, only quartz, feldspar including both K-feldspar and plagioclase and clay percentages are used to calculate bulk terrigeneous and volcanic grain percentages in the XRD data. They summed up with calcareous allochems and normalized. Point count and XRD results of terrigeneous and volcanic grains are compared and it is obviously observed that detrital calcareous allochems are overestimated and terrigeneous and volcanic grains are underestimated in the point count analysis (Figure 122, Figure 123, and Figure 124). For the low maturity outcrop well show increase in the terrigeneous and volcanic grains with the stratigraphic depth trend (especially in LEF part of the low maturity well samples) is consistent in the both point count data and XRD data (Figure 53 and Figure 121). Overestimation of calcareous allochems is not obviously observed as medium maturity and high maturity well samples, since authigenic carbonate precipitation in the low maturity well is not as much as in the medium maturity and high maturity well. Bulk data percentages are supposed to be higher than point count results for both terrigeneous and volcanic grains and calcareous allochems; however because their total is 100%, if one of them is overestimated, other one should be underestimated reported here. The reason why they are more than total carbonate percentages is the challenge to determine whether the fine-grained calcareous allochems in the matrix is authigenic or detrital. Therefore, if calcareous allochems are ignored and only terrigeneous and volcanic grain percentages across thermal maturity levels are considered, it can be inferred that where detrital percentages increase, total percentages (detrital and authigenic phases) increases and vice versa, which supports the idea that abundance of detrital grains have an important influence on the abundance of authigenic phase. Detrital and total percentages do not increase or decrease in the same amount, yet their change is systematic. Also, calcareous allochems are more overestimated in the high-maturity Well 4, which can be explained by the abundant authigenic fine-grained carbonate in the matrix. Where the calcareous allochem percentages get higher, authigenic terrigeneous and calcareous allochems decreases (detrital and bulk data get closer) (Figure 122 and Figure 123).

The porosity and permeability data of medium maturity Well 2 samples, high maturity Well 3&4 samples provided by Shell are plotted to observe the change in reservoir properties with depth respectively (Figure 126 and Figure 127). Due to the absence of consistency of the data in medium maturity and high maturity wells, they could not be plotted on the same graph. Increasing trend of the medium maturity Well 2 samples are obviously observed and lowest permeability and porosity value of sample CH4 correspond to highest COPL values calculated (Table 14) and highest permeability and porosity values of the sample CH5 correspond to lowest COPL values (Table 14). In the high maturity wells plot, consistency of low permeability and approximately similar porosity values of the samples are realized except for one highly permeable Well 4 sample 1-80 (2797.93m) sample and highly porous Well 3 sample 1-136 (2556.66m). Petrographic analysis supports the observation of porosity versus permeability graph with the abundance of interparticle secondary porosity (Figure 128) in the matrix (sometimes oversize-pores) (Figure 129). In the other outlier sample in which porosity is higher when compared with the sample Well 3 sample 1-66 which has approximately same permeability value, petrographic data reveals isolated intraparticle porosity abundance (Figure 130).

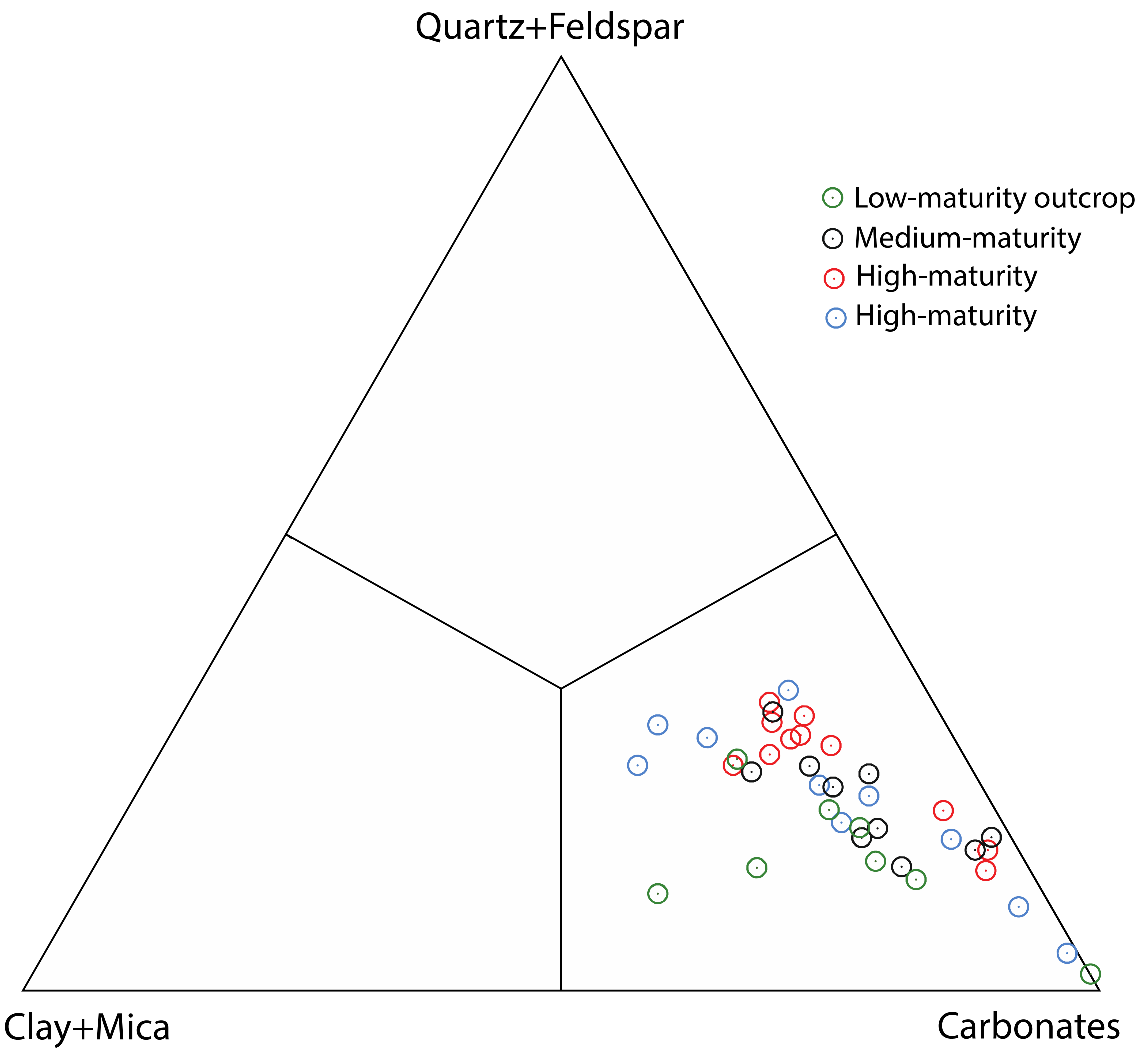

Figure 116: Plotted bulk data on the ternary diagram whose vertices correspond to main components in the Eagle Ford of low maturity, medium maturity and high maturity samples

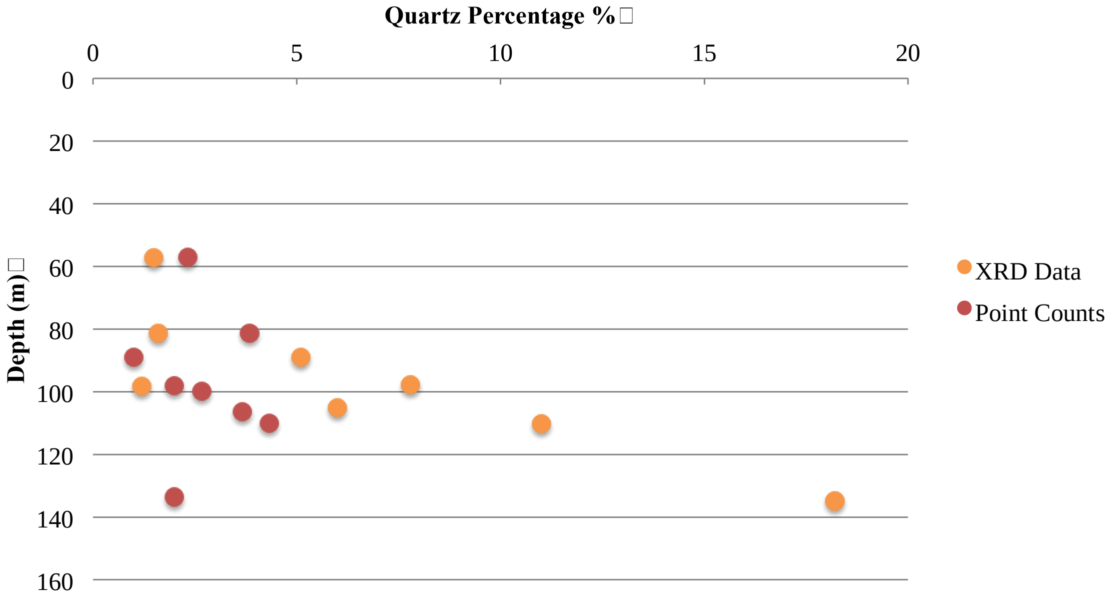

Figure 117: Quartz percentage vs. depth graph of low maturity outcrop Well 1 samples

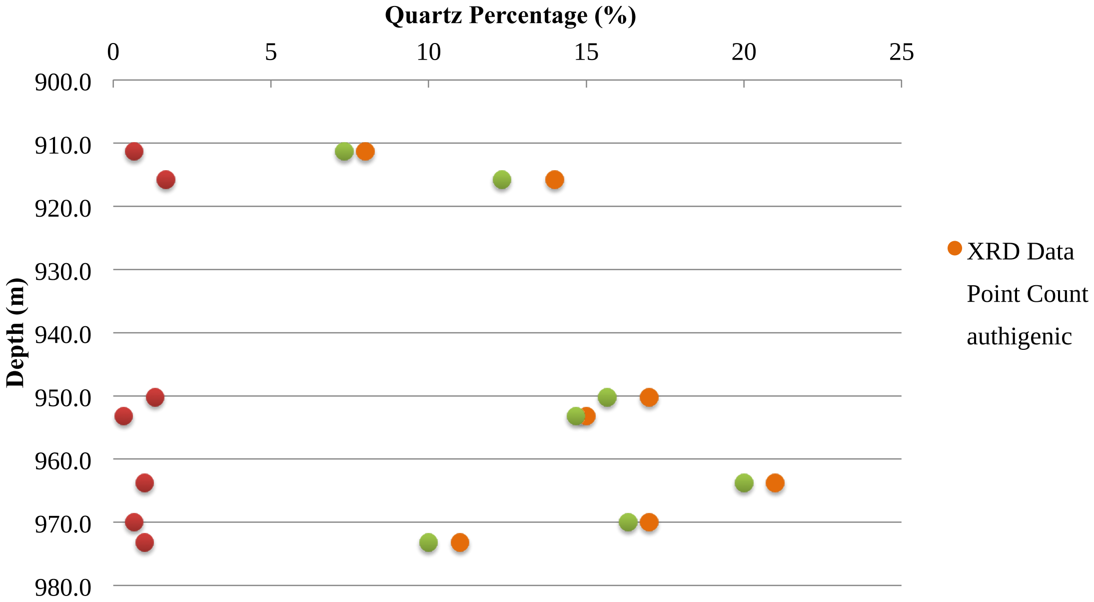

Figure 118: Quartz percentage vs. depth graph of medium-maturity Well 2 samples

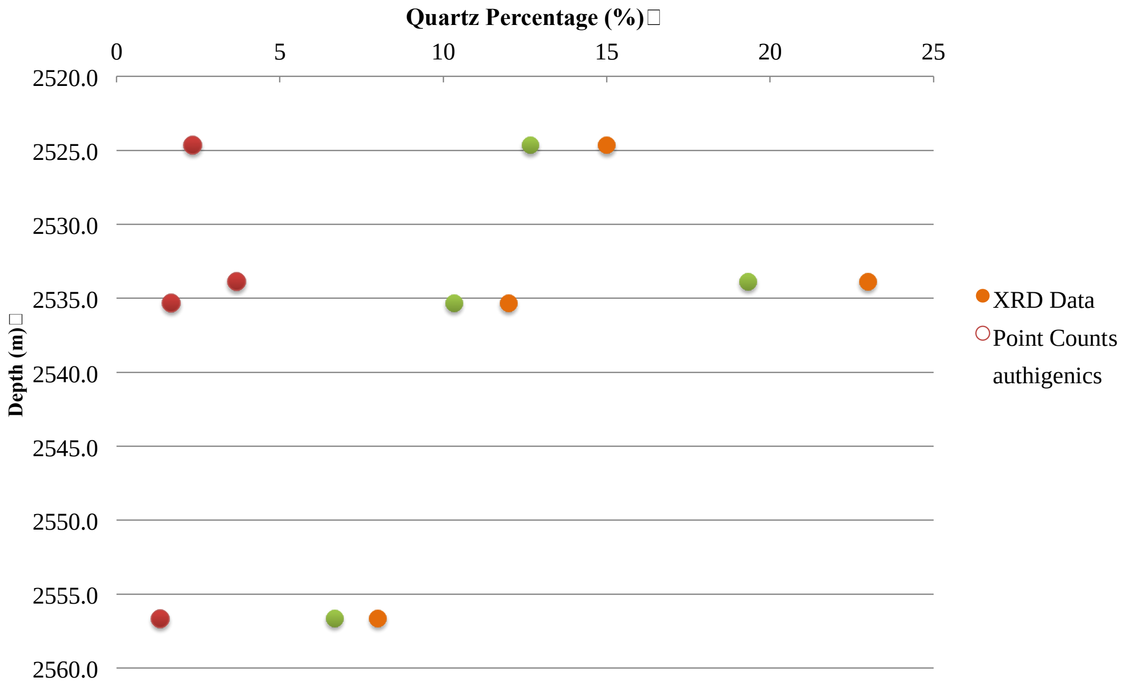

Figure 119: Quartz percentage vs. depth graph of high-maturity Well 3 samples

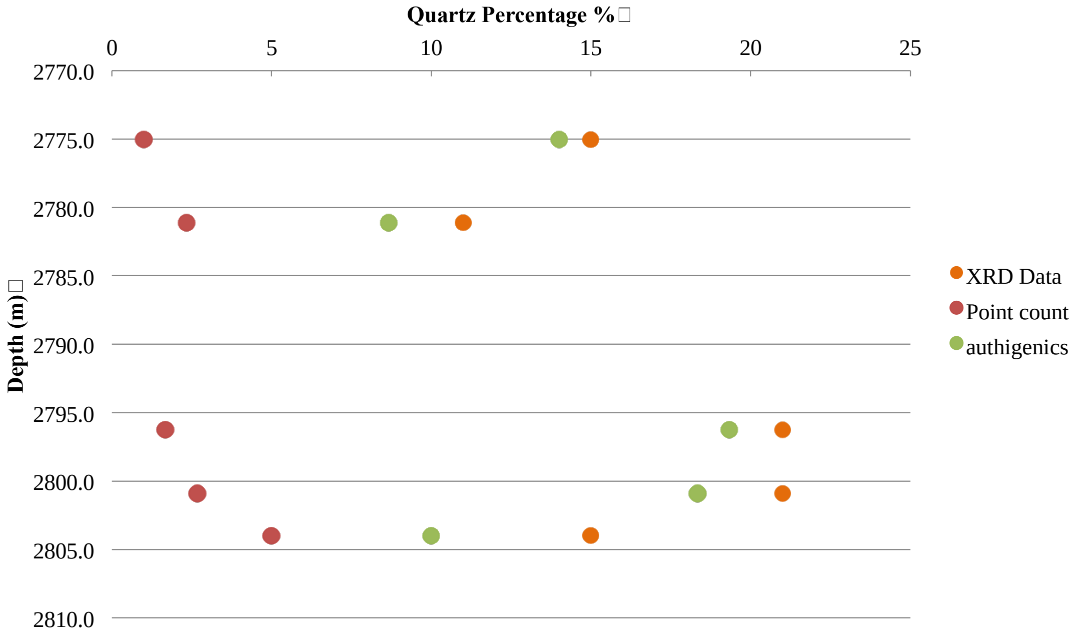

Figure 120: Quartz percentage vs. depth graph of high-maturity Well 4 samples

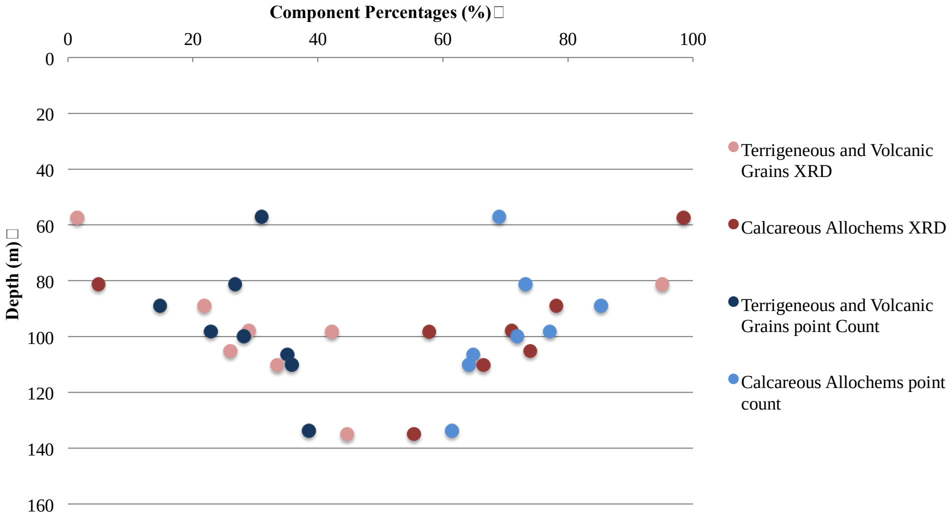

Figure 121: Comparison of point count and XRD results of calcareous allochems and terrigeneous and volcanic grains in the low maturity Well 1. Percentages of terrigeneous and volcanic grains and calcareous allochems of point counts are total to 100%, same as XRD results.

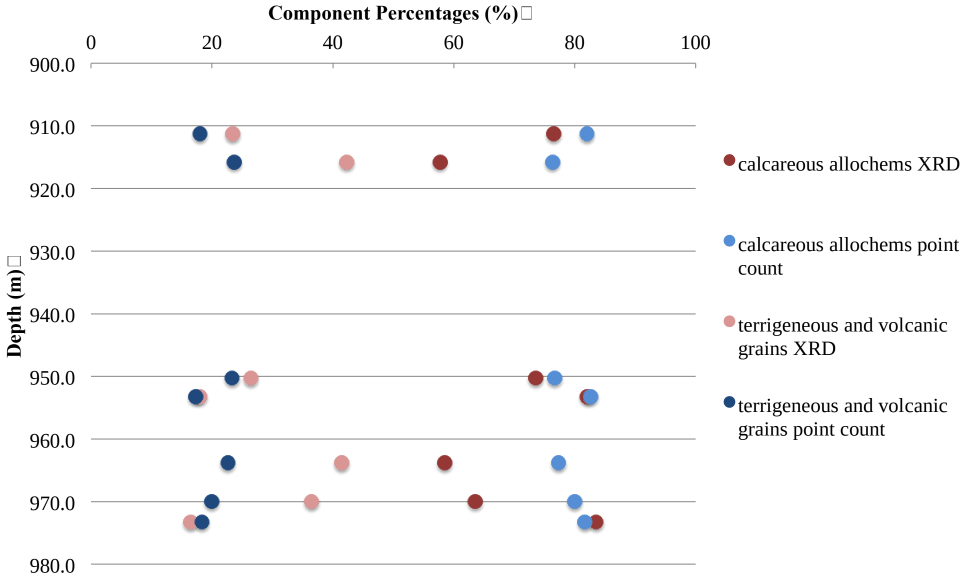

Figure 122: Comparison of point count and XRD results of calcareous allochems and terrigeneous and volcanic grains in the medium-maturity Well 2. Percentages of terrigeneous and volcanic grains and calcareous allochems of point counts are total to 100%, same as XRD results.

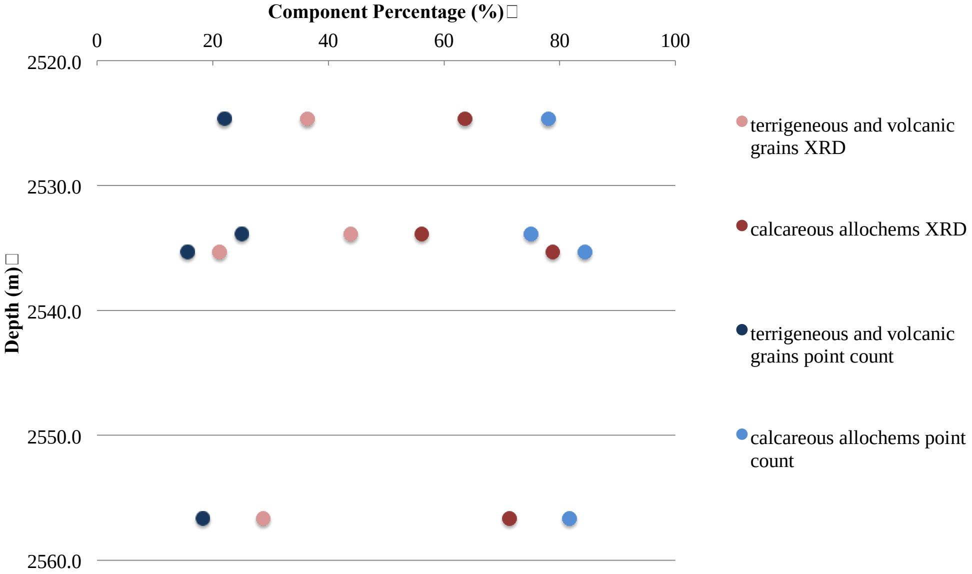

Figure 123: Comparison of point counts and XRD results of calcareous allochems and terrigeneous and volcanic grains in the high-maturity Well 3. Percentages of terrigeneous and volcanic grains and calcareous allochems of point counts are total to 100%, same as XRD results.

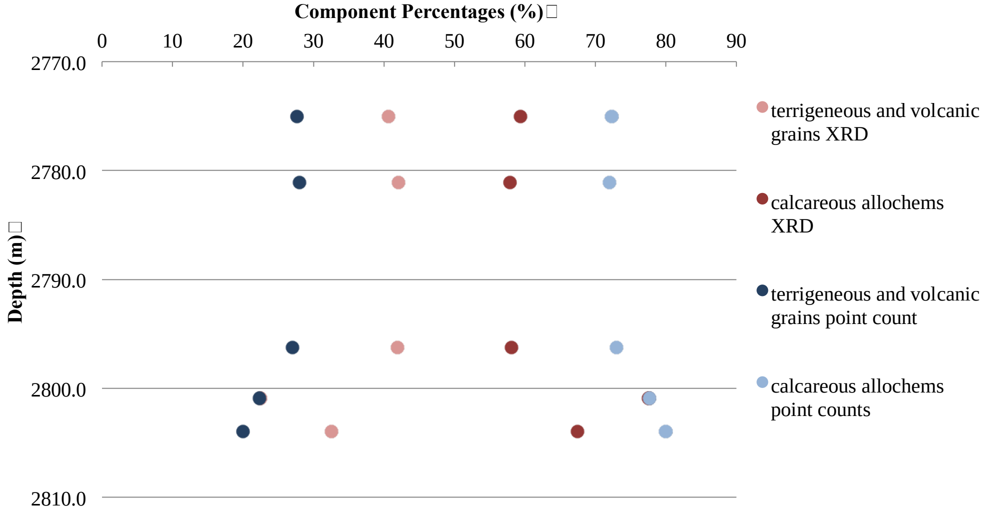

Figure 124: Comparison of point counts and XRD results of calcareous allochems and terrigeneous and volcanic grains in the high-maturity Well 4. Percentages of terrigeneous and volcanic grains and calcareous allochems of point count is total to 100%, same as XRD result

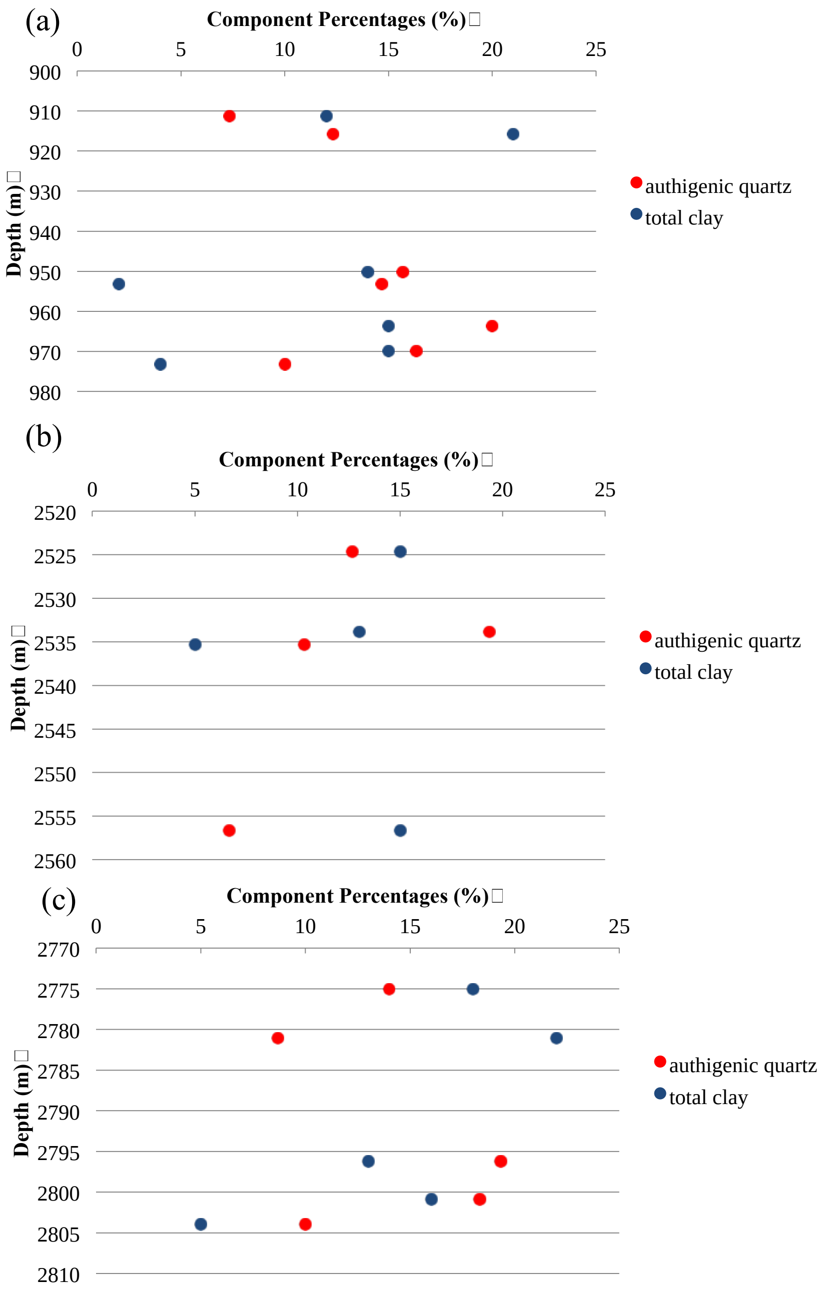

Figure 125: Authigenic quartz and clay percentages versus depth graphs of (a) medium-maturity Well 2 (b) high-maturity Well 3 and (c) high-maturity Well 4 samples. Note that there is not any trend.

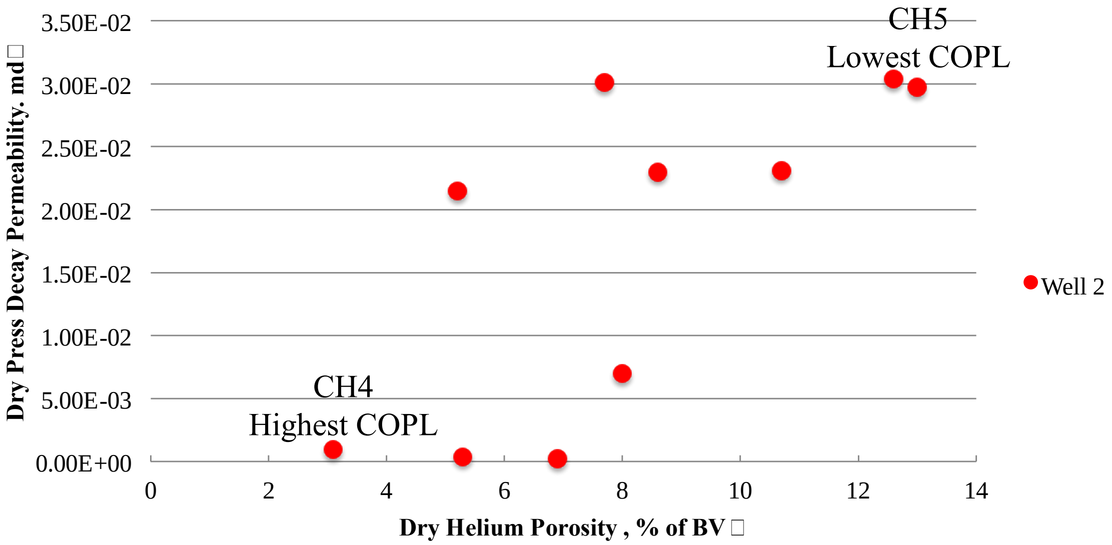

Figure 126: Porosity vs. permeability graph of medium maturity well samples

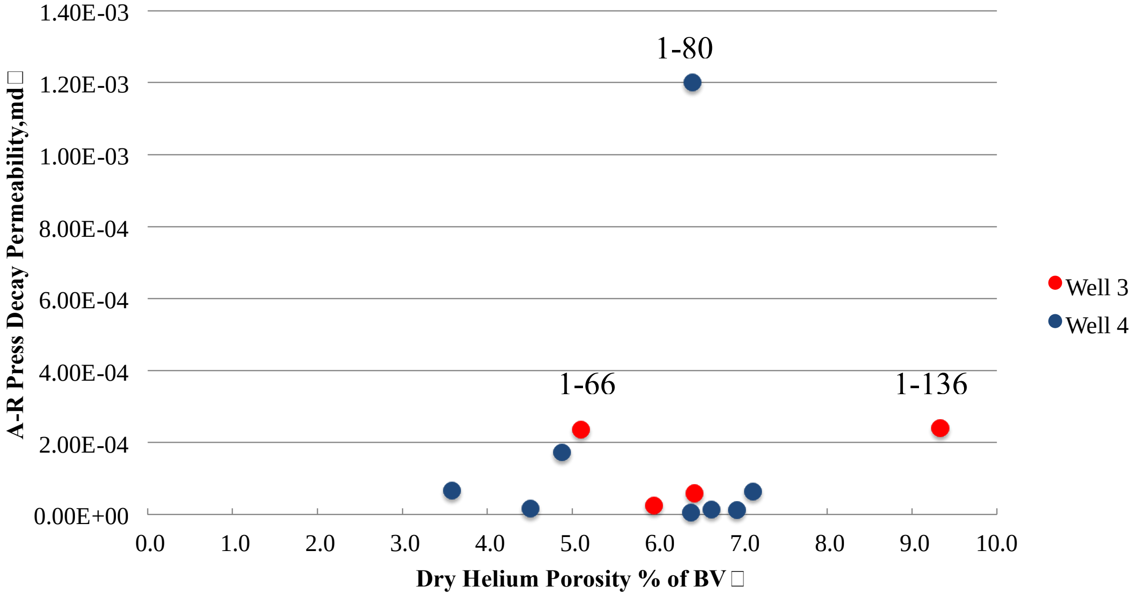

Figure 127: Porosity vs. permeability graph of high-maturity well samples

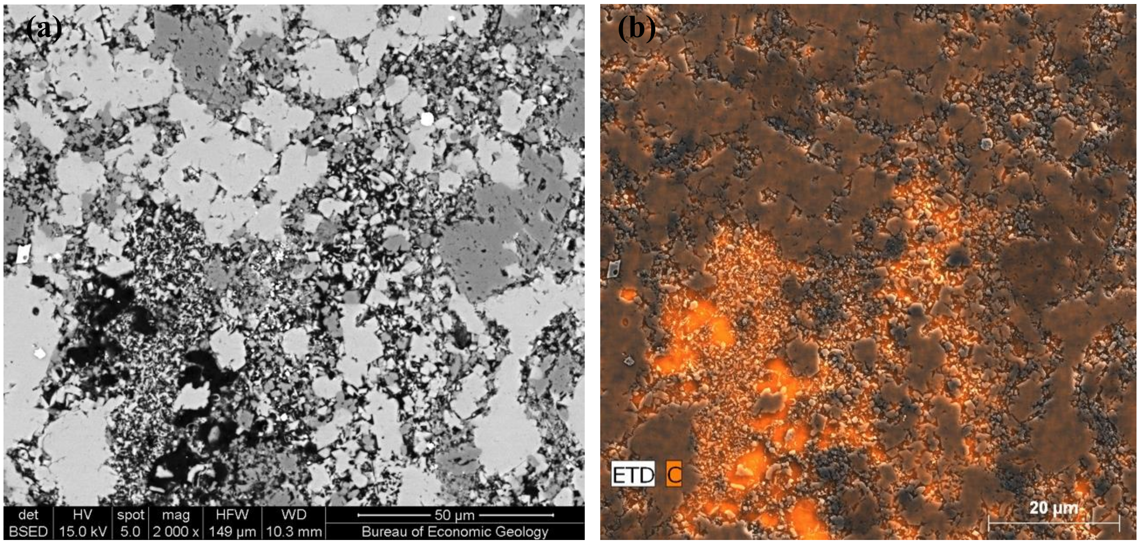

Figure 128: Interparticle porosity in the matrix is shown in the (a) BSED image (b) EDS X-ray map of the high-maturity Well 4 sample 1-80 (2797.93m)

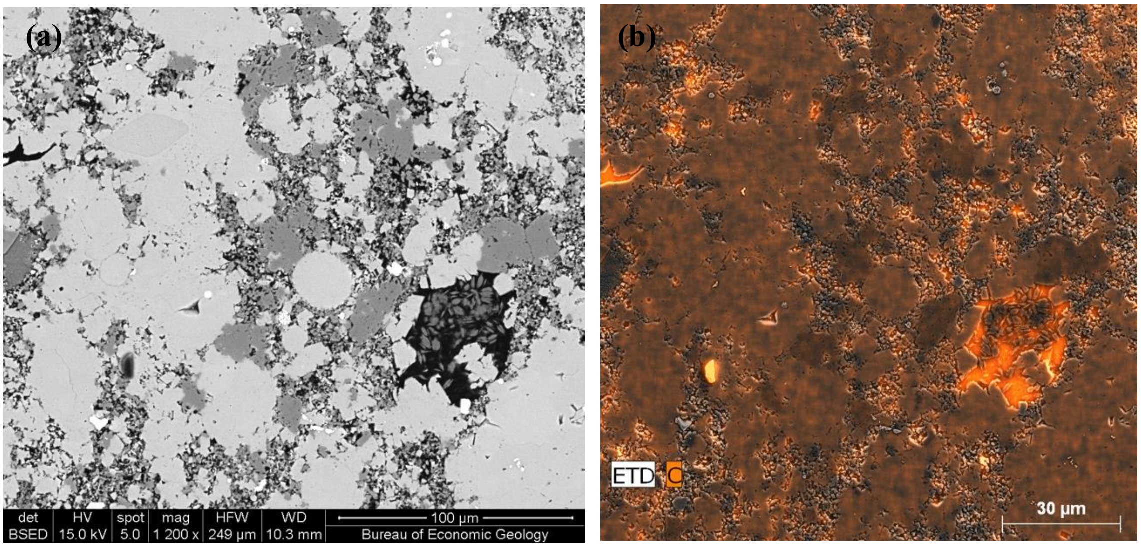

Figure 129: Interparticle oversize secondary porosity is shown in the (a) BSED image (b) EDS X-ray map of the high-maturity Well 4 sample 1-80 (2797.93m)

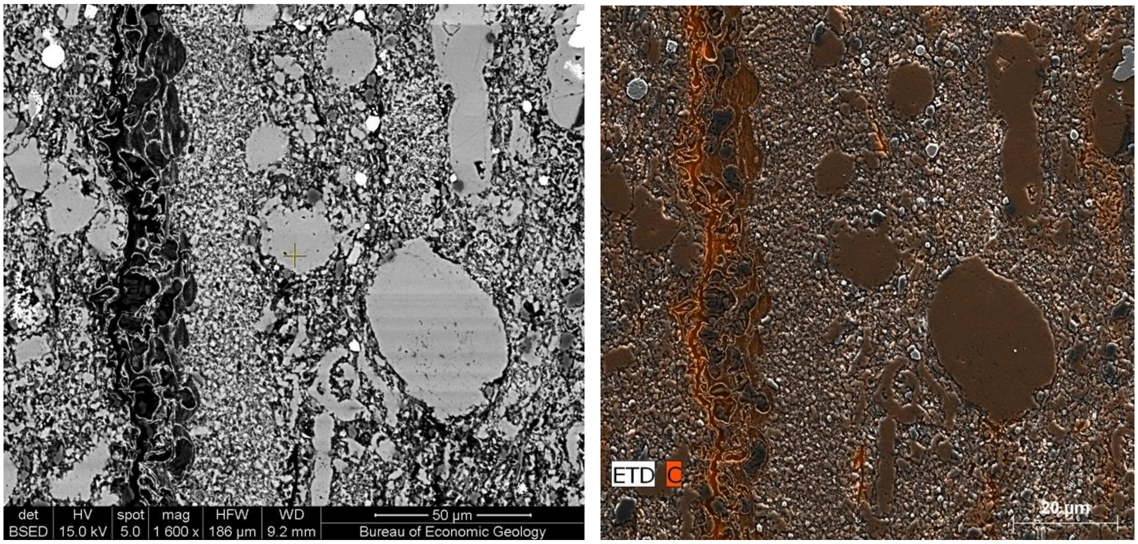

Figure 130: Intraparticle porosity within the phosphate fragment is shown in the (a) BSED image (b) EDS X-ray map of the high-maturity Well 3 sample 1-136 (2556m).

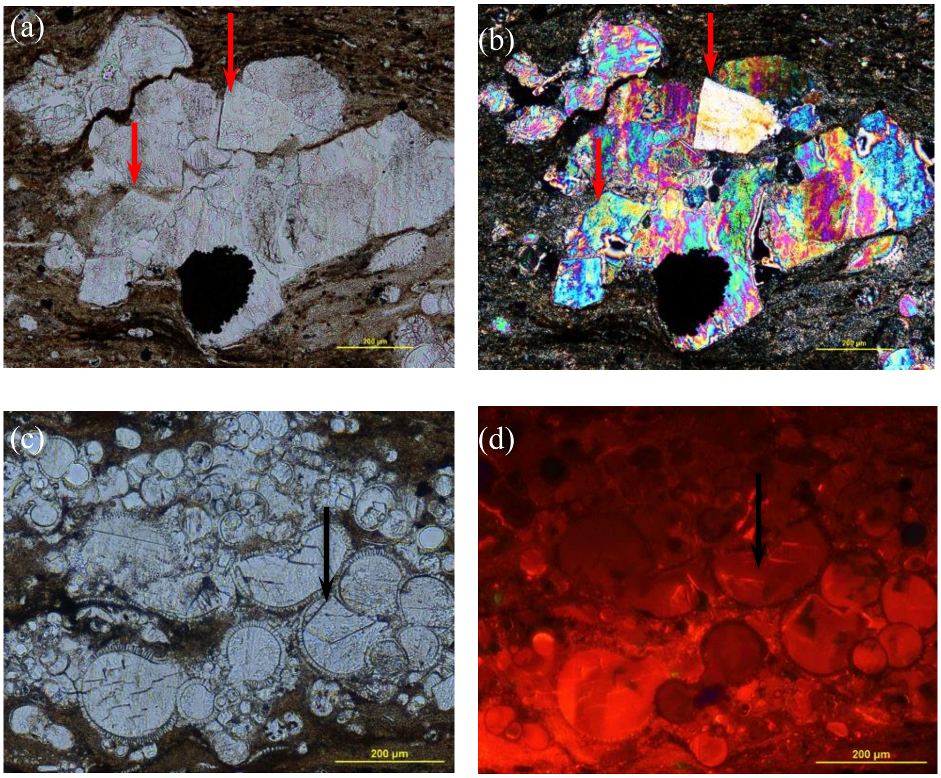

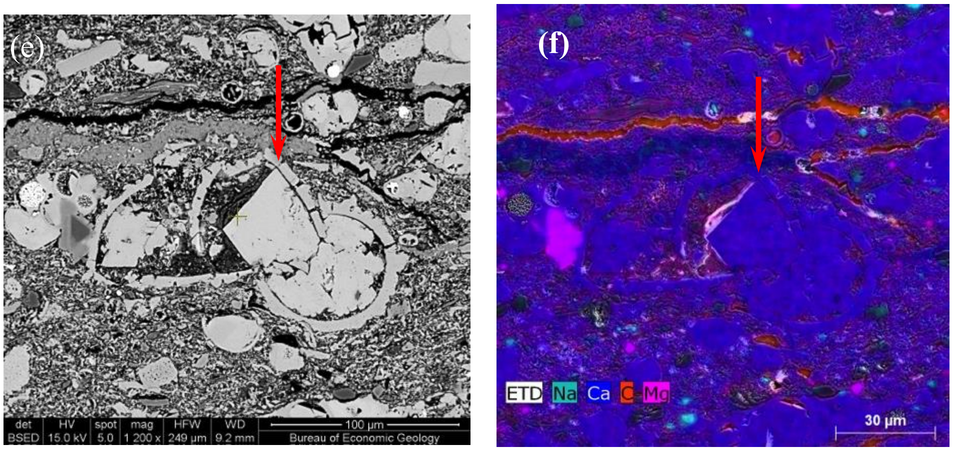

Figure 131: Various types of calcite replacement in marls (not generally observed in the argillaceous marls and calcareous tarls) are shown in the (a) transmitted light microscopy plane-polarized image of the Well 1 sample 16 (b) cross-polarized image of the Well 1 sample 16 (c) transmitted light microscopy plane-polarized image of the Well 1 sample 16 (d) CL image of the Well 1 sample 16 (e) BSED image of the Well 1 sample 20 (f) EDS X-ray map of the Well 1 sample 20. Note that they have euhedral calcite in common.

CONCLUSION

The Eagle Ford Formation in the Maverick Basin of South Texas were deposited in an area generally removed from siliciclastic influx coming from Woodbine depositional system of East Texas by the to the blocking effect of the San Marcos Arch (Ozkan et. al., 2014). Thus, the Eagle Ford is a carbonate-rich mudrock in the South Texas area. Lithologic heterogeneity, which is the main concern of this study, arises from the intermixing of detrital and authigenic components and the mixing of extrabasinal and intrabasinal components in the grain assemblage. Compositional mudrock classification which has three end members, terrigeneous and volcanic grains (extrabasinal grains), calcareous allochems (intrabasinal grains) and biosiliceous grains (intrabasinal grains) is applied to Eagle Ford and reveals three types of mudrocks, calcareous tarl, argillaceous marl and marl, that reflect the relative contributions of extrabasinal and intrabasinal components. Determination of authigenic processes and components precipitated as a result of these processes and their systematic change with the variety in detrital assemblage is another aspect of the study.

Compaction, cementation, grain dissolution, grain replacement, and recrystallization are the main diagenetic process identified in the Eagle Ford. Among them, compaction and cementation are the main drivers of the porosity loss. However it is important to note that compaction has superiority to the cementation according to the calculated compactional porosity loss even with the conservative assumptions of initial porosity values. Relative timing, which has notable affect on the description of rock properties, is interpreted with the consideration of crosscutting relationships, cement stratigraphy and shapes of the crystals mostly within the foraminifer tests. Prevalence of uncollapsed nature of foraminifers in the Eagle Ford is the evidence of early cementation. Compaction does not affect intraparticle porosity within the foraminifers, which is mostly reduced instead by cementation. The uncollapsed nature of radiolarians, which are identified dominantly as replaced, is the indicator of early replacement of calcite as well as early cementation in the Eagle Ford.

X-ray mapping technique is offered as an effective technique for the petrographic purposes suggested in this study. Although X-ray mapping discrimination of larger grains is sufficient to allow an estimate of the classification and diagenesis prediction until some point, the resolution is still too low to allow full discrimination of clay-size materials and nanopores. However, it can be concluded that X-ray mapping technique is promising since it allows to discriminate grains from the authigenics with different color intensities, shapes and to predict the relative timing of diagenetic processes.

Some conclusions obtained from this study are unexpected. For instance, because the Eagle Ford is not notably siliceous in bulk composition the presence of around 15% authigenic quartz precipitation was not expected. Dominant form of quartz in these rocks is authigenic. Quartz precipitation in the Eagle Ford is, in fact, quite similar to the much more siliceous Barnett Shale (Milliken et. al., 2012(b)). Although there is another possibility to have authigenic quartz, which is the clay diagenesis, any correlation with the authigenic quartz precipitation and change in clay abundances cannot be made. The mass balance between the precipitation of authigenic quartz and dissolution of unstable opaline skeletal grains and other reactive silicates is still unknown due to the challenges to predict initial volumes of detrital material and final volume of authigenic material exactly.

REFERENCES

Adkins, W.S. and Lozo, F. E., 1951, Stratigraphy of the Woodbine and Eagle Ford, Waco Area, Texas.

Aplin, A. C., and Macquaker, J. H. S., 2011, Mudstone diversity: Origin and implications for source, seal, and reservoir properties in petroleum systems. AAPG Bulletin, *95*(12), 2031–2059. doi:10.1306/03281110162

Arthur, M. a., Schlanger, S. O., and Jenkyns, H. C., 1987, The Cenomanian-Turonian Oceanic Anoxic Event, II. Palaeoceanographic controls on organic-matter production and preservation. *Geological Society, London, Special Publications*, *26*(1), 401–420. doi:10.1144/GSL.SP.1987.026.01.25

Arthur, M. A., Dean, W. E., and Pratt, L. M., 1988, Geochemical and Climatic effects of increased marine organic carbon burial at the Cenomanian/ Turonian boundary.

Arthur, M. A., and B. B. Sageman, 2004, Sea-level control on source-rock development: Perspectives from the Holocene Black Sea, the Mid-Cretaceous Western Interior Basin of North America, and the Late Devonian Appalachian Basin: SEPM Special Publication, v. 82, p. 35–59.

Bain, R., 1990, Diagenetic, nonevaporitive origin for gypsum. Geology, v. 18 no. 5, p 447-450.

Bennett, R. H., O'Brien N. R., and Hulbert, M. H., 1991, Determinants of clay microfabric signatures: processes and mechanisms. In Microstructure of Fine-Grained Sediments: From Mud to Shale (eds. R. H. Bennett, W. R. Bryant, M. H. Hulbert, and A.H. Bouma) Springer-Verlag, New York, p. 5–32.

Berner, R.A., 1980, Early diagenesis: A theoretical approach: New Haven, Connecticut, Princeton University Press, 256 p.

Blatt, H., Middleton, G., and Murray, R., 1972, Origin of sedimentary rocks. Prentice-Hall, Englewood Cliffs, New Jersey.

Blatt H., 1979, Diagenetic Processes in Sandstones: SEPM Spec. Pub. No. 26, p. 141-157.

Blowes, D. W., & Jambor, J. L., 1989, The pore-water geochemistry and the mineralogy of the vadose zone, *5*, 327–346.

Blatt, H., 1985, Provenance studies and mudrocks. SEPM Journal of Sedimentary Research, Vol. 55(1). doi:10.1306/212F8611-2B24-11D7-8648000102C1865D

Bjorlykke, K., 1983, Diagenetic reactions in sandstone. in Parker, A., and Sellwood, B.W., eds., Sediment Diagenesis: v. 115, p. 169-213.

Bjorlykke, K., Hoeg, K., 1997, Effects of burial diagenesis on stresses, compaction and fluid flow in sedimentary basins. Marine and Petroleum Geology 14, p. 267–276.

Boles, J. R., 1982, Active albitization of plagioclase, Gulf Coast Tertiary: Am. Jour. Sci., v. 282, p. 165-180.

Bridge, J. S., and R. V. Demicco, 2008, Earth surface pro- cesses, landforms and sediment deposits: New York, Cambridge University Press, 830 p.

Brown, C.W. and Pierce, R.L., 1962, Palynologic correlations in Cretaceous Eagle Ford Group, northeast Texas: Association of Petroleum Geologists Bulletin, v. 46, p. 2133-2147.

Buffler, R. T., Watkins, J. S., Shaub, F. J., and Worzel, J. L., 1980, Structure and early geologic history of the deep central Gulf of Mexico basin, in Pilger, R. H., Ed., Proc. of a symposium: The origin of the Gulf of Mexico and the early opening of the central north Atlantic Ocean, 3-16

Burton, J. H., Krinsley, D. H., and Eye, K., 1987, Authigenesis of Kaolinite and Chlorite in Texas Gulf Coast Sediments, *35*(4), 291–296.

Chayes, F., 1956, Petrographical modal analysis: An elementary statistical appraisal: New York, John Wiley & Sons, 113p.

Cobbold, P. R., Zanella, A., Rodrigues, N., and Løseth, H., 2013, Bedding-parallel fibrous veins (beef and cone-in-cone): Worldwide occurrence and possible significance in terms of fluid overpressure, hydrocarbon generation and mineralization. Marine and Petroleum Geology, 43, 1–20. doi:10.1016/j.marpetgeo.2013.01.010

Corbett, M. J., and Watkins, D. K., 2013, Calcareous nannofossil paleoecology of the mid-Cretaceous Western Interior Seaway and evidence of oligotrophic surface waters during OAE2 Palaeogeography, Palaeoclimatology, Palaeoecology, 392, 510–523. doi:10.1016/j.palaeo.2013.10.007

Cotera, A.S., Jr., 1956, Petrology of the Cretaceous Woodbine Sand in Northeast Texas: M.S. Thesis, The University of Texas at Austin, Austin, TX.

Curtis, C. D., 1983, Geochemistry of Porosity Enhancement and Reduction in Clastic Sediments. Geological Society, London, Special Publications, 12(1), 113–125. doi:10.1144/GSL.SP.1983.012.01.12

Dawson, W. C., Austin, T., Ford, E., and Austin, A., 1997, Limestone Microfacies and Sequence Stratigraphy : Eagle Ford Group (Cenomanian-Turonian) North-Central Texas Outcrops.

Dawson, W.C., 2000, Shale microfacies: Eagle Ford Group (Cenomanian-Turonian) north-central Texas outcrops and subsurface equivalents: Gulf Coast Association of Geological Societies Transactions, v. 50, p. 607-621.

Dawson, W. C., and Almon, W. R., 2010, Eagle Ford Shale Variability: Sedimentologic Influences on Source and Reservoir Character in an Unconventional Resource Unit, 181–190.

Day-Stirrat, R. J., Dutton, S. P., Milliken, K. L., Loucks, R. G., Aplin, A. C., Hillier, S., and Van der Pluijm, B., 2010, Fabric anisotropy induced by primary depositional variations in the silt: clay ratio in two fine-grained slope fan complexes: Texas Gulf Coast and northern North Sea. Sedimentary Geology, 226(1-4), 42–53. doi:10.1016/j.sedgeo.2010.02.007

Dean, W. E., Leinen, M. and Stow, D. A., 1985, Classification of Deep-Sea, Fine-Grained Sediments. J. Sed. Petrol. V. 55, p. 250-256

Dewhurst, D. N., Aplin A.C., Sarda J.P., and Yang C.Y.L., 1998, Compaction-driven evolution of porosity and permeability in natural mudstones: An experimental study: Journal of Geophysical Research Solid Earth, v. 103, p. 651–661. doi:10.1029/97JB02540.

Dow, W. G., 1977, Kerogen studies and geological interpretations: Journal of Geochemical Exploration, v. 7, p. 79–99

Ehrenberg, S.N., 1995, Measuring sandstone compaction from modal analysis of thin sections: How to do it and what the results mean: Journal of Sedimentary Research, v. A65, p 369-379.

Ekdale, A. A., and T. R. Mason, 1988, Characteristic trace- fossil associations in oxygen-poor sedimentary envi- ronments: Geology, v. 16, p. 720-723.

Fairbanks, M. D., 2012, High Resolution Stratigraphy and Facies Architecture of the Upper Cretaceous (Cenomanian-Turonian) Eagle Ford Group, Central Texas: [Master's Thesis] University of Texas at Austin, Austin, TX

Faust, M. J., 1990, Seismic stratigraphy of the mid-Cretaceous unconformity (MCU) in the central Gulf of Mexico basin, *55*(7), 868–884

Fishman, N., Guthrie, J. M., and Honarpour, M., 2014, Development of Organic and Inorganic Porosity in the Cretaceous Eagle Ford Formation, South Texas

Flawn, P. T., 1953, Petrographic classification of argillaceous sedimentary and low-grade metamorphic rocks in subsurface: Am. Assoc. Petroleum Geologists Bull., v. 37, p. 560-565.

Flemming, B. W., 2000, A revised textural classification of gravel-free muddy sediments on the basis of ternary diagrams, 20, 1125–1137.

Folk, R.L., 1954, The distinction between grain size and mineral composition in sedimentary-rock nomenclature. Journal of Geology v. 62, p. 344-359.

Folk, R. L., 1959, Practical petrographic classification of limestones: AAPG Bulletin, v. 43, p. 1–38

Folk, R. L., 1962, Petrography and Origin of the Silurian Rochester and McKenzie Shales, Morgan County, West Virginia SEPM Journal of Sedimentary Research, Vol. 32(3), 539–578. doi:10.1306/74D70D17-2B21-11D7-8648000102C1865D

Folk, R. L., 1965, Some aspects of recrystallization in ancient limestones, in Dolomitization and Umestone diagenesis: Soc. Econ. Paleontologists and Mineralogists Spec. Pub. No. 13, p. 124-168.

Folk, R.L., 1980, Petrology of Sedimentary Rocks: Austin, Texas, Hemphill Publishing Co., 182 p

Fontoura, S. A. B., Janeiro, R. De, & Rabe, C., 2002, Characterization of Shales for Drilling Purposes.

Galloway, W.E., 2008, Depositional evolution of the Gulf of Mexico sedimentary basin, in A.D. Miall, (ed.), The sedimentary basins of the United States and Canada: Elsevier, Amsterdam, Netherlands, v. 5, p. 505-549.

Gazzi, P., 1966, Le arenarie del flysch sopracretaceo dell'Appeninno modenese; correlazioni con il flysch di Monghidoro: Mineralog. et Petrog. Acta, v. 12, p. 69-97.

Gazzi, P., and Zuffa, G. G., 1970, Le arenarie paleogen-iche dell'Appennino emiliano: Miner. Petrogr. Acta, v. 16, p. 97-137.

Gazzi, P., Zuffa, G. G., Gandolfi, G., and Paganelli, L., 1973, Provenienza e dispersione fitoranea delle sabbie delle spiagge adriatiche fra le foci dell'Isonzo e del Foglia: inquadramento regionale: Soc. Geol. Italiana Mem., v. 12, p. 1-37

Grabowski, G.J., 1984, Generation and migration of hydrocarbons in Upper Cretaceous Austin Chalk, south-central Texas, in Palacas, J.G., ed., Petroleum geochemistry and source rock potential of carbonate rocks: AAPG Studies in Geology 18, p. 97-115.

Grainger, P., 1984, The classification of mudrocks for engineering purposes. Quarterly Journal of Engineering Geology and Hydrogeology, *17*(4), 381–387. doi:10.1144/GSL.QJEG.1984.017.04.13

Haq, B.V., J. Hardenbol, and P. R. Vail, 1988, Mesozoic and Cenozoic chronostratigraphy and eustatic cycles, in Wilgus, C. K., et al., (eds), Sea-level changes-An Integrated Approach: Society of Economic Paleontologists and Mineralogists Special Publication 42, p 71- 108.

Hancock, J. M., 1975, The petrology of the Chalk. Proceedings of the Geologists' Association, *86*(4), 499–535. doi:10.1016/S0016-7878(75)80061-7

Hancock, J. M., 1993, Sea-level changes around the Cen- omanian Turonian boundary: Cretaceous Research, v. 14, p. 553-562.

Harbor, R., 2011, Facies characterization and stratigraphic architecture of organic-rich mudrocks, Upper Cretaceous Eagle Ford Formation, South Texas

Retrieved from http://repositories.tdl.org/tdl-ir/handle/2152/ETD-UT-2011-08-3892

Hart, B., Macquaker, J., and Taylor, K., 2013, "Mudstone ("shale") depositional and diagenetic processes: Implications for seismic analyses of source-rock reservoirs." Interpretation, 1(1), B7–B26. doi: 10.1190/INT-2013-0003.1

Hattin, D. E., 1981, Petrology of Smoky Hill Member, Niobrara Chalk (Upper Cretaceous), in Type Area, Western Kansas

Hayes, J. B., 1979, Sandstone Diagenesis-the hole truth: Soc. Econ. Paleontol. Mineral. Spec. Publ. No. 26

Herron, M. M., 1988, Geochemical Classification of Terrigenous Sands and Shales from Core or Log Data SEPM Journal of Sedimentary Research, Vol. 58(5), 820–829. doi:10.1306/212F8E77-2B24-11D7-8648000102C1865D

Hower, J., Eslinger E.V., Hower M.E., and Perry E.A., 1976, Mechanism of burial metamorphism of argillaceous sediment: 1. Mineralogical and chemical evidence: Geological Society of America Bulletin, v. 87, p. 725–737. doi:10 .1130/0016-7606(1976)87<725:MOBMOA>2.0 .CO;2.

Huc, A.Y., Le Fournier, J., Vandenbroucke, M., and Bessereau, G., 1990, Northern Lake Tanganyika. An example of organic sedimentation in an anoxic rift lake. In: Katz, B.J. (Ed.), Lacustrine Basin Exploration – Case Studies and Modern Analogs American Association of Petroleum Geologists – Memoir 50. American Association of Petroleum Geologists, Tulsa, Oklahoma, pp. 169–185.

Hutton, A. C., 1987, Petrographic classification of oil shales. International Journal of Coal Geology, 8(3), 203–231. doi:10.1016/0166-5162(87)90032-2

Isaacs, C. M., 1982, Influence of rock composition on kinetics of silica phase changes in the Monterey Formation, Santa Barbara area, California. U.S. Geological Survey, 10, 304–308.

Jennings, D. S., & Antia, J., 2013, Petrographic Characterization of the Eagle Ford Shale, South Texas: Mineralogy, Common Constituents, and Distribution of Nanometer-scale Pore Types, 101–114. doi:10.1306/13391708M1023586

Jiang, M., 1989, Biostratigraphy and geochronology of the Eagle Ford Shale, Austin Chalk, and Lower Taylor marl in Texas based on calcareous nannofossils. (Volumes I and II), Phd Dissertation, Texas A&M University.

Kastner, M., 1971, Authigenic feldspars in carbonate rocks: American Mineralogist v. 56, p. 1403-1442

Land, S., and Milliken, L., 1981, Feldspar diagenesis in the Frio Formation, Brazoria County , Texas Gulf Coast, (July), 314–318.

Land, L. S., Mack, L. E., Milliken, K. L., Lynch, and F. L., 1997, GSA Bulletin: Burial diagenesis of argillaceous sediment, south Texas Gulf of Mexico sedimentary basin: A reexamination. doi:10.1130/0016-7606(1997)109<0002

Lash, G.G., 1987, Sedimentology and possible paleoceanographic significance of mudstone turbidites and associated deposits of the Pen Argyl Member, Martinsburg Formation (Upper Ordovician), eastern Pennsylvania. Sediment. Geol., 54: 113-135.

Liro, L. M., Dawson, W. C., Katz, B. J., and Robison, V. D., 1994, Sequence-Stratigraphic Elements and Geochemical Variability Within a Condensed Section": Eagle Ford Group, East-Central Texas. *GCAGS Transactions*, *78*(1987), 393–402.

Retrieved from http://www.crossref.org/deleted_DOI.html

Lock, B. E., Peschier, L., and Whitcomb, N., 2010, The Eagle Ford (Boquillas Formation) of Val Verde County, Texas: A Window on the South Texas Play, 419–434.

Longman, M. W., Luneau, B. A., and Landon, S. M., 1998, Nature and Distribution of Niobrara Lithologies in the Cretaceous Western Interior Seaway of the Rocky Mountain Region1, *35*(4)

Loucks, R. G., Reed, R. M., Ruppel, S. C., and Hammes, U. (2012). Spectrum of pore types and networks in mudrocks and a descriptive classification for matrix-related mudrock pores. AAPG Bulletin, 96(6), 1071–1098. doi:10.1306/08171111061

Lu, J., Milliken, K., Reed, R. M., and Hovorka, S., 2011, Diagenesis and sealing capacity of the middle Tuscaloosa mudstone at the Cranfield carbon dioxide injection site, Mississippi, U.S.A. Environmental Geosciences, 18(1), 35–53. doi:10.1306/eg.09091010015

Lundegard, P.D. and Samuels, N.D., 1980, Field classification of fine-grained sedimentary rocks. Journal of Sedimentary Petrology 50,781-786.

Lundegard, P.D. and Samuels, N.D., 1981, Field classification of fine-grained sedimentary rocks- reply. Journal of Sedimentary Petrology v. 51(3), p. 1031-1033.

Lundegard, P., 1992, Sandstone Porosity Loss-A " Big Picture" View of The Importance of Compaction, journal of Sedimentary Petrology, v. 62, no. 2, 250-260 p.

Machel, H. G., 1985, Cathodoluminescence in Calcite and Dolomite and Its Chemical Interpretation. Journal of Geological Association of Canada, v. 12(4), p. 139–147.

Macquaker, J. H. S., and Gawthorpe, R. L., 1993, Mudstone Lithofacies in the Kimmeridge Clay Formation, Wessex Basin, Southern England: Implications for the Origin and Controls of the Distribution of Mudstones. SEPM Journal of Sedimentary Research, Vol. 63. doi:10.1306/D4267CC1-2B26-11D7-8648000102C1865D

Macquaker, J.H.S., Gawthorpe, R.L., Taylor, K.G., and Oates, M.J., 1998, Heterogeneity, stacking patterns and sequence stratigraphic interpretation in distal mudstone successions: examples from the Kimmeridge Clay Formation, U.K., in Schieber, J., Zimmerle, W., and Sethi, P.S., eds., Shales and Mudstones: Schweizerbart'sche Verlagsbuchhandlung, Stuttgart, p. 163–186.

Macquaker, J. H. S., & Howell, J. K., 1999, Small-scale (<5.0 m) vertical heterogeneity in mudstones: implications for high-resolution stratigraphy in siliciclastic mudstone successions. Journal of the Geological Society, v. 156(1), p. 105–112. doi:10.1144/gsjgs.156.1.0105

Macquaker, J. H. S., & Adams, A. E., 2003, Maximizing Information from Fine-Grained Sedimentary Rocks: An Inclusive Nomenclature for Mudstones. Journal of Sedimentary Research, v. *73*(5), p. 735–744. doi:10.1306/012203730735

Macquaker, J. H. S., Taylor, K. G., and Gawthorpe, R. L., 2007, High-Resolution Facies Analyses of Mudstones: Implications for Paleoenvironmental and Sequence Stratigraphic Interpretations of Offshore Ancient Mud-Dominated Successions. Journal of Sedimentary Research, v. *77*(4), p. 324–339. doi:10.2110/jsr.2007.029

Macquaker, J. H. S., Keller, M. A., and Davies, S. J., 2010, Algal Blooms and "Marine Snow": Mechanisms That Enhance Preservation of Organic Carbon in Ancient Fine-Grained Sediments. Journal of Sedimentary Research, v. 80(11), p. 934–942. doi:10.2110/jsr.2010.085

Marshall, J. D., 1982, Isotopic Composition of Displacive Fibrous Calcite Veins reversals in pore-water composition trends during burial diagenesis, v. 52(2), p. 615–630.

Martill, D.M., 1987, A taphonomic and diagenetic case study of a partially articulated ichthyosaur. Palaeontology v. 30, p. 543-555.

Mcbride, E. F., 1974, Significance of Color in Red, Green, Purple, Olive, Brown, and Gray Beds of Difunta Group, Northeastern Mexico. SEPM Journal of Sedimentary Research, Vol. 44(3), 760–773. doi:10.1306/212F6B9A-2B24-11D7-8648000102C1865D

McGarity, A. H. (2013). Facies and Stratigraphic Framework of the Eagle Ford Shale in South Texas: [Master's thesis] University of Houston, Houston, TX.

McGregor, R. G., and Blowes, D. W., 2002, The physical, chemical and mineralogical properties of three cemented layers within sulfide-bearing mine tailings, 76, 195–207.

Miller, R.W., 1990, The stratigraphy and depositional environment of the Boquillas Formation of Southwest Texas: [Master's thesis] The University of Texas at Arlington, Arlington, TX.

Milliken, K. L., 1989, Petrography and composition of authigenic feldspars, Oligocene Frio Formation, South Texas. SEPM Journal of Sedimentary Research, Vol. 59(3), 361–374. doi:10.1306/212F8F94-2B24-11D7-8648000102C1865D

Milliken, K., 1992, Chemical Behavior of Detrital Feldspars in Mudrocks Versus Sandstones, Frio Formation (Oligocene), South Texas, 62(5), 790–801.

Milliken, K. L., & Land, L. S., 1993, The origin and fate of silt sized carbonate in subsurface Miocene-Oligocene mudstones, south Texas Gulf Coast. Sedimentology, 40(1), 107–124. doi:10.1111/j.1365-3091.1993.tb01094.x

Milliken, K. L., 1994, Cathodoluminescent Textures and The Origin of Quartz Silt in Oligocene, 567–571.

Milliken, K.L., 2003. Diagenesis. In: Middleton, G.V., Church, M.J., Coniglio, M. (Eds.), Encyclopedia of Sediments and Sedimentary Rocks. Kluwer Academic Publishers, Dordrecht, pp. 214-219

Milliken, K. L., Day-stirrat, R. J., Papazis, P. K., Dohse, C., and Christi, C., 2012 (a), Carbonate Lithologies of the Mississippian Barnett Shale, Fort Worth Basin, Texas, p. 290–321. doi:10.1306/13321473M97252

Milliken, K. L., Esch, W. L., Reed, R. M., and Zhang, T., 2012 (b), Grain assemblages and strong diagenetic overprinting in siliceous mudrocks, Barnett Shale (Mississippian), Fort Worth Basin, Texas. AAPG Bulletin, v. 96(8), p. 1553–1578. doi:10.1306/12011111129

Milliken, K. L., Macquaker, J., and Taylor, K., 2012 (c), Early diagenetic kaolinite precipitation: a widespread phenomenon in organic-rich mudrocks (abs.): Gulf Coast Association of Geological Societies Transactions, v. 62, p. 763

Milliken, K. L., 2013, SEM-Based Cathodoluminescence imaging for discriminating quartz types in mudrocks, p. 1–10.

Milliken, K. L., Rudnicki, M., Awwiller, D. N., and Zhang, T., 2013, Organic matter-hosted pore system, Marcellus Formation (Devonian), Pennsylvania. AAPG Bulletin, 97(2), 177–200. doi:10.1306/07231212048

Milliken, K. L., and Day-stirrat, R. J., 2013, Cementation in mudrocks: Brief review with examples from Cratonic Basin Mudrocks, 133–150.

Milliken, K. L., Ko T. L., Pommer M., Marsaglia K., 2014, Mediterranean Sapropels: Analogues for Petrographic Assessment of Organic Matter in Oil and Gas Shales (abs.): in American Association of Petroleum Geologists Annual Convention and Exhibition, Houston, Texas.

Mondol, N. H., K. Bjorlykke, J. Jahren, and K. Hoeg, 2007, Experimental mechanical compaction of clay mineral aggregates—Changes in physical properties of mudstones during burial: Marine and Petroleum Geology, v. 24, p. 289–311. doi:10.1016/j.marpetgeo.2007.03.006

Montgomery, S.L. 1991, Horizontal drilling in the Austin Chalk; Part 2, Patterns of production: Petroleum Frontiers, v. 7, no. 4, 58 p

Montgomery, S. L., A. J. Petty, and P. J. Post, 2002, James Limestone, northeastern Gulf of Mexico: Refound opportunity in a Lower Cretaceous trend: American Association of Petroleum Geologists Bulletin, v. 86, p. 381–397

Muller, G., 1967, Diagenesis in argillaceous sediments. In G. Larsen and G.V. Chilingar (Editors), Diagenesis in Sediments, Elsevier, Amsterdam, p. 126-177

O'Brien, N. R., and R. M., Slatt, 1990, Argillaceous rock atlas: New York, Springer-Verlag, p. 141

Ozkan, A., Macaulay C., Milliken K. L., Pommer M. E., Ergene S. M., Minisini D., Eldrett J., Bergman S., Kelly A., 2014, Evolution of Pore Systems in Eagle Ford Mudstones: Influence of Texture, Diagenesis, and Thermal Maturity (abs.): in American Association of Petroleum Geologists Annual Convention and Exhibition, Houston, Texas.

Papazis, P. K., 2005, Petrographic Characterization of the Barnet Shale, Forth Worth Basin, Texas: [Master's Thesis] University of Texas at Austin, Austin, TX.

Paxton, S. T., J. O. Szabo, J. M. Adjukiewicz, and R. E. Klimentidis, 2002, Construction of an intergranular volume compaction curve for evaluating and predicting compaction and porosity loss in rigid-grain sandstone reservoirs: AAPG Bulletin, v. 86, p. 2047–2067

Pessagno, E.A., 1969, Upper Cretaceous stratigraphy of the western Gulf Coast area of Mexico, Texas, and Arkansas: Geological Society of America Memoir v. 111, p. 139.

Pettijohn, F. J., 1975, Sedimentary Rocks. 3rd ed. Harper and Row, New York, p. 628.

Pettijohn, F.J., Potter, P.E., and Siever, R., 1987, Sand and Sandtsone, Springer-Verlag New York Inc, second edition

Phelps, R. M., 2011, Middle-Hauterivian to Lower-Campanian Sequence Stratigraphy and Stable Isotope Geochemistry of The Comanche Platform, South Texas.

Phelps, R. M., Kerans C., Loucks R. G., Gama R. D., Jeremiah, J., and Hull, D., 2014, Oceanographic and eustatic control of carbonate platform evolution and sequence stratigraphy on the Cretaceous (Valanginian-Campanian) passive margin, northern Gulf of Mexico: Sedimentology, v. 61 (2), p. 461-496.

Pollastro, R. M., 2009, Natural Fractures, Composition, Cyclicity, and Diagenesis of the Upper Cretaceous Niobrara Formation, Berthoud Field, Colorado, (3), 243–256.

Proshlyakov, B.K., 1960, Reservoir properties of rocks as a function of their depth and lithology. Geol. Neft'i Gaza, (12): 24-29.

Pye, K., and Miller, J., 1990, Chemical and biochemical weathering of pyritic mudrocks in a shale embankment. Quarterly Journal of Engineering Geology and Hydrogeology, 23(4), 365–382. doi:10.1144/GSL.QJEG.1990.023.04.11

Pommer, M., 2014, Quantitative Assessment of Pore Types and Porosity Distribution Across Thermal Maturity, Eagle Ford Formation, South Texas; [Master's Thesis] University of Texas at Austin, Austin, TX

Railroad Commission of Texas, 2011, Eagle Ford information, <http://www.rrc.state.tx.us/eagleford/index#general>, Accessed August 15, 2012

Reed, R.M., and Milliken, K.L., 2003, How to overcome imaging problems associated with carbonate minerals on SEM-based cathodoluminescence systems: Journal of Sedimentary Research, v. 73, p. 326-330.

Rieke Ill, H. H., and Chilinoarian, G. V., 1974, Compaction of Argillaceous Sediments: New York, Elsevier, 424 p.

Robison, C. R., 1997, Hydrocarbon source rock variability within the Austin Chalk and Eagle Ford Shale (Upper Cretaceous), East Texas, U.S.A., 34, 287–305.

Salvador, A. and Muñeton, J.M. Q., 1989, Stratigraphic Correlation Chart Gulf of Mexico Basin, in Salvador, A., ed., The Gulf of Mexico Basin: Boulder Colorado, Geological Society of America, The Geology of North America, v. J., plate 5.

Schieber, J., and Zimmerle, W., 1998, The history and promise of shale research. In: J. Schieber, W. Zimmerle, and P. Sethi (editors), Shales and Mudstones (vol. 1): Basin Studies, Sedimentology and Paleontology, Schweizerbart'sche Verlagsbuchhandlung, Stuttgart, p. 1-10.

Schieber, J., Krinsley, D., and Riciputi, L., 2000, Diagenetic origin of quartz silt in mudstones and implications for silica cycling. Nature, v. 406(6799), p. 981–5. doi:10.1038/35023143

Scholle, P. A., and Halley, R. B., 1985, Burial Diagenesis: Out of sight, out of Mind: Soc. Econ. Paleontol. Mineral. Spec. Publ.

Scholle, P.A., and Ulmer-Scholle, D.S., 2003, A color guide to the petrography of carbonate rocks: grains, textures, porosity, diagenesis, AAPG Memoir 77, Tulsa, The American Association of Petroleum Geologists, p. 64.

Schlanger, S. O., Arthur, M. a., Jenkyns, H. C., & Scholle, P. a., 1987, The Cenomanian-Turonian Oceanic Anoxic Event, I. Stratigraphy and distribution of organic carbon-rich beds and the marine 13C excursion. Geological Society, London, Special Publications, v. 26(1), p. 371–399. doi:10.1144/GSL.SP.1987.026.01.24

Sellards, E.H., Adkins,W.S., Plummer, F.B., 1932, The geology of Texas, I: Stratigraphy: The University of Texas Bulletin No. 3232, p 422-439.

Shaw, H.F., 1997, Inside Mudrocks-A Review of The Petrology of Siliciclastic Mudrocks: Ground Chemistry: Implications for Construction

Shepard, F.P., 1954. Nomenclature based on sand-silt-clay ratios. Journal of Sedimentary Petrology 24, 151-158

Sinton, C.W. and Duncan, R.A. (1997) Potential links between ocean plateau volcanism and global ocean anoxia at the Cenomanian-Turonian boundary. Econ. Geol., 92, 836–842

Sippel, R.F., 1968, Sandstone petrology, evidence from luminescence petrography: Journal of Sedimentary Petrology, v. 38, p. 530-554.

Slatt, R. M., & Brien, N. R. O., 2013, Microfabrics Related to Porosity Development, Sedimentary and Diagenetic Processes, and Composition of Unconventional Resource Shale Reservoirs as Determined by Conventional Scanning Electron Microscopy, 37–44. doi:10.1306/13391703M102441

Sorby, H.C., 1860, On the origin of “cone-in-cone”. British Association for the Advancement of Science, Report of the 29th Meeting, 1859, Transactions of Sections, Geology, p 124.

Spaw, J. M., 2012, Identification, Integration and Upscaling of Mudrock Types - A Pathway to Unlocking Shale Plays

Spears, D. A., 1976, The fissility of some Carboniferous shales Sedimentology, v. 23, p. 323-7.

Spears, D. A., 1980, Towards a classification of shales, v. 137, p. 125–129.

Surles, M. A., 1987, Stratigraphy of the Eagle Ford Group (Upper Cretaceous) and its source-rock potential in the East Texas Basin: Baylor Geological Studies Bulletin No. 45, p. 57.

Taylor, K. G., & Macquaker, J. H. S. (2000). Early diagenetic pyrite morphology in a mudstone-dominated succession: the Lower Jurassic Cleveland Ironstone Formation, eastern England. Sedimentary Geology, v. 131(1-2), p. 77–86. doi:10.1016/S0037-0738(00)00002-6

Teerman, S. C., B. J. Cardott, R. W. Harding, M. J. Lemos De Sousa, D. R. Logan, H. J. Pinheiro, M. Reinhardt, C. L. Thompson-Rizer, and R. A. Woods, 1995, Source rock/ dispersed organic matter characterization: TSOP research subcommittee results: Organic Geochemistry, 22, 11– 25. doi:10.1016/0146-6380(95)90004-7.

Tissot, B. P., and D. H. Welte, 1984, Petroleum formation and occurrence, 2nd ed.: Springer-Verlag, Berlin, Germany, p. 699.

Tourtelot, H. A., 1960, Origin and use of the word shale. Am. J. Sci. Bradley, v 258-A, p. 335-43.

Tovey, N. K., and Krinsley, D. H., 1991, Mineralogical mapping of scanning electron micrographs. Sedimentary Geology, v. 75(1-2), p. 109–123. doi:10.1016/0037-0738(91)90053-G

Ulicny, David Hladikova, Jana and Hredecka, L., 1993, Record of sea-level changes, oxygen depletion and the Carbon Anomaly Across the Cenomanian-Turonian Boundary, Bohemian Cretaceous Basin.

Vandenbroucke, M., and Largeau, C., 2007, Kerogen origin, evolution and structure. Organic Geochemistry, 38(5), 719–833. doi:10.1016/j.orggeochem.2007.01.001

Velde, B., 1996, Compaction trends of clay-rich deep-sea sediments: Marine Geology, v. 133, p. 193–201.

Welton, J. E., 1984, *SEM Petrology Atlas*.

White, R. J., Spinelli, G. a., Mozley, P. S., and Dunbar, N. W., 2011, Importance of volcanic glass alteration to sediment stabilization: offshore Japan. Sedimentology, 58(5), 1138–1154. doi:10.1111/j.1365-3091.2010.01198.x

Wilkin, R. T., and H. L. Barnes, 1997, Formation processes of framboidal pyrite: Geochimica et Cosmochimica Acta, v. 61, p. 323-339.

Wilson, M. J., 1971, Clay Mineralogy of the Old Red Sandstone (Devonian) of Scotland. SEPM Journal of Sedimentary Research, Vol. 41(4). doi:10.1306/74D723D8-2B21-11D7-8648000102C1865D

Wilson, M. D., and Pittman, E. D., 1977, Tertiary Mesozoic Paleozoic Total scribed sequences of diagenetic alterations which affect sandstones of various compositions under differing geochemical conditions. Clay neoformation (precipitation from solution as opposed to regeneration of preexist), 47(1), 3–31.

Workman, S. J., 2013, Integrating Depositional Facies and Sequence Stratigraphy in Characterizing Unconventional Reservoirs : Eagle Ford Shale South Texas: [Master’s Thesis] Western Michigan University

Workman, S. J., and Grammer, G. M., 2013, Integrating Depositional Facies and Sequence Stratigraphy in Characterizing Unconventional Reservoirs in the Cretaceous, p. 473–508.

Wust, R. A., Nassichuk, B. R., and Bustin, M. R., 2013, Porosity Characterization of Various Organic-rich Shales from the Western Canadian Sedimentary Basin, Alberta and British Columbia, Canada, 81–100. doi:10.1306/13391707M1023585

Xun S., Zhang T., and Milliken K.L., 2014, Geochemical Characterization of Organic Matter from the Eagle Ford Formation and Indications of Thermal Maturity and Depositional Redox Conditions (abs.): in American Association of Petroleum Geologists Annual Convention and Exhibition, Houston, Texas.

Zhang, T., Xun S., Milliken K.L., and Ruppel S., 2014, Pore Characterization of Eagle Ford Shales by N2 Adsorption and Desorption Isotherms and Pore Evolution in Organic Matter During Thermal Maturation (abs.): in American Association of Petroleum Geologists Annual Convention and Exhibition, Houston, Texas.

Zuffa, G. G., 1980, Hybrid Arenites: Their Composition and Classification. SEPM Journal of Sedimentary Research, Vol. 50(1). doi:10.1306/212F7950-2B24-11D7-8648000102C1865D